3

POLARIZATION PROPERTIES IN RANDOM SURFACE SCATTERING

A. K. Fung, A. J. Blanchard, and M. F. Chen

3.1 **Introduction**
3.2 **A Surface Scattering Model**
- a. Formulation of the Surface Scattering Problem
- b. Far Zone Backscattered Field
- c. Average Scattered Power
- d. Scattering Coefficients and Special Cases
- e. Theoretical Results and Comparisons with Simulation

3.3 **Dependence of the Backscattering Coefficients on Polarization States**
- a. Surface Scattering Matrix and the Average Received Power
- b. Theoretical Calculations

3.4 **Polarimetric Measurement System and Procedure**
- a. Scattering Coefficient Measurement System and Approach
- b. Imaging Measurement System and Approach

3.5 **Scattering from Statistically Known Surfaces**
- a. An Iterative Solution of the Surface Current Density
- b. Generation of Rough Surfaces in Three-dimensions with Specified Correlation Function
- c. Simulation of Wave Scattering from Rough Surfaces in Three Dimensions

3.6 **Polarization Properties in Surface Imaging**
- a. Holographic Imaging Techniques
- b. Resolution in ISAR Imaging
- c. Projection Images
- d. Polarimetric Imaging of Surfaces

Acknowledgment
References

3.1 Introduction

In this chapter, polarization properties of the surface scattering coefficient are shown as a function of roughness, incidence angle and frequency. Results are presented in the form of scattering coefficient curves and images. In the latter case, scattering from an arbitrary surface patch is needed. This has to be done either experimentally or by numerical simulation since we are dealing with a random surface patch. Images in different polarization states can be computed either from experimental data acquired by using the inverse synthetic aperture method or from the theoretical scattering model discussed in section 3.2. In addition, the variations of the backscattering coefficient with polarization states are also shown.

In section 3.2, the formulation and the assumptions used in deriving a surface scattering model valid over the entire frequency range are presented. The backscattering coefficients for vertical, horizontal, and cross polarizations are given and their dependence on angle, surface roughness parameters and frequency are illustrated. The dependence of these backscattering coefficients on polarization states is discussed in section 3.3. In section 3.4, a scattering measurement procedure is described. Section 3.5 deals with a method for the generation of statistically known surfaces and scattering computations via the method of moments to obtain numerically exact scattering characteristics. Comparisons are made between the simulated backscattering coefficients from known surfaces and the theoretical calculations based on the model in section 3.2. In section 3.6, a formulation for wide band imaging of rough surfaces is given and polarization properties of a rough surface in image form based on laboratory measurements are presented.

3.2 A Surface Scattering Model

The problem of wave scattering from a randomly rough surface has been studied using low and high frequency approximations. Useful results were obtained in the 1960's (Kovalev and Pozknyak 1961; Hagfors 1966; Kodis 1966; Fung 1967, 1968; Valenzuela 1967; Barrick 1968) and were applied to interpret measurements from land and sea surfaces. At that time, it was recognized that radar backscattering at small angles of incidence seemed to follow the high frequency solution derived from the Kirchhoff formulation (Beckmann and Spizzichino

1963; Sancer 1969). At large angles of incidence the first-order solution of the small pertubation method, a low frequency solution, appeared to explain the measurements better especially in the polarization characteristics (Valenzuela 1967; Fung 1967). Towards the end of the 1960's and throughout the 1970's, attempts were made to unite the two approximate solutions with the hope that better agreement with measurements would result. This led to the development of the two-scale models (Semyonov 1966; Wright 1968; Valenzuela 1968; Leader 1978; Brown 1978) which did result in better agreement with measurements (Fuks 1966; Bass and Fuks 1979; Fung and Chan 1971; Wu and Fung 1972). However, several questions remain to be answered:

(1) What is the scattering behavior of the random surface at the intermediate frequencies where neither high nor low frequency approximation is applicable?

(2) Real rough surfaces may have a continuous spectrum of roughness scales. If the two-scale model is applied to interpret measurements from such a surface, will the interpretation be satisfactory from a practical stand point?

(3) Can we find a working model for rough surfaces that do not satisfy either the high or the low frequency approximation?

These questions have been recognized by many investigators and many attempts have been made to obtain models with wider ranges of validity than the two-scale model (DeSanto 1974; Gray *et al* 1978; Garcia *et al* 1979; Fung and Pan 1985; Brown 1985; Bahar 1985; Winebrenner and Ishimaru, 1985). In this section the formulation and results of the scattering model by Fung and Pan (1987) are summarized.

a. Formulation of the Surface Scattering Problem

The key to solving the surface scattering problem lies in the determination of the surface current. One approach to obtain an estimate of the surface current is to solve the integral equation for the surface current by the standard iterative technique. In this case the accuracy of the solution is strongly dependent on the initial guess. For simplicity only a perfectly conducting surface is considered below.

One approach to find a current estimate is to use the integral equation for the surface current $\overline{J}(\overline{r})$.

$$\overline{J}(\overline{r}) = 2\hat{n} \times \overline{H}^i + (1/2\pi) \int_s \hat{n} \times [\nabla G \times \overline{J}(\overline{r})]\, ds' \qquad (2.1)$$

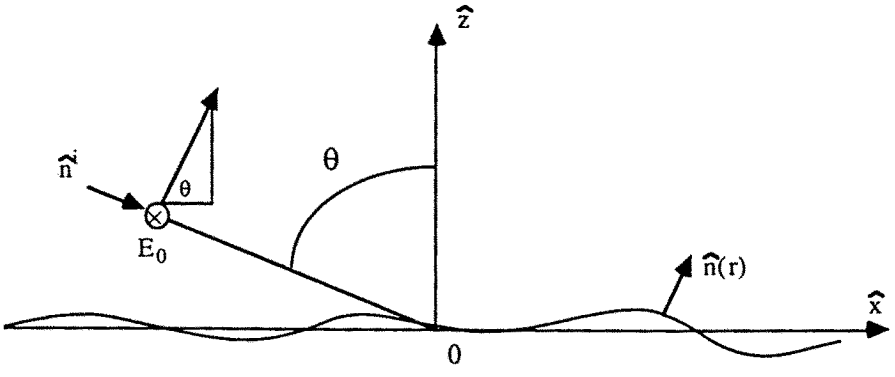

Figure 3.2.1 The geometry of the scattering problem.

where $\hat{n}$ is the unit normal vector to the surface, $\overline{H}^i$ is the incident magnetic field and G is the Green's function. The integration is over the illuminated area of the surface. An estimate of the surface current can be obtained by assuming that we can approximate the surface current under the integral sign by $2\hat{n} \times \overline{H}^i$. To obtain an expression for the surface current consider an incident horizontally polarized field of the form (Fig. 3.2.1).

$$\overline{E}^i = \hat{y}E_0 \exp(-jkx \sin\theta + jkz \cos\theta) = \hat{y}E_0 \exp(-jk_x x - jk_z z) \tag{2.2}$$

where θ is the angle of incidence; k is the wave number in free space and E_0 is the field amplitude. Next, let

$$\overline{n} = \hat{n}/\cos\chi = -\hat{x}Z_x - \hat{y}Z_y + \hat{z}$$

$$\cos\chi = \left[1 + Z_x^2 + Z_y^2\right]^{-1/2}$$

where Zx, Zy are the partial derivatives of the surface $Z(x, y)$. Then, (2.1) can be written as

$$\begin{aligned}(\overline{J}/\cos\chi) &= 2\overline{n} \times \overline{H}^i + (1/2\pi)\int_s \overline{n} \times \left[\nabla G \times (\overline{J}'/\cos\chi)\right] dx'\,dy' \\ &= \overline{J}_{kh} + \overline{J}_{ch}\end{aligned} \tag{2.3}$$

The first term on the right hand side of (2.3) is effectively the Kirchhoff approximation to the surface current density and is used as our first guess to obtain an iterative solution. Upon replacing the Green's function in the second term by its Fourier integral representation, we can write the second term in (2.3) as

$$\overline{J}_{ch} = -\frac{2E_0}{2\pi^2\eta}\int dx'\,dy'\,e^{-jk_x x'-jk_z z'} \cdot \int du dv\, e^{ju(x-x')+jv(y-y')-jq|z-z'|} \begin{bmatrix} \frac{u}{q}Z_y Z_x \sin\theta + \frac{u}{q}(Z_y - Z_{y'})\cos\theta + \frac{v}{q}Z_y Z_{y'}\sin\theta \pm Z_{y'}\sin\theta \\ \frac{Z_x \sin\theta}{q}(uZ_{x'} + vZ_{y'}) - \frac{\cos\theta}{q}(uZ_x + vZ_{y'}) \pm (Z_{x'}\sin\theta + \cos\theta) \\ -Z_y\frac{\cos\theta}{q}(uZ_x + vZ_y) \pm (Z_x Z_{y'}\sin\theta - Z_y Z_{x'}\sin\theta - Z_y\cos\theta) \end{bmatrix} \tag{2.4}$$

where the upper sign of terms with two signs is used when $z > z'$ and the lower sign is used when $z < z'$; $q = [k^2 - u^2 - v^2]^{1/2}$ and η is the intrinsic impedance of free space. For a random surface, we neglect the terms with plus and minus signs because the same term contributes positively over the portion of the surface where $z > z'$ and negatively over the other portion of the surface where $z < z'$. Hence, on the average its positive contribution will cancel its negative contribution. We also ignore higher-order slope terms since they should contribute much less than the first-order terms. In addition, we shall ignore the absolute factor in the phase because, when z and z' are close together in space, z and z' are nearly equal in value and hence will cancel. When the difference between z and z' is large, they are at least one correlation distance apart in space so that the contribution of the total integrand to the final average power is small. The error caused by ignoring this factor is examined in Pan and Fung [1987] leading to a restriction on the validity of the model developed. This condition of validity is

$$\cos^2\theta\left[(k\sigma)^2/(kc)^{1/2}\right]\exp\left[2kc(1-\sin\theta)\right]^{1/2} \ll 1$$

where σ is the surface height standard deviation, c is equal to 0.459 L and L is the surface correlation length. With this understanding, the

expression for the current density in horizontal polarization is

$$\begin{aligned}\overline{J}_h = \overline{J}_{kh} + \overline{J}_{ch} \approx \frac{2E_0}{\eta}\begin{bmatrix} -Z_y \sin\theta \\ Z_x \sin\theta + \cos\theta \\ Z_y \cos\theta \end{bmatrix} \exp(-jk_x x - jk_z z) \\ - \frac{E_0}{2\pi^2\eta}\int dx'dy' \exp(-jk_x x' - jk_z z') \\ \cdot \int du\, dv\, e^{ju(x-x')+jv(y-y')} \begin{bmatrix} \frac{u}{q}(Z_y - Z_{y'})\cos\theta \\ -\frac{\cos\theta}{q}(uZ_x + vZ_{y'}) \\ 0 \end{bmatrix}\end{aligned} \tag{2.5}$$

For a vertically polarized incident wave of the form,

$$\overline{E}^i = E_0(\hat{x}\cos\theta + \hat{z}\sin\theta)\exp(-jk_x x - jk_z z)$$

calculations similar to the horizontally polarized case yield the following expression for the surface current density

$$\begin{aligned}\overline{J}_v = \overline{J}_{kv} + \overline{J}_{cv} \approx (2E_0/\eta)\begin{bmatrix} 1 \\ 0 \\ Z_x \end{bmatrix} \exp(-jk_x x - jk_z z) \\ - \frac{E_0}{2\pi^2\eta}\int dx'\, dy' \exp(-jk_x x' - jk_z z') \\ \int du\, dv\, e^{ju(x-x')+jv(y-y')} \begin{bmatrix} -\frac{u}{q}Z_{x'} - \frac{v}{q}Z_y \\ \frac{v}{q}(Z_x + Z_{x'}) \\ 0 \end{bmatrix}\end{aligned} \tag{2.6}$$

All the notations have been used previously.

b. Far Zone Backscattered Field

In accordance with the Stratton-Chu integral, we can write the far zone scattered field from a perfectly conducting surface as

$$\overline{E}(\overline{r}) = -C\eta\hat{r} \times \int_{A_0} \hat{r} \times \overline{J}_p \exp(jk\hat{r}\cdot\overline{r})dx\, dy \tag{2.7}$$

where $C = (-jk/4\pi R)\exp(-jkR)$, $\hat{r}$ is the unit vector pointing in the direction of observation, A_o is the illuminated area, η is the intrinsic impedance of free space, $\overline{J}_p$ is equal to either $\overline{J}_v$ or $\overline{J}_h$, and k is the wave number. In backscattering,

$$k\hat{r} = -\hat{x}k\sin\theta + \hat{z}k\cos\theta = -\overline{k}$$

Thus, (2.7) becomes

$$\overline{E}(\overline{r}) = -C\eta\hat{r} \times \int_{A_0} \left[\hat{r}(\hat{r}\cdot\overline{J}_p) - \overline{J}_p\right] \exp(\overline{jk}\cdot\overline{r})dx\,dy \tag{2.8}$$

For horizontal polarization,

$$\begin{aligned} E_{hh} = \hat{y}\cdot\overline{E}(\overline{r}) &= 2CE_0 \int dx\,dy\,(Z_x\sin\theta + \cos\theta)\,e^{-2jk_x x - jk_z z} \\ &+ (\cos\theta\, CE_0/2\pi^2)\int dx\,dy\,dx'\,dy'\,e^{[-jk_x(x+x')-jk_z(z+z')]} \\ &\cdot \int du\,dv\left[(uZ_x + vZ_{y'})/q\right] e^{ju(x-x')+jv(y-y')} \end{aligned} \tag{2.9}$$

Upon applying integration by parts to (2.9) and ignoring edge effects we obtain

$$\begin{aligned} E_{hh} &= 2CE_0\sec\theta \int dx\,dy\,e^{-2jk_x x - 2jk_z z} \\ &+ (CE_0/2\pi^2 k)\int dx\,dy\,e^{(-jk_x x - jk_z z)}\int dx'\,dy' e^{(-jk_x x' - jk_z z')} \\ &\cdot \int du\,dv\,[(k_x u - u^2 + v^2)/q] e^{ju(x-x')+jv(y-y')} \end{aligned} \tag{2.10}$$

Similarly, we can show that for the vertically polarized case the backscattered field is

$$\begin{aligned} E_{vv} &= 2CE_0\sec\theta \int dx\,dy\,e^{-2jk_x x - 2jk_z z} \\ &+ (CE_0/2\pi^2 k)\int dx\,dy\,e^{(-jk_x x - jk_z z)}\int dx'\,dy'\,e^{(-jk_x x' - jk_z z')} \\ &\cdot \int du\,dv\,\left[(k_x u + u^2 - v^2)/q\right] e^{ju(x-x')+jv(y-y')} \end{aligned} \tag{2.11}$$

The cross polarized scattered field can also be computed by taking $\hat{y} \cdot \overline{E}(\bar{r})$ where $\overline{J}_v$ is used in the field expression to obtain

$$E_{hv} = \left(CE_0/\pi^2 k \cos\theta\right) \int dx\, dy\, dx'\, dy'\, du\, dv\, (uv/q) \cdot \exp\left[-jk_x(x+x') - jk_z(z+z') + ju(x-x') + jv(y-y')\right] \tag{2.12}$$

In backscattering $E_{vh} = E_{hv}$ due to reciprocity and hence does not have to be computed separately. Now that all the field expressions are available, we are ready to compute the average scattered power.

c. *Average Scattered Power*

Upon comparing (2.10) and (2.11), we see that the first terms in these equations are the same indicating that, for a perfectly conducting surface, there is no polarization difference between vertically and horizontally polarized cases under the Kirchhoff approximation. It is convenient to separate the field expression into two components, namely, the Kirchhoff field and the non-Kirchhoff field. For vertical polarization, we denote these field components as

$$E_{vv} = E_K + E_C^v \tag{2.13}$$

To find the average power, we multiply E_{vv} by its conjugate E_{vv}^* and then take the ensemble average

$$\langle E_{vv} E_{vv}^* \rangle = \langle E_K E_K^* \rangle + 2\mathrm{Re}\left[\langle E_K^* E_C^v \rangle\right] + \langle E_C^v E_C^{v^*} \rangle \tag{2.14}$$

The first term in (2.14) is the standard Kirchhoff term and can be computed as has been done in the past (Beckmann and Spizzichino 1963; Sancer 1969). Our major interest here is in the incoherently scattered power which is what is usually measured. This means we should subtract the mean or the coherent field from the expression given by (2.13) before we form the power expression. However, this is equivalent to computing the terms in (2.14) and then subtracting an appropriate mean product or mean squared quantity from each term. In what follows, we shall proceed by considering each term in (2.14). For the purpose of illustration, we shall assume Gaussian height distribution for the surface under consideration.

The first term in (2.14) is

$$\langle E_k E_k^* \rangle = 4|C|^2 E_0^2 \sec^2\theta \int dx\, dy\, dx' dy'\, e^{2jk_x(x-x')} \langle e^{2jk_z(z-z')} \rangle$$
$$= 4|C|^2 E_0^2 \sec^2\theta \int dx\, dy \int e^{2jk_x\xi} e^{-k_z^2\sigma^2[1-\rho(\xi,\eta)]} d\xi d\eta \quad (2.15)$$

where $\xi = x' - x$, $\eta = y' - y$, and $\rho(\xi,\eta)$ is the surface height autocorrelation function and σ^2 is the variance of the surface. To obtain the incoherent power, we subtract the mean magnitude squared value, $|\langle E_K \rangle|^2$, from it yielding

$$\langle E_K E_K^* \rangle - |\langle E_K \rangle|^2 = 4A_0|C|^2 E_0^2 \sec^2\theta$$
$$\cdot \int d\xi d\eta\, e^{2jk_x\xi}\, e^{-4k_z^2\sigma^2} \left[e^{4k_z^2\sigma^2\rho} - 1 \right] \quad (2.16)$$

where A_0 is the illuminated area.

The second term in (14) requires the evaluation of the product

$$\langle E_K^* E_C^v \rangle = \left(|C|^2 E_0^2/\pi^2 k \cos\theta\right)$$
$$\cdot \int dx\, dy\, dx'\, dy'\, dx''\, dy'' \langle e^{jk_z(2z''-z'-z)} \rangle$$
$$\cdot \int du\, dv\, \frac{(k_x+u)u - v^2}{q}$$
$$\cdot e^{jk_x(2x''-x'-x)-ju(x'-x)-jv(y'-y)} \quad (2.17)$$

where

$$\langle e^{jk_z(2z''-z'-z)} \rangle = \exp\Big\{ -k_z^2\sigma^2 [3 - 2\rho(x''-x', y''-y')$$
$$+ 2\rho(x''-x, y'') + \rho(x'-x, y'-y)] \Big\}$$
$$= \exp\left\{ -k_z^2\sigma^2 \left[3 - 2\rho_{12} - 2\rho_{13} + \rho_{23}\right] \right\} \quad (2.18)$$

After a change of variables, $\xi = x'' - x'$, $\eta = y'' - y'$, $\zeta = x'' - x$, $\tau = y'' - y$

$$\langle E_K^* E_C^v \rangle = \left(|C|^2 E_0^2/\pi^2 k \cos\theta\right) e^{-3k_z^2\sigma^2} \int dx\, dy \int du\, dv\, \frac{k_x u + u^2 - v^2}{q}$$
$$\cdot \int d\xi\, d\eta \int d\zeta\, d\tau\, e^{-k_z^2\sigma^2\rho_{23}(\zeta-\xi,\tau-\eta)} e^{j(u+k_x)\xi + jv\eta + 2k_z^2\sigma^2\rho_{12}(\xi,\eta)}$$
$$\cdot e^{-j(u-k_x)\zeta - jv\tau + 2k_z^2\sigma^2\rho_{13}(\zeta,\tau)} \quad (2.19)$$

In (2.19), x and y can be integrated to give the illuminated area A_0. To obtain the incoherent power we remove the mean from the above product yielding

$$\langle E_K^* E_C^v\rangle - \langle E_K^*\rangle\langle E_c^v\rangle = \left(\frac{|C|^2 E_0^2 A_0}{\pi^2 k\cos\theta}\right) e^{-3k_z^2\sigma^2} \cdot \int \frac{k_x u + u^2 - v^2}{q}\, du\, dv \int d\zeta\, d\tau \int d\xi\, d\eta\, e^{-k_z^2\sigma^2\rho_{23}(\zeta-\xi,\tau-\eta)} \cdot e^{j(u+k_x)\xi + jv\eta - j(u-k_x)\zeta - jv\tau}\left\{e^{2k_z^2\sigma^2[\rho_{13}(\xi,\eta)+\rho_{12}(\zeta,\tau)]} - 1\right\} \quad (2.20)$$

To obtain some insight into this term, we rewrite the ρ_{23} factor and the terms in the last bracket as

$$\sum_0^\infty \frac{[-k_z^2\sigma^2\rho_{23}(\zeta-\xi,\tau-\eta)]^n}{n!}\left\{\sum_0^\infty \frac{[2k_z^2\sigma^2\rho_{13}(\xi,\eta)]^n}{n!} \sum_0^\infty \frac{[2k_z^2\sigma^2\rho_{12}(\zeta,\tau)]^m}{m!} - 1\right\}$$

The explicit forms of the first few terms of the above expression are

$$2k_z^2\sigma^2\{\rho_{13}(\xi,\eta) + \rho_{12}(\zeta,\tau) + 2k_z^2\sigma^2[\rho_{13}(\xi,\eta)\rho_{12}(\zeta,\tau) + \rho_{13}^2(\xi,\eta)/2 + \rho_{12}^2(\zeta,\tau)/2] - k_z^2\sigma^2\rho_{23}(\zeta-\xi,\tau-\eta)[\rho_{13}(\xi,\eta) + \rho_{12}(\zeta,\tau)] + \ldots\}$$

Upon examining the above terms involving $\rho_{12}(\zeta,\tau)$ alone, we note that they vanish because integrations with respect to ξ and η generate Dirac delta functions, $\delta(u+k_x)$ and $\delta(v)$, which force the factor, $(k_x u + u^2 - v^2)$, in the integrand to zero. In view of the sign difference between the non-Kirchhoff terms in E_{VV} and E_{HH}, it is clear that if we were to calculate $\langle E_K^* E_c^h\rangle$ in horizontal polarization all terms involving $\rho_{13}(\xi,\eta)$ alone would vanish instead. This implies that the terms involving the cross product such as $\rho_{13}(\xi,\eta)\rho_{12}(\zeta,\tau)$ must be of higher order and hence can be neglected in polarized scattering calculation. Knowing this property we can approximate (2.20) by dropping all the product terms in surface correlation yielding

$$\langle E_K^* E_C^v\rangle - \langle E_K^*\rangle\langle E_C^v\rangle = (8|C|^2 E_0^2 A_0)\tan^2\theta\, e^{-3k_z^2\sigma^2} \cdot \int d\xi\eta\, e^{j2k\xi\sin\theta} \sum_{n=1}^\infty \frac{[2k_z^2\sigma^2\rho_{13}(\xi,\eta)]^n}{n!} \quad (2.21)$$

It is interesting to note that the polarization difference only appears as a sign difference in this term and hence it is unnecessary to repeat the calculation for horizontal polarization.

The third term in (2.14) can be written as

$$\langle E_C^v E_C^{v*}\rangle = \frac{|C|^2 E_0^2}{4\pi^4 k^2}\int dx\,dy\,dx'\,dy'\,d\overline{x}\,d\overline{y}\,d\overline{x}'\,d\overline{y}'\,du\,dv\,d\overline{u}\,d\overline{v}$$
$$\cdot\left\{[u(k_x+u)-v^2][\overline{u}(k_x+\overline{u})-\overline{v}^2]/q\overline{q}\right\}\langle e^{jk_x(\overline{x}-x'-x+\overline{x}')}\rangle$$
$$\cdot e^{jk_z(\overline{x}-x)+j(\overline{vy'}-vy')+j(k_x+\overline{u})\overline{x}'-j(k_x+u)x'+j(ux-\overline{u}\overline{x})+j(vy-\overline{v}\overline{y})} \tag{2.22}$$

where

$$\langle e^{jk_x(\overline{x}-x-x'+\overline{x}')}\rangle = e^{-k_x^2\sigma^2(2+\rho_{23}+\rho_{14}-\rho_{12}-\rho_{13}-\rho_{24}-\rho_{34})} \tag{2.23}$$

The subscripts of the correlation functions refer to the four types of points, namely, $\overline{x}$, x', x, and $\overline{x}'$ numbered as 1, 2, 3 and 4 respectively. After a change of variables to the difference coordinates with $x-\overline{x}=\xi$, $y-\overline{y}=\nu$, $x'-\overline{x}'=\zeta$, $y'-\overline{y}'=\tau$, $\overline{x}-\overline{x}'=\overline{\tau}$, $\overline{y}-\overline{y}'=\overline{\kappa}$, we obtain

$$\langle E_C^v E_C^{v^*}\rangle = \frac{|C|^2 E_0^2}{4\pi^4 k^2}\int d\overline{x}'\,d\overline{y}'\int du\,dv\int d\overline{u}\,d\overline{v}$$
$$\cdot\frac{(k_x u+u^2-v^2)(k_x\overline{u}+\overline{u}^2-\overline{v}^2)}{q\overline{q}}$$
$$e^{-2k_z^2\delta^2}\int d\xi\,d\zeta\int d\tau\,d\eta\int d\overline{\tau}\,d\overline{\kappa}$$
$$e^{k_z^2\sigma^2(\rho_{13}+\rho_{24}+\rho_{12}+\rho_{34}-\rho_{14}-\rho_{23})}$$
$$e^{-jk_x(\xi+\zeta)-ju(\zeta-\xi)-jv\tau+jv\eta-j(\overline{u}-u)\overline{\tau}-j(\overline{v}-v)\overline{\kappa}} \tag{2.24}$$

Then, integrating $\overline{x}'$ and $\overline{y}'$ to obtain the illuminated area and subtracting the mean magnitude squared value, we get

$$\langle E_C^v E_C^{v^*}\rangle - |\langle E_C^v\rangle|^2 = \frac{|C|^2 E_0^2 A_0}{4\pi^4 k^2}e^{-2k_z^2\sigma^2}\int du\,dv\int d\overline{u}\,d\overline{v}$$
$$\cdot\frac{(k_x u+u^2-v^2)(k_x\overline{u}+\overline{u}^2-\overline{v}^2)}{q\overline{q}}\int d\overline{\tau}\,d\overline{\kappa}\int d\xi\,d\eta\int d\tau\,d\zeta$$
$$\cdot e^{-j(k_x+u)\zeta-jv\tau-j(k_x-u)\xi+jv\eta-j(\overline{u}-u)\overline{\tau}-j(\overline{v}-v)\overline{\kappa}}$$
$$\cdot e^{-k_z^2\sigma^2[\rho_{23}(\xi-\zeta+\overline{\tau},\eta-\tau+\overline{\kappa})+\rho_{14}(\overline{\tau},\overline{\kappa})]}$$
$$\cdot\left\{e^{k_z^2\sigma^2[\rho_{13}(\xi,\eta)+\rho_{24}(\zeta,\tau)-\rho_{12}(\zeta-\overline{\tau},\tau-\overline{\kappa})-\rho_{34}(\xi+\overline{\tau},\eta+\overline{\kappa})]}-1\right\} \tag{2.25}$$

The property of the factor in the last bracket in (2.25) is similar to the one in (2.20). Here, it is also possible to obtain a very good approximation by ignoring the cross product terms in the surface correlation function. In addition, the integration of ρ_{12} and ρ_{34} terms goes to zero in the backscatter direction. Thus, by retaining only the dominant terms in (2.25) we have

$$\langle E_C^v E_C^{v*}\rangle - |\langle E_c^v\rangle|^2 = 16A_0|C|^2E_0^2e^{-2k_z^2\sigma^2}\sin^4\theta/\cos^2\theta \int d\zeta d\tau e^{-j2k\zeta\sin\theta}\sum_{n=1}^{\infty}\left[k_z^2\sigma^2\rho_{24}(\zeta,\tau)\right]^n/n! \tag{2.26}$$

It is interesting to note that because the factor involving the u and v variables in (2.25) is being squared there is no difference in the final result of (2.26) and its corresponding expression for horizontal polarization.

d. Scattering Coefficients and Special Cases

The discussions in the previous section indicate that of the three terms in (2.14) only the second term shows a sign difference between polarizations. The other two terms remain the same. Hence, the backscattering coefficients can be obtained for both polarizations by multiplying the power expressions given by (2.16), (2.21), and (2.26) by the factor, $(4\pi R^2/A_oE_o^2)$, and summing together the three expressions in accordance with (2.14). Denoting the backscattering coefficients by σ_{vv}^0 and σ_{hh}^0 for vertical and horizontal polarizations respectively, we have

$$\sigma_{\substack{vv\\hh}}^0 = \frac{2k^2}{\cos^2\theta}\left\{e^{-4k^2\sigma^2\cos^2\theta}\sum_{n=1}^{\infty}\frac{(4k^2\sigma^2\cos^2\theta)^n}{n!}W^{(n)}(2k\sin\theta,0) \pm 4\sin^2\theta e^{-3k^2\sigma^2\cos^2\theta}\sum_{n=1}^{\infty}\frac{(2k^2\sigma^2\cos^2\theta)^n}{n!}W^{(n)}(2k\sin\theta,0) + 4\sin^4\theta e^{-2k^2\sigma^2\cos^2\theta}\sum_{n=1}^{\infty}\frac{(k^2\sigma^2\cos^2\theta)^n}{n!}W^{(n)}(2k\sin\theta,0)\right\} \tag{2.27}$$

where $W^{(n)}(U,V)$ is the roughness spectrum of the surface related to the n^{th} power of the surface correlation function by the Fourier transform as follows:

$$W^{(n)}(U,V) = 1/2\pi\int_{-\infty}^{\infty}d\xi d\zeta e^{-jU\xi-jV\zeta}\rho^n(\xi,\zeta),\ (n=1,2,\ldots)$$

Note that the first term in (2.27) is the standard Kirchhoff term. It should be the only term left when we take the high frequency limit. This, indeed, is the case since the exponential decay factor in front of the second and the third terms are larger than the corresponding increases in the infinite sums as the wave number increases. More specifically, the sum in the second term cannot increase faster than $\exp(2k^2\sigma^2\cos^2\theta)$ and similarly the sum in the third term cannot increase faster than $\exp(k^2\sigma^2\cos^2\theta)$ as the wave number increases.

To verify the low frequency limit, we need to take only the $n = 1$ term in (2.27) and approximate the exponential functions by unity yielding

$$\sigma^0_{\substack{vv \\ hh}} = 8k^4\sigma^2 W(2k\sin\theta, 0)\cdot\begin{cases}(1+\sin^2\theta)^2 \\ \cos^4\theta\end{cases} \tag{2.28}$$

which is exactly the same as the results derived from the first-order small perturbation theory.

As an example, for a Gaussian correlation function,

$$\rho^n(\xi,\zeta) = \exp[-(\xi^2+\zeta^2)/L^2]$$

(2.27) takes the form,

$$\sigma^0_{vv} = \left(\frac{2kL}{\cos\theta}\right)^2 e^{-4k^2\sigma^2\cos^2\theta}\sum_{m=1}^{\infty}\frac{(k\sigma\cos\theta)^{2m}}{m!m}e^{-(kL\sin\theta)^2/m}$$
$$\left\{4^{m-1} + 2^m\sin^2\theta e^{(k\sigma\cos\theta)^2} + \sin^4\theta e^{2(k\sigma\cos\theta)^2}\right\} \tag{2.29}$$

We can derive the cross polarized backscattering coefficient denoted by σ^0_{hv} in a similar manner as we derived (2.26)

$$\sigma^0_{hv} = \sigma^0_{vh} = \left(\frac{4\pi R^2}{E_0^2 A_0}\right)\langle|E_{hv}|^2\rangle$$
$$= \frac{8}{\pi\cos^2\theta}e^{-2k^2\sigma^2\cos^2\theta}\sum_{m,n=1}^{\infty}\frac{\left(k^2\sigma^2\cos^2\theta\right)^{m+n}}{m!n!}$$
$$\cdot\int du\,dv\frac{u^2v^2W^{(m)}(k\sin\theta+u,v)W^{(n)}(k\sin\theta-u,-v)}{k^2-u^2-v^2} \tag{2.30}$$

It is easy to see that (2.30) vanishes in the high frequecy limit due to the exponential decay factor. In the low frequency region, we set

$m = n = 1$ and approximate $\exp(-2k^2\sigma^2\cos^2\theta)$ by unity yielding

$$\sigma^0_{hv} = \sigma^0_{vh} = \frac{8}{\pi}k^4\sigma^4\cos^2\theta \cdot \int du\,dv\,\frac{[u^2v^2W(k\sin\theta+u,v)W(k\sin\theta-u,-v)]}{k^2-u^2-v^2} \quad (2.31)$$

This expression is in agreement with Rice (1951) and also Valenzuela (1968) if we let the relative dielectric constant approach infinity in Valenzuela (1968). Note that the singularity, $(k^2-u^2-v^2)^{-1}$, in (2.30) and (2.31) is due to the assumption of a perfectly conducting surface. It comes from taking the limit as ε_r tends to infinity on

$$\left|\frac{(\varepsilon_r-1)^2\sqrt{\varepsilon_r-\sin^2\theta}}{(\varepsilon_r\cos\theta+\sqrt{\varepsilon_r-\sin^2\theta})(\cos\theta+\sqrt{\varepsilon_r-\sin^2\theta})}\right|^2 \cdot \left|\varepsilon_r\sqrt{k^2-u^2-v^2}+\sqrt{\varepsilon_rk^2-u^2-v^2}\right|^{-2} \quad (2.32)$$

while keeping $(k^2-u^2-v^2)^{-1/2}$ greater than zero. The dielectric formulation given above [Valenzuela, 1968] does not have a singularity when $(k^2-u^2-v^2)^{-1/2}$ tends to zero.

e. Theoretical Results and Comparisons with Simulation

For ease of reference, we shall refer to (2.27) and (2.30) as the Integral Equation Model (IEM) since it is based on the integral equation for the surface current. In Figs. 3.2.2 through 3.2.3, we show the dependence of the like and cross polarization coefficients on the roughness parameter $k\sigma$ between 0.25 and 0.5 while kL is kept constant at 3.14. We purposely select an intermediate kL value since in the low and high frequency regions, scattering characteristics can be easily determined from the small perturbation and the Kirchhoff models. For the purpose of obtaining some reference, the predictions of the Kirchhoff and the first-order small perturbation models in like polarization and the second-order perturbation in cross polarization are also plotted on the same graphs. At $k\sigma = 0.25$, IEM predictions agree well with the small perturbation results in cross polarization but deviates at larger angles of incidence in like polarizations because the kL value is larger than what is required by the perturbation model. The Kirchhoff predictions are correct only at normal incidence. As $k\sigma$ increases to 0.5,

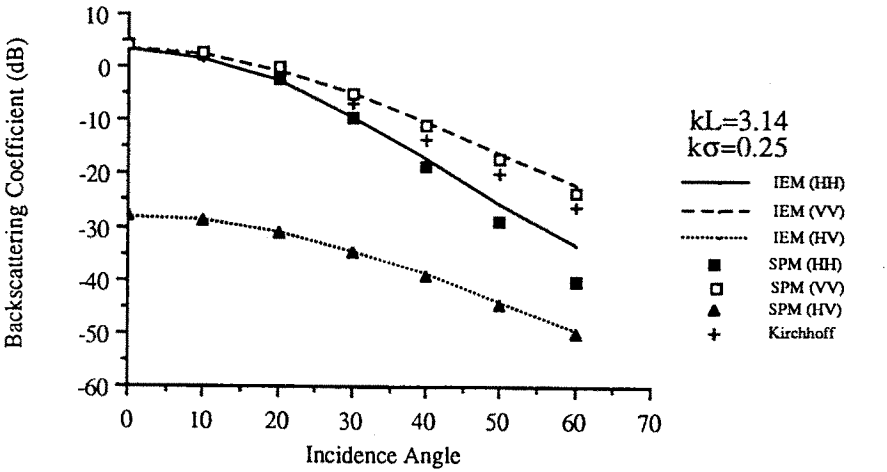

Figure 3.2.2 Comparison of the backscattering coefficient between the integral equation model (IEM), the Kirchhoff approximation and the small perturbation model (SPM) for a Gaussian surface with normalized roughness parameters $k\sigma = 0.25, kL = 3.14$.

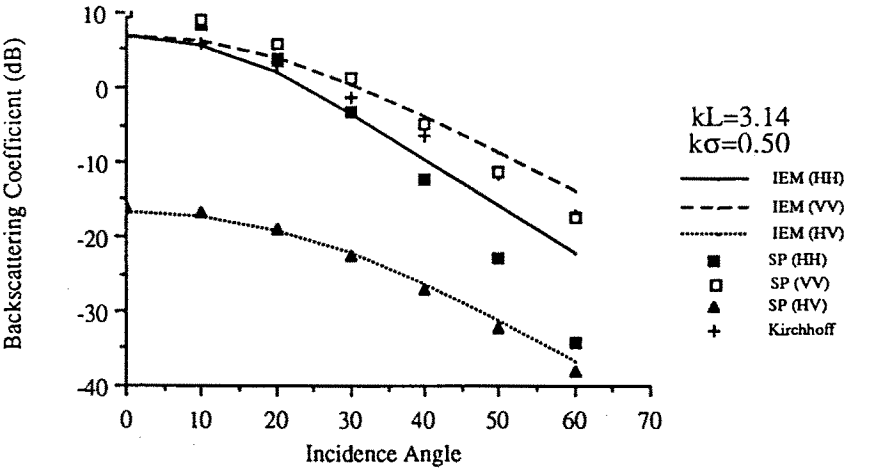

Figure 3.2.3 Comparison of the backscattering coefficient between the integral equation model (IEM), the Kirchhoff approximation and the small perturbation model (SPM) for a Gaussian surface with normalized roughness parameters $k\sigma = 0.50, kL = 3.14$.

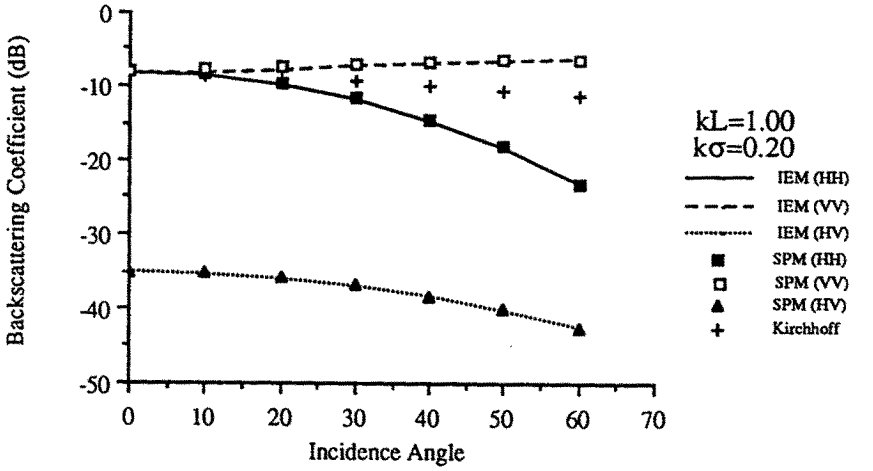

Figure 3.2.4 Comparison of the backscattering coefficient between the integral equation model (IEM), the Kirchhoff approximation and the small perturbation model (SPM) for a Gaussian surface with normalized roughness parameters $k\sigma = 0.20, kL = 1.00$.

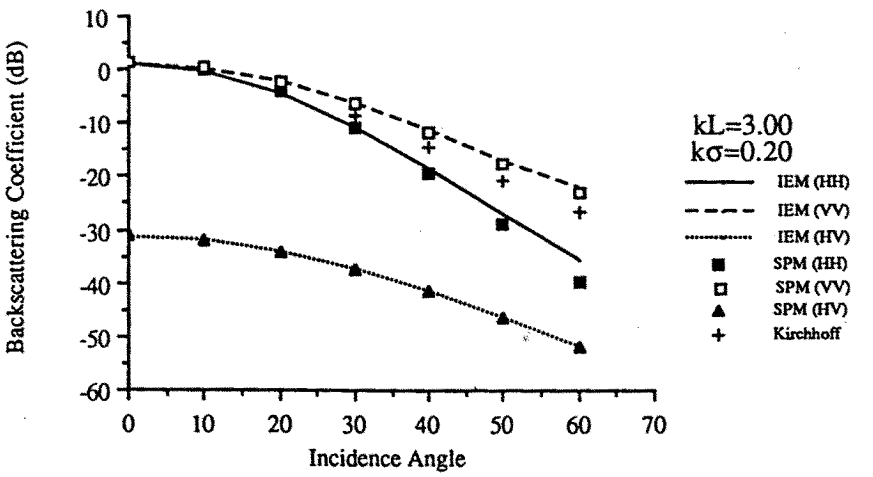

Figure 3.2.5 Comparison of the backscattering coefficient between the integral equation model (IEM), the Kirchhoff approximation and the small perturbation model (SPM) for a Gaussian surface with normalized roughness parameters $k\sigma = 0.20, kL = 3.00$.

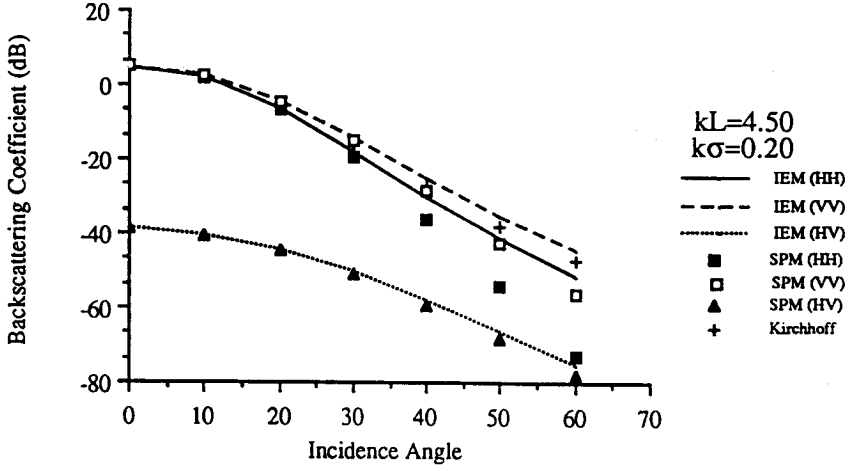

Figure 3.2.6 Comparison of the backscattering coefficient between the integral equation model (IEM), the Kirchhoff approximation and the small perturbation model (SPM) for a Gaussian surface with normalized roughness parameters $k\sigma = 0.20, kL = 4.50$.

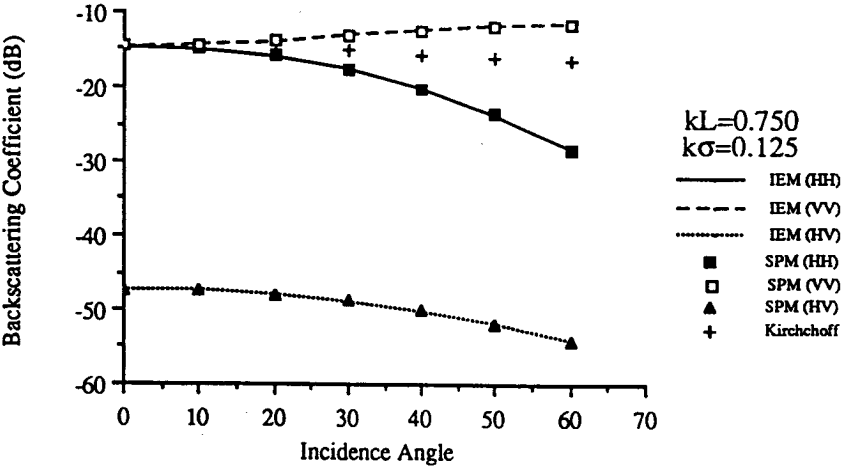

Figure 3.2.7 Comparison of the backscattering coefficient between the integral equation model (IEM), the Kirchhoff approximation and the small perturbation model (SPM) for a Gaussian surface with normalized roughness parameters $k\sigma = 0.125, kL = 0.75$.

IEM predictions differ significantly from the small perturbation results in like polarizations since the latter is no longer valid. The cross polarized returns have also begun to differ but not significantly. This shows that the cross polarized coefficient given by the second-order perturbation method has a wider range of validity in kL and $k\sigma$ values than the first-order like polarized coefficients. The overall angular trends for both like and cross are to drop-off slower as $k\sigma$ increases and the level increase in the cross is much faster than the like.

Figures 3.2.4 through 3.2.6 show the IEM model behavior when the roughness parameter kL is varied from 1 to 4.5 while $k\sigma$ is kept at 0.2. When $k\sigma = 0.2$ and $kL = 1$, IEM agrees well with the small perturbation model in both like and cross polarizations. As kL increases, the separation between VV and HH polarizations decreases, angular trends drop-off faster and IEM approaches the Kirchhoff model in like polarization. Due to the choice of the small $k\sigma$ value the difference between the cross polarized coefficients is not very significant even when kL is 4.5. This again shows that the second-order perturbation model for the cross polarization has a wider range of validity than the first-order like polarized model. This is to be expected theoretically. It is specially interesting to note that the level of the cross polarized returns rises as kL increases from 1 to 3 but then it decreases for further increases in kL to lower levels than when kL was 1. The initial increase in level is due to having a larger scale of roughness, while the decrease is due to having a significantly smaller slope. This decrease is consistent with the fact that a Kirchhoff type surface has a low level of depolarization.

To show frequency dependence, we illustrate in Figs. 3.2.7 to 3.2.9 the like polarized scattering properties by varying $k\sigma$ from 0.125 to 0.75 and kL from 0.75 to 4.5, a change in frequency by a factor of 6. We see a perfect match between the small perturbation model and IEM at the low frequency end, a gradual decrease in the separation between the VV and HH polarizations as frequency increases and the approach to the geometric optics solution at the high frequency end. Note that while the polarized coefficients approach the Kirchhoff solution at the high frequency end just like the case when kL increases, the cross polarized coefficient near vertical incidence appears to saturate at the high frequency end. The difference in the cross polarized behavior between large kL and high frequency cases is due to the fact that the surface does not change in the study of the frequency response while permitting kL to increase means that the surface slope is becom-

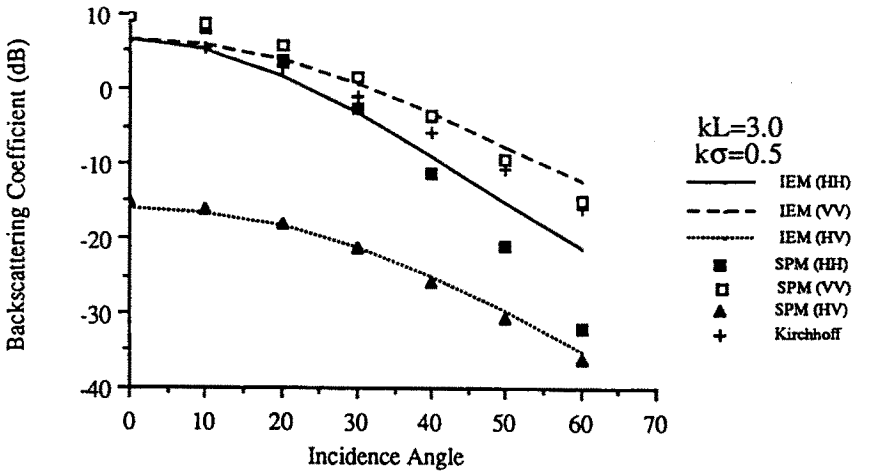

Figure 3.2.8 Comparison of the backscattering coefficient between the integral equation model (IEM), the Kirchhoff approximation and the small perturbation model (SPM) for a Gaussian surface with normalized roughness parameters $k\sigma = 0.5, kL = 3.0$.

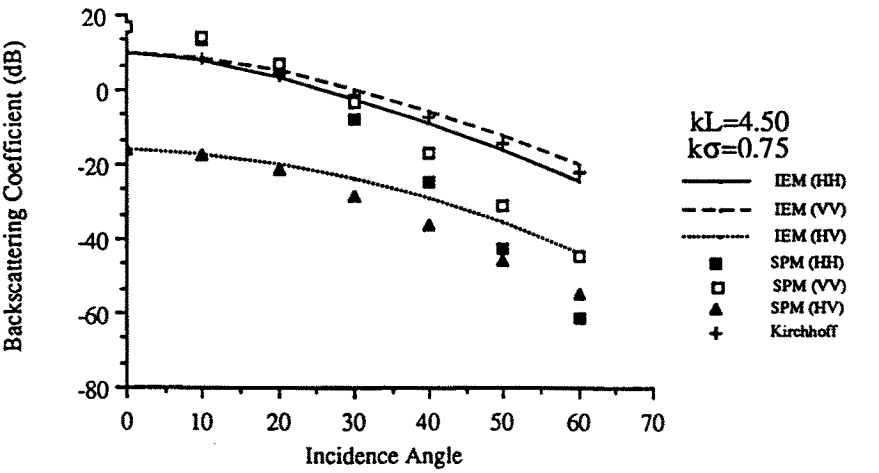

Figure 3.2.9 Comparison of the backscattering coefficient between the integral equation model (IEM), the Kirchhoff approximation and the small perturbation model (SPM) for a Gaussian surface with normalized roughness parameters $k\sigma = 0.75, kL = 4.5$.

ing smaller. The justification of this frequency trend will be shown in section 3.5c where comparisons are made with numerical simulation calculations for both like and cross polarizations.

3.3 Dependence of Backscattering Coefficients on Polarization States

A standard method to denote the polarization state of a plane wave is to use the polarization ellipse defined in terms of the ellipticity angle τ and a pair of orthogonal vector bases, $\hat{x}$ and $\hat{y}$ as

$$\overline{E} = [\hat{x}\cos\tau + j\hat{y}\sin\tau]E_0 e^{j(\omega t - kz)}$$

For simplicity, we shall set the field amplitude E_0 to unity and generalize the polarization state by assuming that the major axis of the ellipse in direction $\hat{x}$ is oriented at an angle ψ from the axis of the reference coordinates $\hat{\phi}$ and $\hat{\theta}$ of the transmitting antenna defined in Fig. 3.3.1. Thus, the polarization state of the transmitting antenna is defined by

$$\overline{a}_t = \Big\{\hat{\phi}(\cos\tau\cos\psi - j\sin\tau\sin\psi) + \hat{\theta}(\cos\tau\sin\psi + j\sin\tau\cos\psi)\Big\}e^{j\omega t}$$

and is characterized by the ellipticity angle τ and the orientation angle ψ. It is clear that the polarization state of the receiving antenna can be characterized in a similar way and we shall denote it by $\overline{a}_r$. In general, a different set of ellipticity and orientation angles may associate with the receiving antenna. To find the average received power, we need to calculate the received voltage through the scattering matrix of the rough surface which is discussed in the next section.

a. Surface Scattering Matrix and the Averaged Received Power

The polarization state of the transmitting antenna written in matrix form using phasor representation is

$$\begin{bmatrix} a_{t\phi} \\ a_{t\theta} \end{bmatrix} = \begin{bmatrix} (\cos\tau\cos\psi - j\sin\tau\sin\psi) \\ (\cos\tau\sin\psi + j\sin\tau\cos\psi) \end{bmatrix} \tag{3.1}$$

Let us denote the surface scattering matrix by S. That is,

$$S = [S_{pq}] = \begin{bmatrix} S_{\phi\phi} & S_{\phi\theta} \\ S_{\theta\phi} & S_{\theta\theta} \end{bmatrix}$$

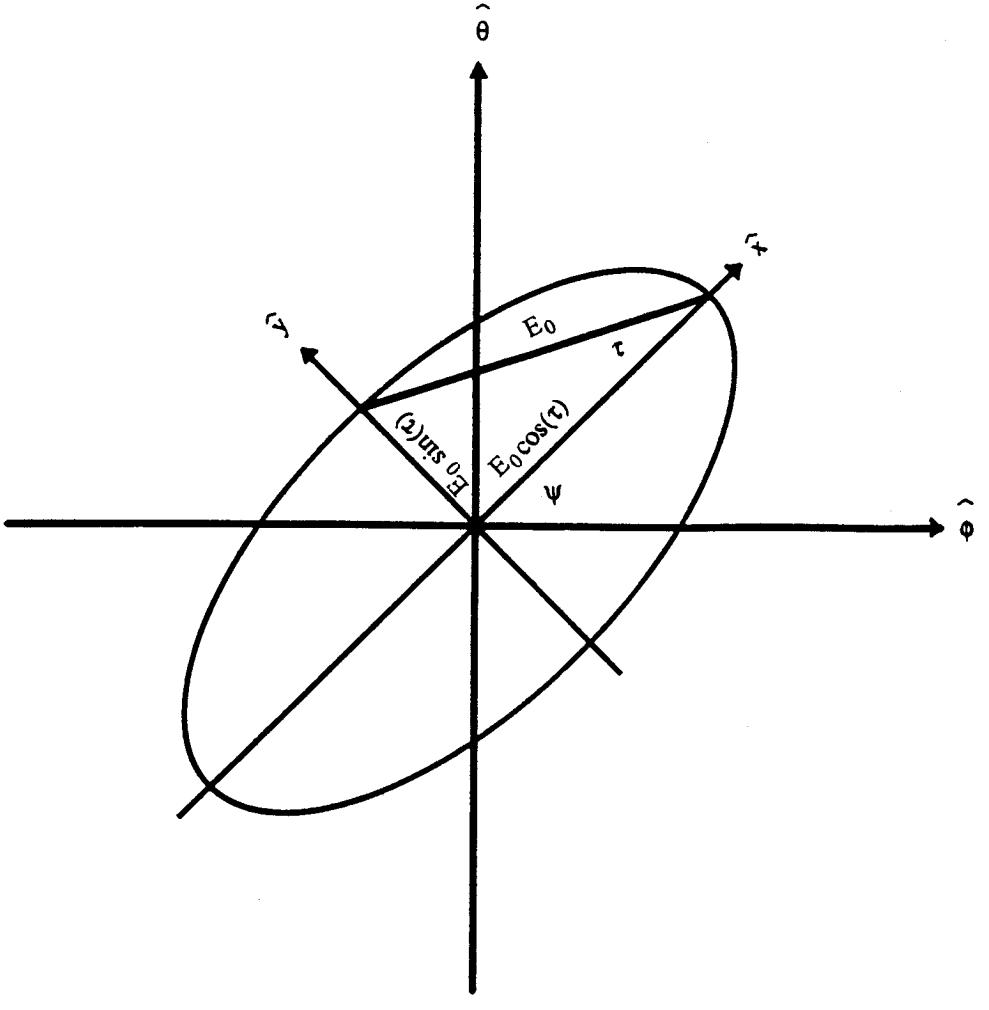

Figure 3.3.1 The polarization ellipse.

and $S_{pq} = E_p^s(\theta_x, \phi_s)/E_q^i(\theta_i, \phi_i)$ where E_q^i and E_p^s denote the incident and the scattered fields with polarization states q and p respectively. Then the received voltage corresponding to transmitting polarization t and receiving polarization r is

$$V_{rt} = [\, a_{r\phi}^* \quad a_{r\theta}^* \,] \begin{bmatrix} S_{\phi\phi} & S_{\phi\theta} \\ S_{\theta\phi} & S_{\theta\theta} \end{bmatrix} \begin{bmatrix} a_{t\phi} \\ a_{t\theta} \end{bmatrix} \tag{3.2}$$

It is clear that both t and r depend on the ellipticity and orientation angles of the transmitting and receiving antennas respectively. The expression for the average received power is

$$\begin{aligned} P_{rt} &= \langle |V_{rt}|^2 \rangle \\ &= \Big\{ |a_{r\phi}|^2 \, \sigma_{\phi\phi}^0 \, |a_{t\phi}|^2 + 2Re\left\{ a_{r\phi}^* \, a_{r\theta}^* \, \sigma_{\phi\phi\theta\theta}^0 \, a_{t\phi} \, a_{t\theta} \right\} \\ &+ 2Re\{ a_{r\phi}^* a_{r\theta}^* \, \sigma_{\phi\theta}^0 \, a_{t\phi} \, a_{t\theta} \} + |a_{r\phi}|^2 \sigma_{\phi\theta}^0 |a_{t\theta}|^2 \\ &+ |a_{r\theta}|^2 \, \sigma_{\theta\phi}^0 \, |a_{t\phi}|^2 + |a_{r\theta}|^2 \, \sigma_{\theta\theta}^0 \, |a_{t\theta}|^2 \Big\} \frac{A}{4\pi R^2} \end{aligned} \tag{3.3}$$

where R is the range from the transmitting antenna to the illuminated area A and σ_{pq}^0 and $\sigma_{\phi\phi\theta\theta}^0$ are the scattering coefficients defined as follows:

$$\sigma_{\phi\phi\theta\theta}^0 = 4\pi R^2 \langle S_{\phi\phi} S_{\theta\theta}^* \rangle / A$$

$$\sigma_{pq}^0 = 4\pi R^2 \langle S_{pq} S_{pq}^* \rangle / A$$

Note that once the antenna coordinates, θ and ϕ, are fixed, the surface scattering matrix defined in terms of them are fixed irrespective of the choice of the transmitting or receiving antenna polarization state which varies only with the angles τ and ψ. Hence, it is possible to determine the response to different polarization states with a given set of S_{pq}'s which is not a function of τ and ψ and varies only with the incident and scattered directions. Since it is a common practice to calculate the scattering coefficients rather than the average power which has range dependence, we shall compute $\sigma_{rt}^0 = 4\pi R^2 P_{rt}/A$. To do so, we need to know all the scattering coefficients which appear in (3.3). All these coefficients were given in section 3.2 except $\sigma_{\phi\phi\theta\theta}^0$. It can be shown by using the field expressions in section 3.2 that

$$\sigma_{\phi\phi\theta\theta}^0 = -\frac{2k^2}{\cos^2\theta} \, e^{-4k^2\sigma^2\cos^2\theta} \sum_{n=1}^{\infty} \frac{(4k^2\sigma^2\cos^2\theta)^n}{n!} \, W^{(n)}(2k\sin\theta, 0) \tag{3.4}$$

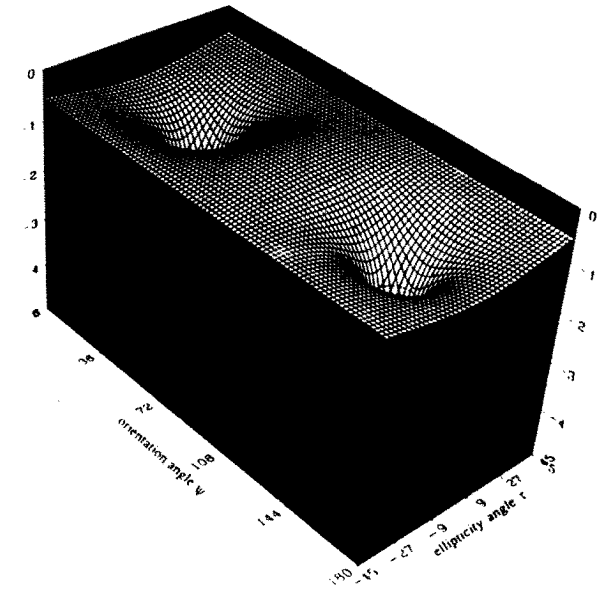

Co-polarized

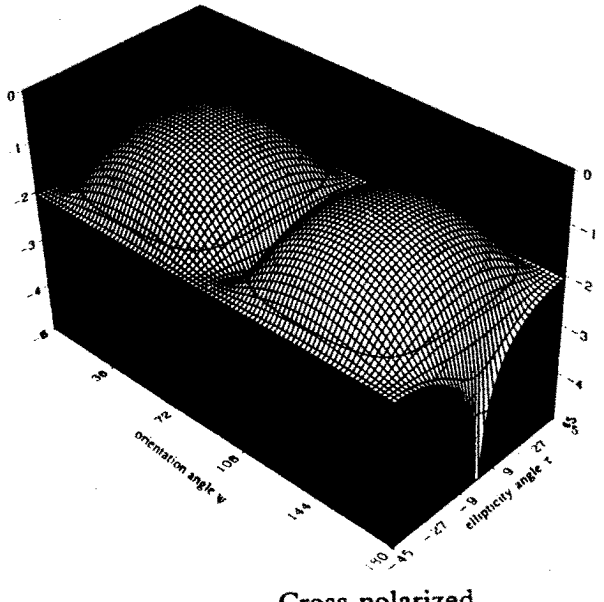

Cross-polarized

Figure 3.3.2 Backscattering coefficient (at 30° of incidence) versus polarization states for an isotropic Gaussian surface with normalized surface roughness parameters $k\sigma = 0.25, kL = 0.69$. (a) Co-polarized, (b) Cross-polarized.

b. Theoretical Calculations

In this section, we use the scattering model developed in section 3.2 and (3.4) to calculate the dependence of the scattering coefficient σ^o_{rt} on the polarization states of the transmitting and receiving antenna in backscattering.

Figures 3.3.2 to 3.3.4 illustrate frequency dependence with $k\sigma$ changing from 0.25 to 2.0 and kL changing from 0.69 to 5.58, a factor of 8. The significant changes with frequency are (a) the like polarization minima move from less than 45° and larger than 135° in orientation angles towards 45° and 135° respectively; (b) the cross polarized scattering coefficient appears to be more peaked at orientation angles around 45° and 135° and ellipticity angles of 0° at larger frequencies and (c) the level difference between VV and HH polarizations decreases with increasing frequency.

3.4 Polarimetric Measurement System and Procedure

a. Scattering Coefficient Measurement System and Approach

The measurements discussed in this chapter were acquired in an indoor range at the University of Texas at Arlington, Wave Scattering Research Center. This bistatic range uses a HP 8510A Network analyzer as the transmit/receive system. The synthesized sweeper was operated from 4 to 18 GHz for these experiments to examine the frequency response of the target of interest. The use of this type of system for RCS measurements makes it possible to vectorially remove signal reflections from the floor, ceiling, and walls of the chamber, along with the pedestal support. This also provides the ability to acquire measurements of targets which usually would be lost in the noise floor. Although these type of subtraction methods are very useful, care must be taken to make sure that the target being measured does not significantly modify the characteristics of the empty chamber. The HP8510A analyzer allows the frequency and time domain information to be displayed simultaneously. The analyzer takes the frequency data and uses a chirp-Z transform to obtain the time domain response of the target. The resolution and the unaliased time window width are determined by the number of frequency points and the bandwidth swept. The network analyzer contains gating features that can be used to isolate regions in the time domain, which make it possible to analyze isolated regions

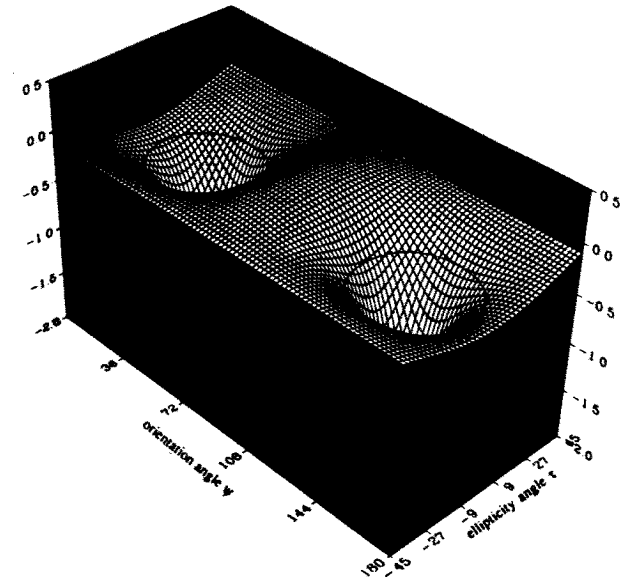

Co-polarized

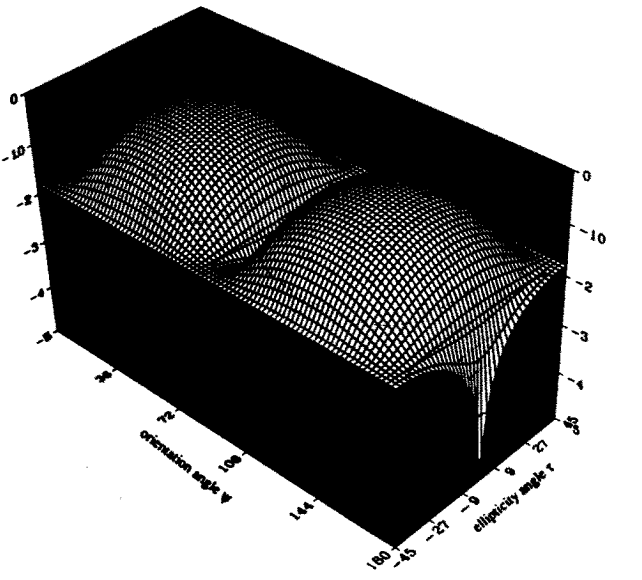

Cross-polarized

Figure 3.3.3 Backscattering coefficient (at 30° of incidence) versus polarization states for an isotropic Gaussian surface with normalized surface roughness parameters $k\sigma = 1.0, kL = 2.78$. (a) Co-polarized, (b) Cross-polarized.

of a device or target by gating out unwanted effects in the frequency domain response.

Figure 3.4.1 presents the major components of the Radar Cross Section Measurement Facility. A diagram of the radar measurement system comprised of a Hewlett/Packard Network Analyzer and Hewlett/Packard Synthesized Sweeper configured into a RCS test set is shown in Fig. 3.4.2. The transmit and receive antennas are dual polarized conical horns. These antennas operate in the 2 to 20 GHz range. The antennas have been tested and shown to have very good polarization isolation properties (greater than 25dB to 30dB across the frequency band of interest). The transmit and receive antennas were identical. The one way power beamwidths of the antennas were 12° and 14° at 12 and 8 GHz respectively. The antennas were directionally calibrated using light beams to align the antennas on the pedestal target position.

An HP 9000/310 is used as the controlling computer for the measurement system. This controller is needed to construct the calibration data set for the 1-port error correction method used in the RCS measurements. The controlling computer saves the calibration sets which can be restored to the 8510 system by the use of the HP-IB data bus.

The radar cross section of a particular target is a function of the polarization of the incident and received waves. It is convenient to use a scattering matrix S to describe the interaction between the incident wave and target. This matrix relates the scattered field, $\overline{E}_s$ to the incident field, $\overline{E}_i$ component by component. In matrix notation (Blanchard *et al.*, 1988),

$$\begin{bmatrix} E_1^s \\ E_2^s \end{bmatrix} = [S] \begin{bmatrix} E_1^i \\ E_2^i \end{bmatrix} \tag{4.1}$$

where

$$[S] = \begin{bmatrix} a_{11} & a_{12} \\ a_{21} & a_{22} \end{bmatrix} \tag{4.2}$$

The subscripts 1 and 2 represent any two orthogonal polarization components of the fields and a_{ij}'s are normally complex quantities. These a_{ij} elements contain both amplitude and phase information such that

$$[S] = \begin{bmatrix} |a_{11}|e^{i\phi_{11}} & |a_{12}|e^{i\phi_{11}} \\ |a_{21}|e^{i\phi_{21}} & |a_{22}|e^{i\phi_{22}} \end{bmatrix} \tag{4.3}$$

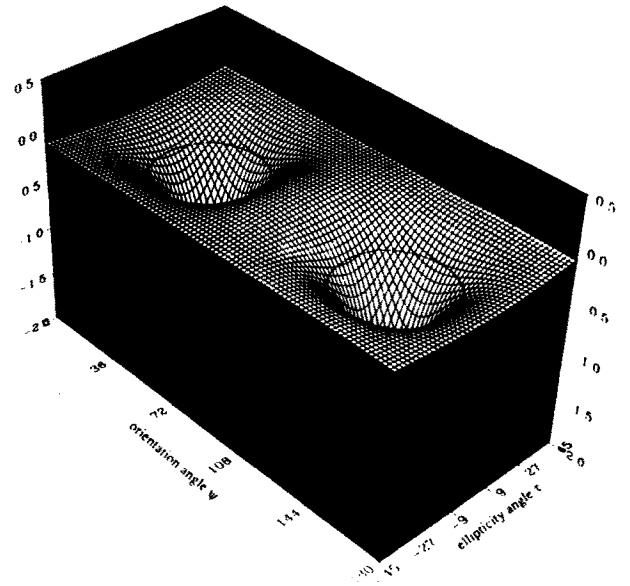

Co-polarized

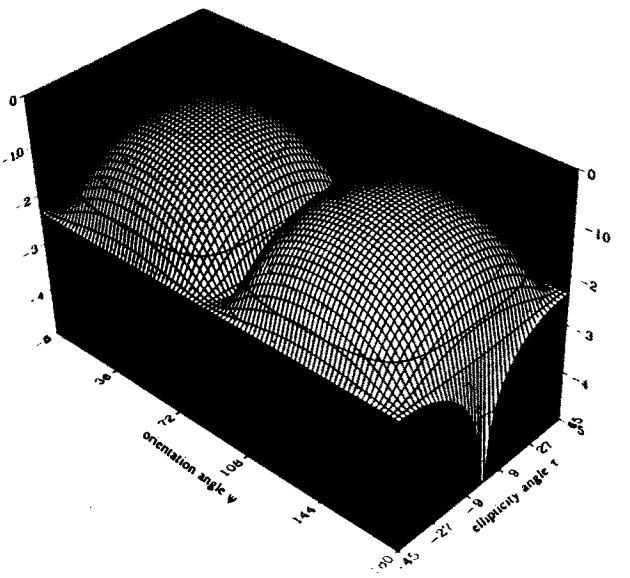

Cross-polarized

Figure 3.3.4 Backscattering coefficient (at 30° of incidence) versus polarization states for an isotropic Gaussian surface with normalized surface roughness parameters $k\sigma = 2.0, kL = 5.58$. (a) Co-polarized, (b) Cross-polarized.

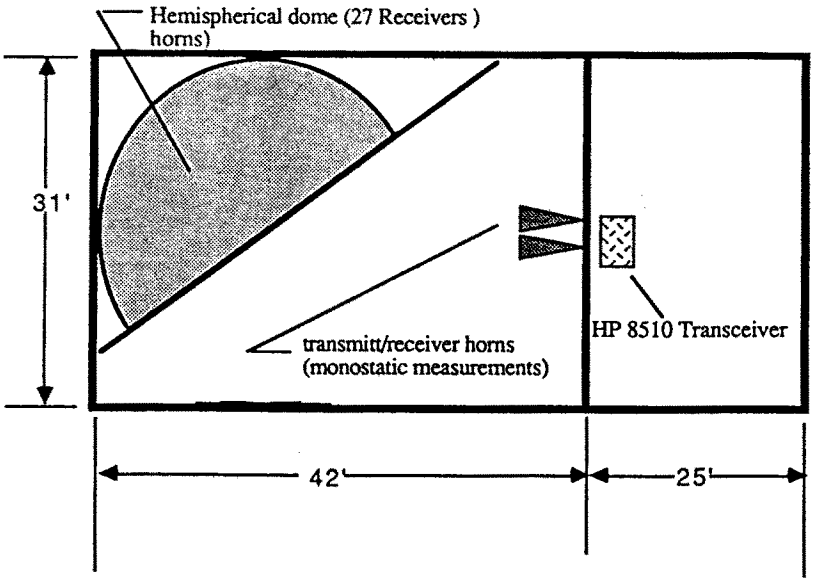

Measurement Facility Plan View

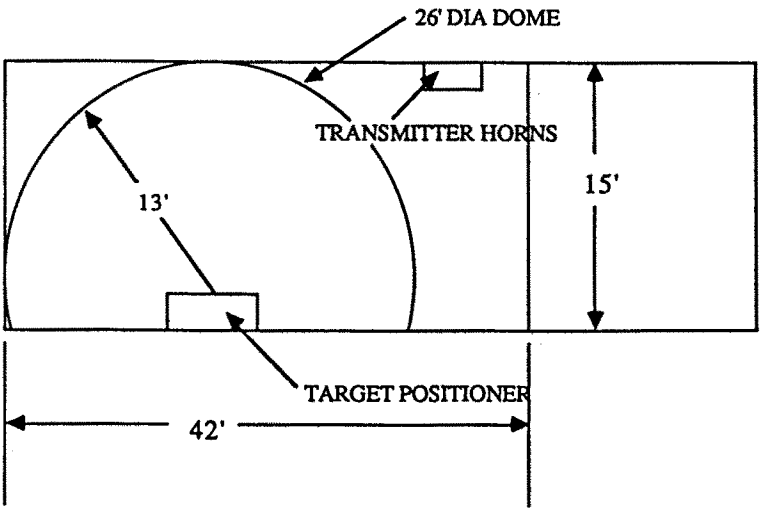

Measurements Facility Elevation View.

Figure 3.4.1 General System Diagram.

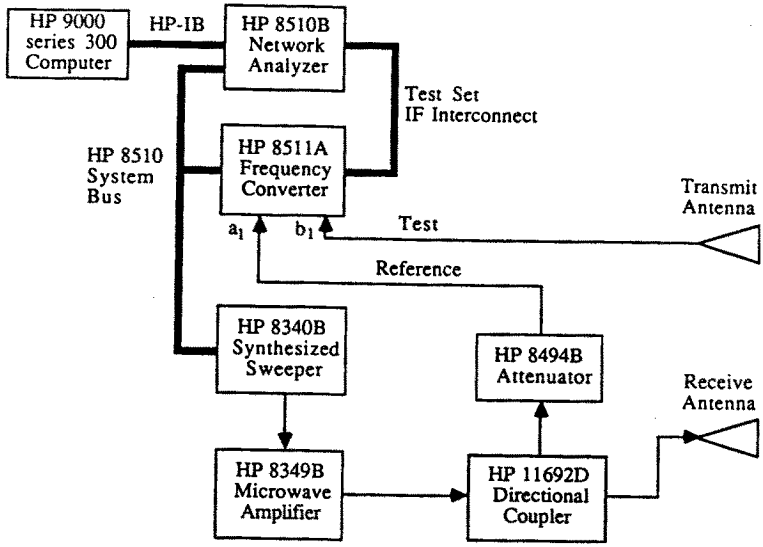

Figure 3.4.2 RCS Test set using the HP 8510A.

The components of S are related to the measured radar cross section by

$$\sigma_{ij} = 4\pi R^2 |a_{ij}|^2 \tag{4.4}$$

All information on the scattering properties of a specific target and orientation with respect to the radar are contained in the scattering matrix. If S is completely specified for a particular frequency, target, and orientation between target and transmit-receive antennas, the radar cross section of the target can be computed for any combination of polarizations.The distributed target monostatic radar equation for identical transmit and receive antennas is given by

$$P_r = \frac{\lambda^2 P_t g^2}{(4\pi)^3} \int_A \frac{g^2(\theta,\phi)\sigma^0}{R^4} dA \tag{4.5}$$

where P_t is the transmitted power, G is the maximum gain of the antennas, $g(\theta,\phi)$ the normalized radiation pattern, R is the range to the target, dA an elemental surface area and σ^o is the differential scattering coefficient of the target. Additional variables can be included in the

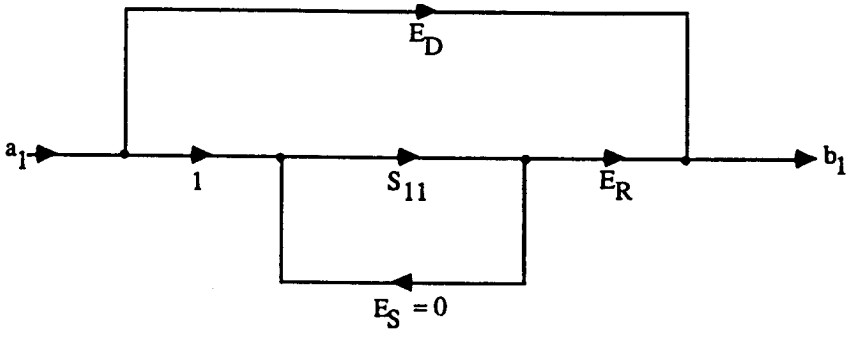

where the error terms: E_D = Directivity
E_R = Reflection Tracking
E_S = Source Match

1-Port Calibration Model Diagram

Figure 3.4.3 Signal Flow Diagram.

radar equation to account for losses in the system. These effects can also be included into the system constant which relates the returned power to the radar cross section of the target.

The calibration of the indoor range using the FM-CW system requires a calibration of amplitude and phase for each of the frequencies in the swept band. The calibration procedure uses the point target calibration reference of a metal sphere. Equation 4.5 for the distributed target simplifies for a point target because the range and antenna patterns are constant and can be removed from the integral and the differential cross section integral becomes the cross section, σ, which has the units of square meters. The point target calibration groups the system parameters into a system constant to relate the power received to the cross section of the target. The system constant for the HP 8510A system is a complex constant which not only corrects the returned signal for intensity level, but also for relative phase of the signal to the reference signal. These complex constants provide for the vector subtraction of background signals and the reference values for the magnitude and phase for the measurement system.

System calibration terms must be constructed for each of the 401

frequency points occurring in the selected frequency range. The calibration of the HP 8510A Network Analyzer radar system uses the built in error correction techniques for a 1-port calibration. The external computer is needed to construct the calibration data set and load this data set into one of the calibration sets in the 8510A system. After this is accomplished, the external controller is not needed. The signal flow graph diagram for the 1-port calibration model is shown in Fig. 3.4.3 which shows the relation between the measured and actual values using the 1-port vector correction. The a_1 and the b_1 labels on the diagram represent the two ports on the HP 8511A frequency converter. The a_1 channel is the reference channel which uses the reference RF source to maintain the phase lock and tracking capabilities of the system. The 1-port calibration model for cross section measurements uses two of the three error terms of the standard single port calibration. The error term for the source match, E_S, of the port is assumed to be zero.

The calibration description for the VV and HH polarization states follows. The first step in the calibration process is to set up a file containing the theoretically calculated backscatter values for the reference target. The file containing the calculated backscatter values for the sphere was used for both the VV and HH polarization calibrations due to the symmetry of the reference target. The second step in the calibration process is to set up the empty chamber with the target support and take a measurement of this configuration. This measured response produces the error term labeled E_D from Fig. 3.4.3. The final error term, E_R, can be found by subtracting E_D from the measured value of the reference sphere and then dividing by the calculated theoretical values for the sphere.

$$E_R = \frac{S_{11M} - E_D}{S_{11\text{Theo}}} \tag{4.6}$$

The measured value for the reference sphere is found by measuring the reference sphere in the chamber, and subtracting the empty chamber response. Each error term is a vector array for all points in the frequency band of interest. The error term arrays contain the magnitude and phase values used in the vector correction of the reflections from the chamber and the calibration of the system parameters. The calibration data set containing the three error arrays is loaded into the HP 8510A Network Analyzer through the HP-IB data bus.

The cross polarization measurements can be calibrated using exactly the same procedure as in like polarization. A sphere can again

be used as the calibration target in bistatic measurements. However, if cross polarized data are taken in backscattering, a different calibration target such as a cylinder must be used since the sphere does not depolarize in the backscattering direction. The effects of antenna coupling did not affect the measurements due to the large difference in path lengths for the feed through and target returns, which made it possible to remove these effects with the time gating features of the system.

Therefore, using the data acquired from the measurements of the empty chamber, the calibration sphere and the theoretical calculations of the reference target, the expressions for the scattering cross section of any unknown target can be referenced by the corrections specified by the calibration target. The measured cross section is related to the actual cross section as:

$$S_{11M} = E_D + \frac{S_{11A} E_R}{1 - E_S S_{11A}} \tag{4.7}$$

where S_{11M} is the measured response, and S_{11A} is the actual cross section of the target. The actual cross section of the target can be found from the previous equation with the source match error term set to zero as was assumed earlier.

$$S_{11A} = \frac{S_{11M} - E_D}{E_R} \tag{4.8}$$

The measurements are referenced to cross section in square meters (Equation 4.2), therefore the scattering coefficient parameter must be calculated from the cross section by referencing the measurement with the effective area of the target. The differential scattering coefficient is determined for area extensive targets by dividing the cross section by the effective area of the target. From Equation (4.1), if the scattering coefficient is assumed to be constant over the target area and the range variable considered constant due to far field conditions, the scattering coefficient and the range terms can be removed from the integral. The system constants can be grouped together with the return power to find the backscattering cross section, and the integral containing the antenna pattern and the differential area can be evaluated to find the effective area of the target. This makes it possible to convert the measured parameter of the backscattering cross section to the backscattering coefficient as shown in Equation (4.9).

$$\sigma^0 = \frac{\sigma}{A_{\text{effective}}} \tag{4.9}$$

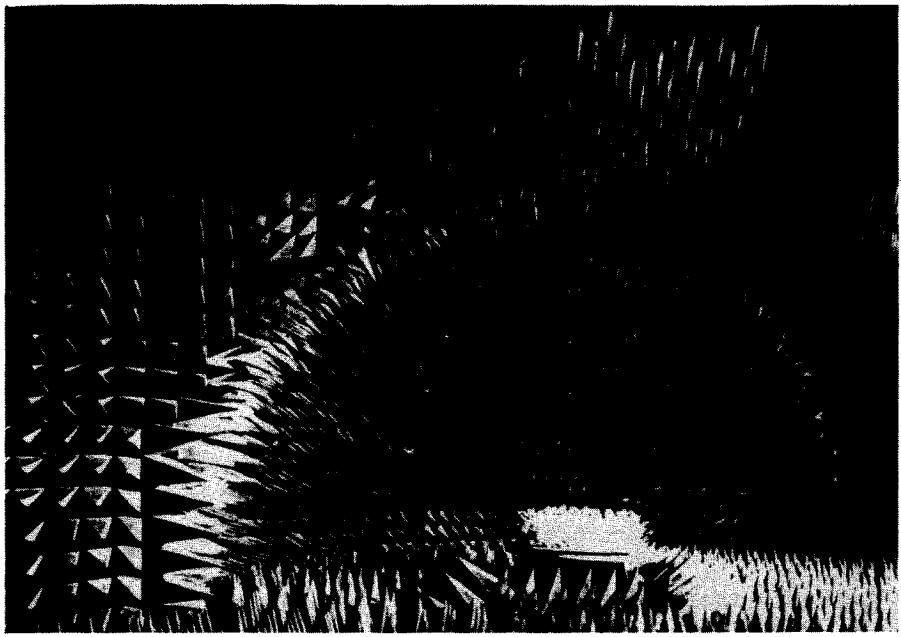

Figure 3.4.4 Photograph of the Bistatic Facility.

b. Imaging Measurement System and Approach

The imaging radar system used for these experiments is designed around the same HP 8510A network analyzer as the RCS facility. The 8510 system is chosen for several reasons: the phase stability of the system is very good, as are the repeatability of phase lock and frequency steps. The phase distortion, and hence the fidelity of the final image, is critically dependent on this scan-to-scan fidelity. Also a large number of measurement points can be handled by the 8510 system. Furthermore, by combining subsets of the desired bandwidth, virtually any bandwidth requirements can be met.

A simple configuration of the HP 8510 measurement system was shown in Fig. 3.4.2. This system is operating over a bandwidth of 2 to 18 GHz, and it consists of the network analyzer, frequency synthesizer source, variable attenuator, broadband directional coupler, transmitter and receiver antennas, and the frequency converter.

The HP 8510 measurement system is controlled by a HP 9000 series 310 computer. This computer is required to run the data acquisition process. Its tasks include controlling the 8510 measurement system,

calibration, and target measurement modes, as well as controlling the positioner, the polarization states of the antennas, and the RF transfer switches.

All the measurements within the experiments were done in the bistatic anechoic chamber of the Wave Scattering Research Center at the University of Texas at Arlington. A photograph of the facility is shown in Fig. 3.4.4. The anechoic chamber houses 27 bistatic receive antennas mounted on a 26 foot diameter 1/4 geodesic dome. The configuration of these antennas is shown in Fig. 3.4.5.

The measurement configuration for the imaging mode is shown in Fig. 3.4.6. The target is rotated through the desired azimuth angle to synthesize the receiver aperture. For each azimuth angle, the data is acquired over the desired frequency bandwidth. A single look angle is sufficient to produce a projection of the reflectivity function. However, to produce a three dimensional image of the object, several look angles are required. This means that several different receive antennas must be chosen, and the acquisition procedure must be repeated for every one of them. In these experiments, data is taken for only a single transmit/receive configuration.

The data recorded by the imaging system has the form:

$$\psi(f,\phi) = KA\exp[-jK(R_t + R_r)]\,G(f,\phi)\,T(f,\phi) + C(f,\phi) \quad (4.10)$$

where

$T(f,\phi)$ = the transfer function of the measurement system.
$C(f,\phi)$ = the clutter due to the chamber and positioner.
$\psi(f,\phi)$ = the measured data.
$G(f,\phi)$ = the scattered far field of the object reflectivity function.
R_t = the distance from transmitter to the scattering center of the object.
R_r = the distance from receiver to the scattering center of the object.

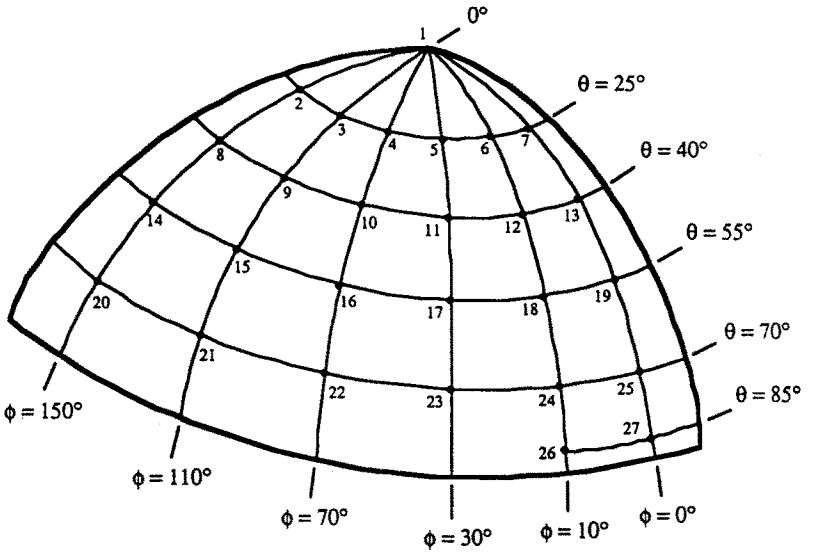

Bistatic Receive Antenna Mounting Structure and Placement

Figure 3.4.5 Receiver Horn Configuration.

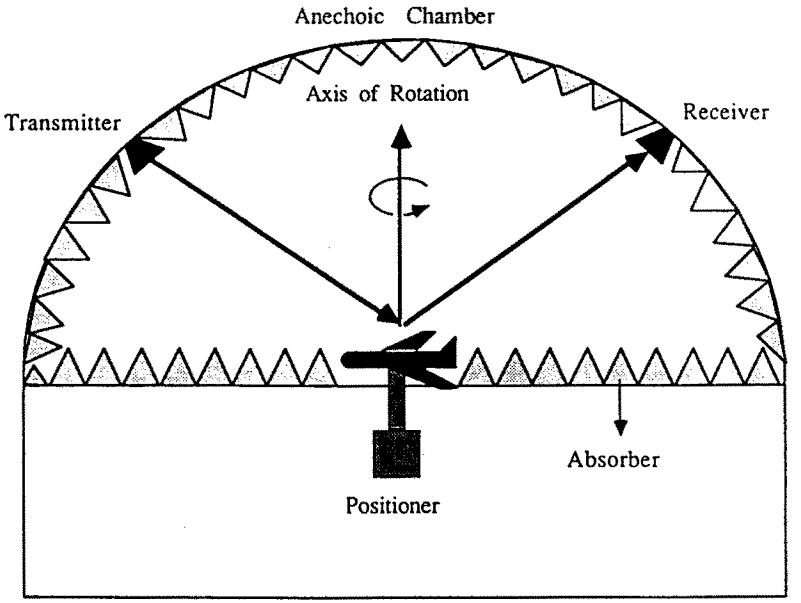

Measurement Hall Configuration

Figure 3.4.6 Imaging Mode Measurement Configuration.

The desired term in equation (4.10) is $G(f,\phi)$, which is the scattered far field of the object. Two sets of calibration measurements are needed to recover $G(f,\phi)$ from equation (4.10). The first one, $C(f,\phi)$, is the response of the clutter. It is determined from the empty chamber measurement. This corresponds to the E_r term in Equation 4.6 previously discussed. The second one, $T(f,\phi)$, is the system response, corresponding to the previously introduced E_s term. To determine $T(f,\phi)$, a calibration measurement is made using a scatterer for which the theoretical scattered fields are known. For the bistatic measurements, a sphere is used to determine all four scattered field terms (HH, VV, HV, VH). The difference between the actual measurement and the theoretical values yields the contribution of the system. The HP 8510A is programmed to store the values of $C(f,\phi)$ and $T(f,\phi)$, and to calculate $G(f,\phi)$ automatically from the measured data.

For imaging an extended target (target contains resolvable scattering centers), the distance $R_t + R_r$ must be determined from the measurement. $R_t + R_r$ is the range to the effective phase center of the object, and it must be determined at every aspect angle. HP 8510A automatically takes the scattering center of the reference sphere as the common reference point for all azimuth angles.

3.5 Scattering from Statistically Known Surfaces

In recent years, numerical simulation of waves scattered from computer generated random surfaces has been used in the verification of surface scattering models and in studying the scattering characteristics of rough surfaces [Fung and Chen, 1985, Chen and Fung, 1988, Thorsos, 1988, Wu, *et al.* 1988]. The simulation technique involves solving the integral equation for the induced surface current density on a patch of computer generated rough surface due to an impinging plane wave by the method of moments. Then the far zone scattered field and subsequently the scattered power are computed. Finally, the scattering coefficient is obtained by averaging over a large number of normalized power calculations from an ensemble of rough surface patches. If the size of the illuminated patch is $N \times N$, there are $2N^2$ unknown surface current density components and it requires inverting a matrix of size $2N^2 \times 2N^2$ to determine the $2N^2$ unknowns. For N equal to 100 this is a 20000×20000 matrix. Clearly, it is impractical to invert a matrix this large. For this reason, only two-dimensional surface scattering

simulation problem has been done. On the other hand to consider the cross polarization effect in rough surface scattering, three-dimensional simulation problem must be carried out. Thus, an alternative approach must be devised to obtain a satisfactory estimate of the surface current density.

Based upon the rough surface scattering model recently developed by Fung and Pan (1987), a satisfactory approach is to solve the surface current integral equation iteratively. To check for the number of iterations necessary to achieve convergence to a satisfactory solution, we shall first apply it to the two-dimensional problem and compare its results with the corresponding calculations using the standard moment method. Once the necessary number of iterations is known, the identical approach is applied to the three dimensional surface scattering problem.

In what follows, an iterative solution of the integral equation for the surface current density is validated in two-dimensional scattering problems. This is followed by section 3.5b on a method for generating randomly rough surfaces with specified correlation functions for three-dimensional scattering problems. Finally, the three-dimensional surface scattering problem is studied using the surface current obtained by the iterative solution of the integral equation in section 3.5c. Results obtained are compared with the surface scattering model predictions in section 3.2 and measurements acquired as described in section 3.4.

a. An Iterative Solution of the Surface Current Density

In this section, the iterative solution of the surface current integral equation is verified numerically by comparing the backscattering coefficient calculated from it with the corresponding calculations based on the moment method. Since the moment method simulation is only feasible for scattering problems in two dimensions, we have to reduce the integral equation approach in section 3.2 to two-dimensional form. For ease of reference, a brief description of the procedure to obtain the final analytical form for "simple Gaussian surfaces" and "two-scale Gaussian surfaces" will be presented. Then, comparisons of the backscattering coefficient between the theoretical model in section 3.2 and the moment method simulation for the above two types of surfaces will follow.

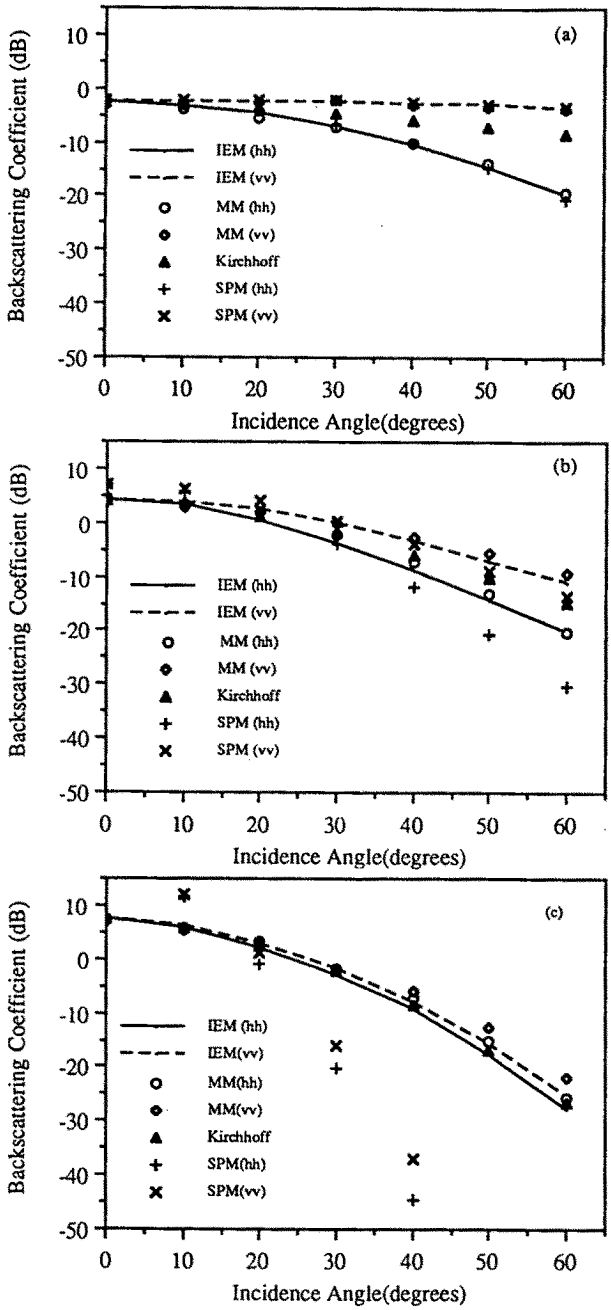

Figure 3.5.1 Comparison of backscattering coefficients between the Integral Equation Model (IEM) and the moment method simulation (MM) for a single scale Gaussian surface whose rms slope $\sigma_s = 0.253 (L = 2.0, \sigma = 0.358)$ (a) For $\lambda = 9$ units, $K\sigma = 0.25$, $KL = 1.396$. (b) For $\lambda = 4.5$ units, $K\sigma = 0.5$, $KL = 2.792$. (c) For $\lambda = 2.25$ units, $K\sigma = 1.0$, $KL = 5.584$.

a.1 Two-dimensional scattering problem

From Poggio and Miller[1973] and the scattering geometry in Fig. 3.2.1, the governing integral equation of the surface current density induced by an impinging plane wave over a perfectly conducting, rough surface in two dimensions is,

$$\frac{\overline{J}}{\cos\chi} = 2\overline{n} \times \overline{H}^i + \frac{1}{2\pi} \int_S \overline{n} \times \nabla G \times \left(\frac{\overline{J}'}{\cos\chi'}\right) dx' \qquad (5.1)$$

where $\cos\chi = (1 + Z_x^2)^{-1/2}$, Z_x is the slope of the surface, G is the Greens's function, $G = \frac{-j}{4} H_0^{(2)}(k|\overline{p} - \overline{p}')$ and $\overline{H}^i$ is the incident magnetic field intensity. Note that $\overline{n} = -\hat{x}Z_x + \hat{z}$ is the surface normal vector. The first iterative solution for the surface current is to substitute the unknown current density under the integral sign by $\overline{J}' = 2\overline{n} \times \overline{H}^i$. The second iteration is obtained from (5.1) by substituting the first iterative solution into the unknown current density under the integral sign and higher order iterations are carried out in a similar manner. When only the first order iteration is carried out, an analytical solution is possible as demonstrated in section 3.2. To obtain a higher order iterative solution one must resort to numerical evaluation. To carry out the solution using the first order iteration, we replace the Green's function by its spectral representation in (5.1) and write the current density for horizontally polarized incident field as

$$\begin{aligned}\frac{\overline{J}^h}{\cos\chi} =& \hat{y}\left\{\frac{2E_0}{\eta}(Z_x \sin\theta + \cos\theta)e^{-jk_x x - jk_z z}\right. \\ & -\frac{E_0}{\pi\eta}\left[\int e^{-jk_x x' - jk_z z'} \int \left[-\frac{uZ_x \cos\theta}{q} \pm (Z_x' \sin\theta + \cos\theta)\right]\right. \\ & \left.\left. \cdot e^{ju(x-x') - jq|z-z'|} du\, dx'\right]\right\} \qquad (5.2a)\end{aligned}$$

Note that in (5.2a), the upper sign of the term with sign is applicable to $z < z'$ and the lower sign to $z > z'$. To simplify the evaluation of the scattered field and the scattering coefficient, the following simplifying assumptions are made.

1. For random surfaces, the probability of having $z > z'$ and $z < z'$ are equally likely, i.e., terms with $\pm$ signs can be ignored due to the cancellation of positive contributions over $z < z'$ by the negative contributions over $z > z'$.
2. The phase term, $-jq|z-z'|$ can be ignored since within one correlation distance the difference between z and z' is small and when the spacing between points is large the resulting power is small.

Under these simplifying assumptions, the current density for horizontally polarized incident field reduces to

$$\frac{\overline{J}^h}{\cos\chi} = \hat{y}\left\{\frac{2E_o}{\eta}(Z_x \sin\theta + \cos\theta)e^{-jk_x x - jk_z z} + \frac{E_0}{\pi\eta}\left[\int e^{-jk_x x' - jk_z z'} \int \frac{uZ_x \cos\theta}{q}\, e^{ju(x-x')} du\, dx'\right]\right\} \tag{5.2b}$$

For vertically polarized incident field, the approximate current density with and without making assumptions 1 and 2 are given by (5.3a) and (5.3b) respectively:

$$\frac{\overline{J}^v}{\cos\chi} = \frac{2E_0}{\eta}(\hat{x} + \hat{z}Z_x)e^{-jk_x x - jk_z z} - \frac{E_0}{\pi\eta}\left[\int (\hat{x} + \hat{z}Z_x') e^{-jk_x x' - jk_z z'} \int \left(-\frac{uZ_x}{q} \pm 1\right) e^{-jk_z(z-z') + ju(x-x')} du\, dx'\right] \tag{5.3a}$$

$$\frac{\overline{J}^v}{\cos\chi} = \frac{2E_0}{\eta}(\hat{x} + \hat{z}Z_x)e^{-jk_x x - jk_z z} + \frac{E_0}{\pi\eta}\left[\int e^{-jk_x x' - jk_z z'} \cdot \int \left(-\frac{uZ_x}{q}\right) e^{-ju(x-x')} du\, dx'\right] \tag{5.3b}$$

The far zone scattered field can be calculated through the following integration over the illuminated length,

$$\overline{E}(\overline{\rho}) = -C\eta \int \{\hat{\rho}\,[\hat{\rho}\cdot\overline{J}] - \overline{J}\}\, e^{jk\hat{\rho}\cdot\overline{\rho}} dx \tag{5.4}$$

where $\hat{\rho}$ is the unit vector along the direction of observation and for backscattering, $\hat{\rho} = -\hat{x}\sin\theta + \hat{z}\cos\theta$. The constant $C = \sqrt{\frac{k}{8\pi\rho}}\, e^{-j(k\rho - \pi/4)}$. After substituting the current density for both polarizations in (5.4), the polarized backscattered fields E^s_{vv} and E^s_{hh} for vertical and horizontal polarizations can be obtained. Following the same

procedure as in Fung and Pan [1987], the backscattering coefficient σ^0_{pp}, where the subscripts denote either vv or hh, can be written as

$$\begin{aligned}\sigma^0_{pp} = &\frac{k}{\cos^2\theta} e^{-4k_z^2\sigma^2} \sum_{n=1}^{\infty} \frac{(4k_z^2\delta^2)^n}{n!} W^{(n)}(2k\sin\theta) \\ &\pm 4k\tan^2\theta e^{-3k_z^2\sigma^2} \sum_{n=1}^{\infty} \frac{(2k_z^2\delta^2)^n}{n!} W^{(n)}(2k\sin\theta) \\ &+4k\tan^2\theta\sin^2\theta e^{-2k_z^2\sigma^2} \sum_{n=1}^{\infty} \frac{(k_z^2\sigma^2)^n}{n!} W^{(n)}(2k\sin\theta)\end{aligned} \tag{5.5}$$

In (5.5), the upper sign of the $\pm$ term is for vv polarization while the lower sign is for hh polarization. The symbol $W^{(n)}(2k\sin\theta)$ is the Fourier transform of the n^{th} power of the correlation function $\rho(\zeta)$, i.e.,

$$W^{(n)}(2k\sin\theta) = \int e^{j2k\sin\theta\zeta} \rho^n(\zeta) d\zeta \tag{5.6}$$

For a Gaussian correlation function, $\rho(\zeta) = e^{-\zeta^2/L^2}$

$$W^{(n)}(2k\sin\theta) = \sqrt{\frac{\pi}{n}} L \exp\left(-\frac{k^2\sin^2\theta L^2}{n}\right). \tag{5.7}$$

By superimposing two independent random surfaces with Gaussian correlations, the "two-scale Gaussian surface" can be constructed. The correlation of this surface can be written as

$$\rho(\zeta) = a e^{-\zeta^2/L_1^2} + b e^{-\zeta^2/L_2^2} \tag{5.8}$$

where L_1 and L_2 are the correlation lengths associated with the two scales. The constants $a = \sigma_1^2/\sigma_t^2$, $b = \sigma_2^2/\sigma_t^2$, $\sigma_t^2 = \sigma_1^2 + \sigma_2^2$, where σ_1^2 and σ_2^2 are the surface variances of the two scales respectively. For this correlation,

$$\begin{aligned}W^{(n)}(k) = &\sum_{m=0}^{n} \binom{n}{m} a^{n-m} b^m \sqrt{\pi} \frac{(kL_1)(kL_2)}{k\sqrt{(n-m)(kL_2)^2 + m(kL_1)^2}} \\ &\cdot \exp\left[\frac{(kL_1)^2(kL_2)^2\sin^2\theta}{(n-m)(kL_2)^2 + m(kL_1)^2}\right]\end{aligned} \tag{5.9}$$

a.2 Results and discussions

In this section, the results of the comparison between the theory using the first-order iterative solution and the moment method simulation (Fung and Chen, 1985) are presented. It is shown that for the cases considered only one iteration is needed. Thus, additional evaluations by numerical means using higher order iterative solutions are not necessary. The cases considered below include frequency responses for two types of surfaces, i.e., the single scale Gaussian surface and the two-scale Gaussian surface.

a.2.1 Single-scale Gaussian surface

A Gaussian surface with $\sigma = 0.358$, $L = 2.0$ units (or the rms slope $\sigma_s = 0.253$) is generated on the computer. A method to generate such a surface in two-dimensions has been given by Fung and Chen [1985]. A generalization of this surface generation scheme to surfaces in three-dimensions is given in section 3.5b. The moment method simulation with wavelengths of 9.0, 4.5 and 2.25 units are performed on the surface. The simulated backscattering coefficient along with the integral equation model calculations (abbreviated in the figures as IEM) for the three wavelengths are plotted in Figs. 3.5.1(a) through 3.5.1(c). In addition to the current model, the results of first-order small perturbation model (abbreviated in the figures as SPM) and Kirchhoff solution are also plotted to serve as references. In Fig. 3.5.1(a), excellent agreements between the moment method simulation and the current model denoted by IEM can be seen. It is also noted that the values of $k\sigma$ and kL are 0.25 and 1.396 which satisfy the conditions of the first-order small perturbation [Ulaby *et al.*, 1982]. The agreement between the small perturbation and the current model also indicates that the current model is valid in the low frequency region. In Fig. 3.5.1(c), the values of $k\sigma$ and kL are 1.0 and 5.584 which satisfy the conditions of the Kirchhoff approximation. The agreement between simulation, IEM and the Kirchhoff model indicates that IEM is also valid in the high frequency region. In Fig. 3.5.1(b), in the intermediate frequency region, the values of $k\sigma$ and kL of the surface are 0.5 and 2.792 respectively. In this region, neither the Kirchhoff model nor the first-order small perturbation model is valid. This is clearly demonstrated by the comparison of the results of simulation with the Kirchhoff and the first-order small perturbation models in Fig. 3.5.1(b). The agreement

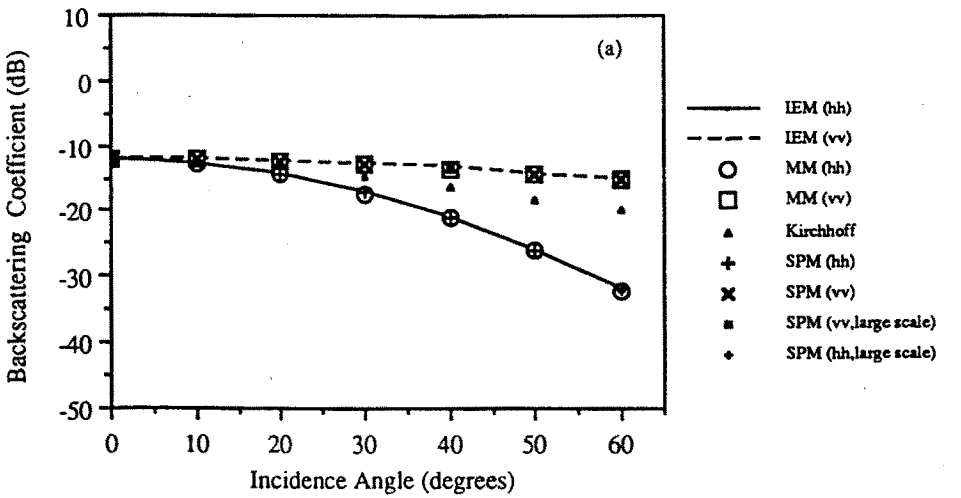

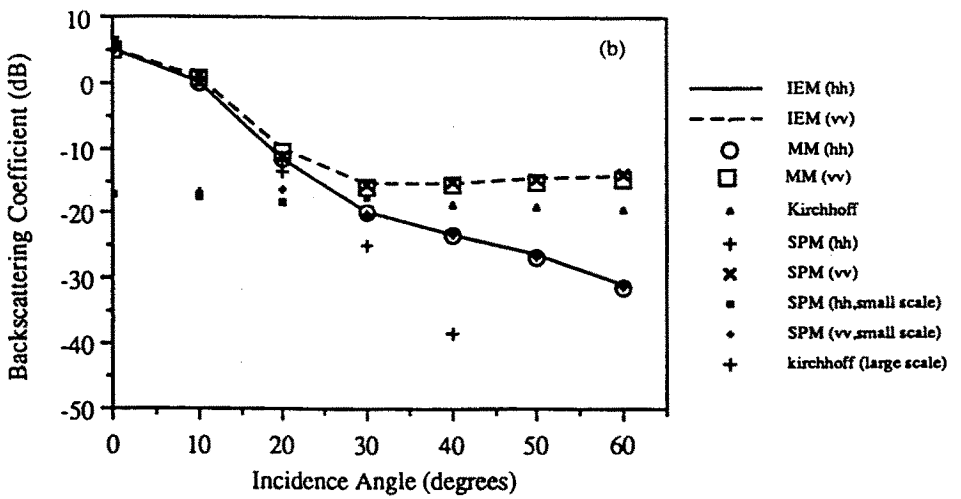

Figure 3.5.2 Continued.

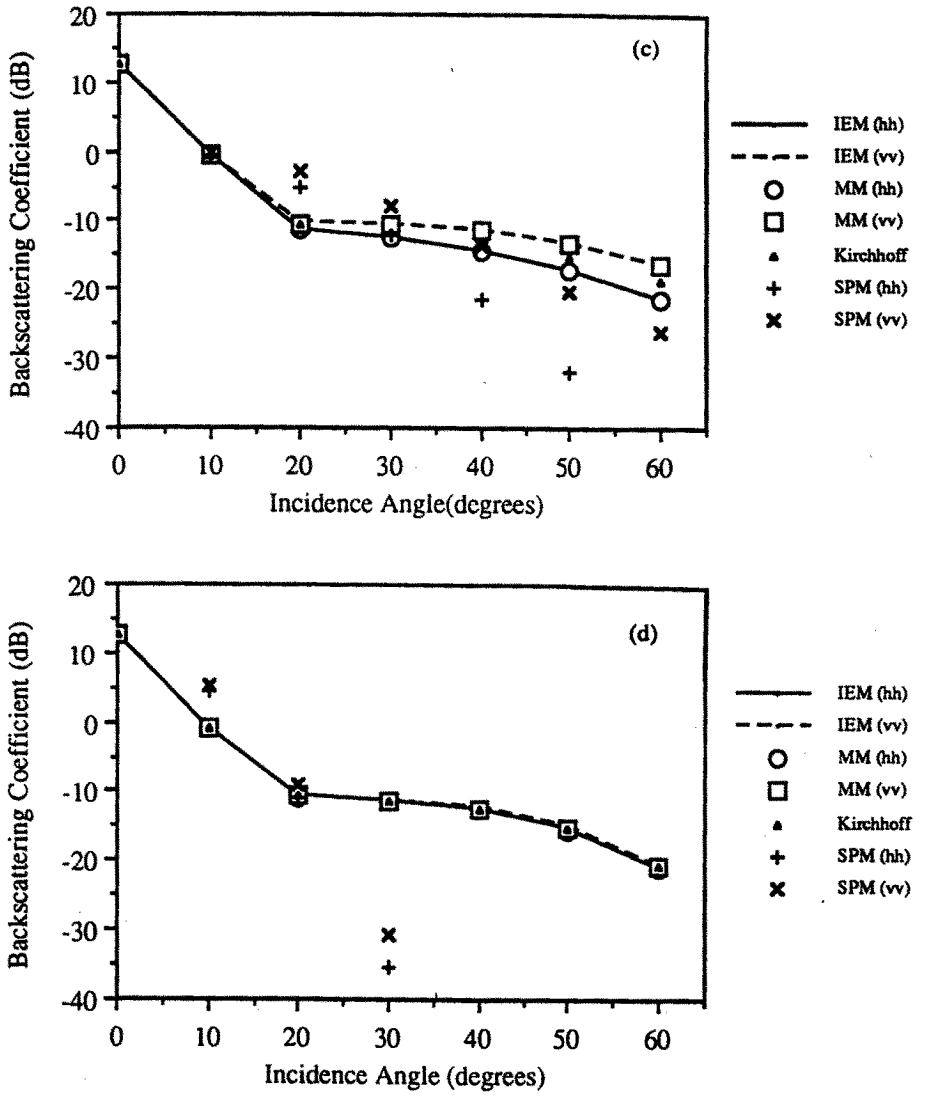

Figure 3.5.2 Comparison of backscattering coefficients between the Integral Equation Model (IEM) and the moment method simulation(MM) for a two-scale Gaussian surface. The roughness parameters of the surface are $\sigma_1 = 0.0764$, $L_1 = 1.0$, $\sigma_2 = 0.382$, $L_2 = 8.0$ (a) For *lambda* $= 32$ units, $K\sigma_1 = 0.015$, $KL_1 = 0.196$, $K\sigma_2 = 0.075$, $KL_2 = 1.57$. (b) For $\lambda = 8$ units,$K\sigma_1 = 0.06$, $KL_1 = 0.78$, $K\sigma_2 = 0.3$, $KL_2 = 6.28$. (c) For $\lambda = 4$ units, $K\sigma_1 = 0.12$, $KL_1 = 1.57$, $K\sigma_2 = 0.6$, $KL_2 = 12.56$. (d) For $\lambda = 2$ units, $K\sigma_1 = 0.24$, $KL_1 = 3.14$, $K\sigma_2 = 1.2$, $KL_2 = 25.12$.

between the simulation and IEM in Fig. 3.5.1(b) indicates that IEM is superior to both the Kirchhoff and the small perturbation models in that it not only encompasses both the high and low frequency regions, but it is also applicable in the intermediate frequency region. The validity of IEM as a working model for all frequencies on single scale Gaussian surface is thus confirmed.

a.2.2 Two-scale composite surface

A two-scale surface is constructed by superimposing two independent Gaussian random profiles with surface height standard deviation $\sigma_1 = 0.0764$ unit, correlation length $L_1 = 1.0$ unit and $\sigma_2 = 0.382$ unit, correlation length $L_2 = 8.0$ units. Simulation of wave scattering from this surface for wavelengths $\lambda = 32,\ 8,\ 2$ and 1 units are performed. The backscattering coefficients of the IEM, the first-order small perturbation model and the Kirchhoff model are plotted in Figs. 3.5.2(a) through 5.2(d) to compare with simulation. In Fig. 3.5.2(a), the incident wavelength is 32 units and the normalized surface parameters are $k\sigma_1 = 0.015$, $kL_1 = 0.196$, $k\sigma_2 = 0.075$ and $kL_2 = 1.57$. It is clear that for both scales the assumptions of the small perturbation model are satisfied. It is anticipated that the small perturbation model should be applicable. The excellent agreement among the simulation, the IEM and the small perturbation model indicates that at the low frequency end the IEM works well for a two-scale Gaussian surface. As expected the scattering from the large scale generates the major contribution. This can be demonstrated by plotting only the backscattering coefficient of the large scale in Fig. 3.5.2(a) using the first-order small perturbation model.

In Fig. 3.5.2(b), the incident wavelength is reduced to 8 units. At this wavelength, the surface parameters are $k\sigma_1 = 0.06$, $kL_1 = 0.78$, $k\sigma_2 = 0.3$, $kL_2 = 6.28$. As can be seen in Fig. 3.5.2(b), scattering is dominated by the large scale at smaller angles of incidence and by the small scale at large angles of incidence. This effect is clearly demonstrated by the backscattering coefficient curve for both the large and the small scales plotted separately in the figure. Note that the Kirchhoff solution is used for the large scale and the small perturbation model is used for the small scale. The agreement between simulation and the IEM is again observed. This agreement indicates that even with different roughness scales dominating at different angular ranges, the IEM is still applicable.

In Fig. 3.5.2(c), the incident wavelength is 2 units and the surface parameters at this wavelength are $k\sigma_1 = 0.24, kL_1 = 3.14, k\sigma_2 = 1.2, kL_2 = 25.12$. It is seen that the dominant scattering at smaller angles of incidence is still the large scale roughness and the dominant scattering at the large angle of incidence is the small scale roughness. The large scale satisfies the conditions of the Kirchhoff approximation [Ulaby *et al*, Chapter 12, 1982] and can be proven by calculating the backscattering coefficient using only the Kirchhoff model. However, the normalized parameters for the small scale do not satisfy either the conditions of the Kirchhoff model or those for the first-order small perturbation model [Ulaby *et al*, Chapter 12, 1982]. Thus, a standard two-scale model [Ulaby *et al*, Chapter 12, 1982] is not applicable. The IEM on the other hand is seen to agree well with the simulation regardless of the sizes of the small scale. In Fig. 3.5.2(d), the incident wavelength is reduced to 1 unit and the normalized surface parameters at this wavelength are $k\sigma_1 = 0.48$, $kL_1 = 6.28$, $k\sigma_2 = 2.40$, $kL_2 = 50.24$. At this wavelength, both the large and small scales satisfy the assumptions of the Kirchhoff model [Ulaby *et al*, Chapter 12, 1982]. Since the slope of the small scale is larger than that of the large scale, the angular trend is expected to be slower at large angles of incidence than at smaller angles of incidence. This phenomenon is clearly demonstrated in Fig. 3.5.2(d) by the backscattering coefficient calculated with the Kirchhoff model for both scales separately. By applying the IEM an excellent agreement between theory and simulation is demonstrated in Fig. 3.5.2(d). In view of all the cases in Fig. 3.5.2 it is clear that IEM is valid over the entire frequency range considered.

b. Generation of Rough Surfaces in Three-Dimensions with Specified Correlation Functions

To work the three-dimensional surface scattering problem, we need rough surfaces in three-dimensional space. A method to generate such a surface is discussed below.

It is a standard procedure to generate independent random deviates with various distributions [Press, 1987]. To correlate these independent random deviates according to a specified autocorrelation function can be achieved by the concept of digital filtering. Consider a two-dimensional digital filter with weights $w_{j,m}$ fed by independent random deviates $z_{j+k,m+l}$. The output of the filter $c_{k,l}$ can be written

as

$$c_{k,l} = \sum_j \sum_m w_{j,m} z_{j+k,m+1} \tag{5.10}$$

The autocorrelation function $\rho_{i,n}$ of a random process is defined as

$$\rho_{i,n} = E\{c_{k,l} c_{k+i,l+n}\} = \sum_j \sum_m \sum_p \sum_q w_{j,m} w_{p,q} \cdot E\{z_{j+k,m+l}\, z_{p+k+i,q+l+n}\} \tag{5.11}$$

Since the random deviates are mutually independent, ie.,

$$E z_{j+k,m+l} z_{p+k+i,q+l+n} = \begin{cases} 0, & j \neq p+i \text{ or } m \neq q+n \\ 1, & j = p+i \text{ or } m = q+n \end{cases} \tag{5.12}$$

it follows that the autocorrelation function can be simplified to

$$\rho_{i,n} = E\{c_{k,l} c_{k+i,l+n}\} = \sum_j \sum_m w_{j,m} w_{j-i,m-n} \tag{5.13}$$

By assuming symmetrical weighting, ie $w_{j-i,m-n} = w_{i-j,n-m}$, (5.13) can be rewritten as

$$\rho_{i,n} = \sum_j \sum_m w_{j,m} w_{i-j,n-m} \tag{5.14}$$

which suggests that the autocorrelation function $\rho_{i,n}$ is simply the two-dimensional convolution of the unknown weighting of the digital filter with itself. For a specified autocorrelation, the unknown weightings can be found as the inverse Fourier transform of the square root of the Fourier transform of the autocorrelation function $\rho(u,v)$, i.e.,

$$w_{j,m} = F^{-1}\left\{\sqrt{F[\rho(u,v)]}\right\} \tag{5.15}$$

where F^{-1} is the symbol for inverse Fourier transform.

For example, the weighting functions of Gaussian autocorrelation are given by

$$\rho_{i,n} = \exp\left[-\left(\frac{i}{l_1}\right)^2 - \left(\frac{n}{l_2}\right)^2\right] \tag{5.16}$$

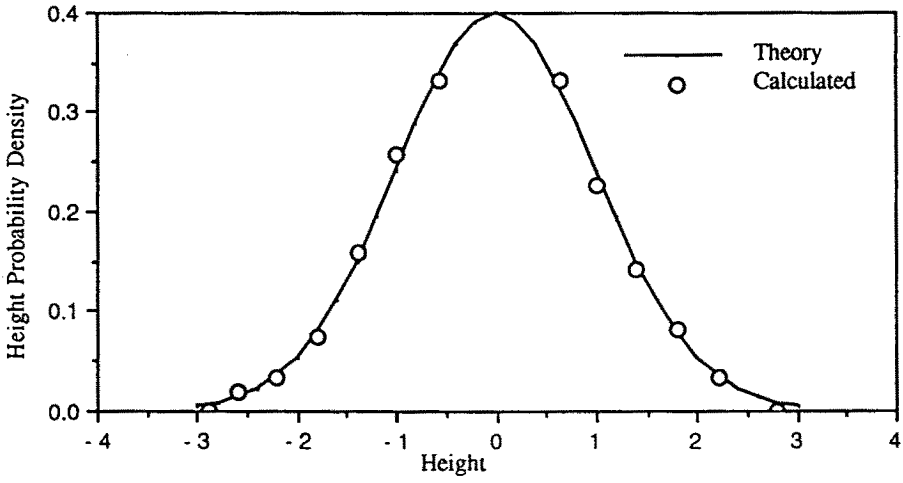

Figure 3.5.3 Comparison between theory and the numerically calculated surface height probability density function of a computer generated isotropic Gaussian surface.

The corresponding filter weights can be found analytically as

$$w_{j,m} = \frac{2}{\sqrt{\pi} l_1 l_2} \exp\left[-2\left(\frac{j}{l_1}\right)^2 - 2\left(\frac{m}{l_2}\right)^2\right] \tag{5.17}$$

To examine the validity of the algorithm, a random surface with isotropic Gaussian autocorrelation function is generated. The correlation length is chosen to be 0.75 unit which is arbitrarily divided into 6 discrete intervals. Since each point of the generated surface is the result of a weighted sum of independent random deviates, from the central limit theorem, the output surface should have a Gaussian height distribution. In Fig. 3.5.3, we have plotted the height density function calculated from the generated surface along with the theoretical curve. It is seen that the height density indeed agrees well with the theoretical Gaussian curve. To verify the correlating process, we have also calculated cuts of the autocorrelation function in various directions. In Figs. 3.5.4(a) through 3.5.4(c), the cuts of $\rho_{i,0}, \rho_{0,n}$, and $\rho_{i,i}$, ie., correlation in the horizontal (x-direction), vertical (y-direction) and diagonal (xy-direction) directions are plotted against their theoretical

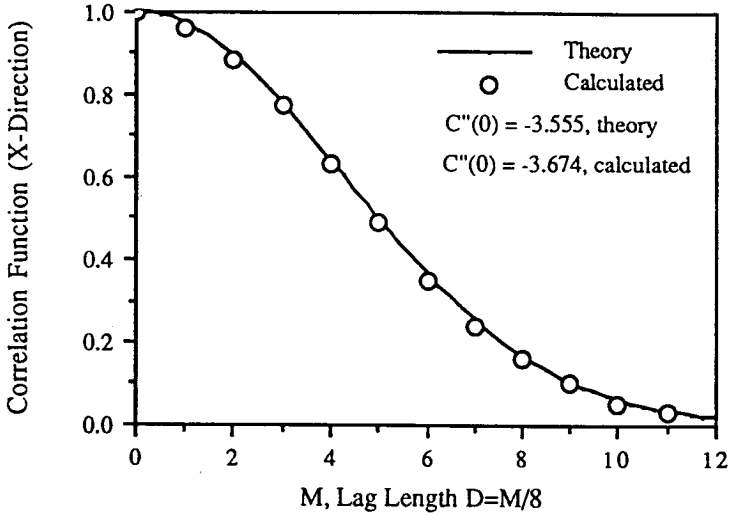

Figure 3.5.4(a) Comparison between theory and the numerically calculated correlation function (x-direction) of a computer generated isotro -pic Gaussian surface.

curves. Agreement between theory and the calculated correlation cuts is excellent in all three directions. For a Gaussian distributed surface, the slope distribution should also be Gaussian [Davenport and Root 1958]. The variance of the slope along any direction is equal to the negative of the product of the surface height variance σ^2 and the second derivative of the autocorrelation in that direction evaluated at the origin. For instance, the variance of the slope along the x-direction is

$$\sigma_{sx}^2 = -\sigma^2 \frac{d^2}{du^2} \rho(u.v = 0)\Big|_{u=0} \tag{5.18}$$

In Figs. 3.5.5(a) and 3.5.5(b), we have plotted the slope density calculated numerically from the generated surface along with the theoretical curves in x and y directions. Excellent agreement between theory and numerically calculated results can be seen. It is therefore concluded that the random surface generating algorithm presented here is a valid approach.

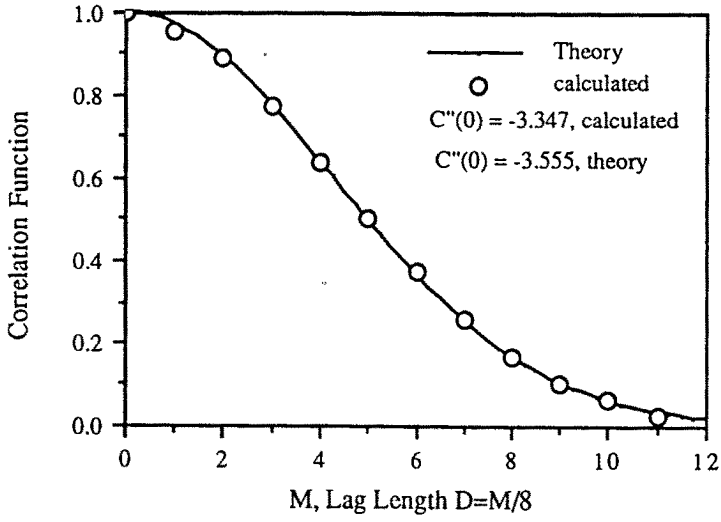

Figure 3.5.4(b) Comparison between theory and the numerically calculated correlation function (y-direction) of a computer generated isotropic Gaussian surface.

c. Simulation of Wave Scattering from Rough Surfaces in Three Dimensions

Based on the conclusion from the previous section we assume that the first iterative solution of the integral equation for the current density can be used to calculate an acceptable scattered field and subsequently the scattered power. In this section the procedure to obtain the simulated scattering coefficient from a computer generated random surface with this current estimate is presented in (*c.1*). The results illustrating polarization dependence are given in (*c.2*).

c.1 The simulation procedure

From Poggio and Miller [1973], the integral equation governing the induced surface current density from an impinging plane wave on a perfectly conducting random surface can be written as

$$\overline{J}(\overline{r}) = 2\hat{n} \times \overline{H}^{i} + \frac{1}{2\pi} \int \hat{n} \times [\nabla G \times \overline{J}(\overline{r}')]\, ds' \qquad (5.19)$$

The estimated current density is obtained by substituting $2\hat{n} \times \overline{H}^{i}$ into

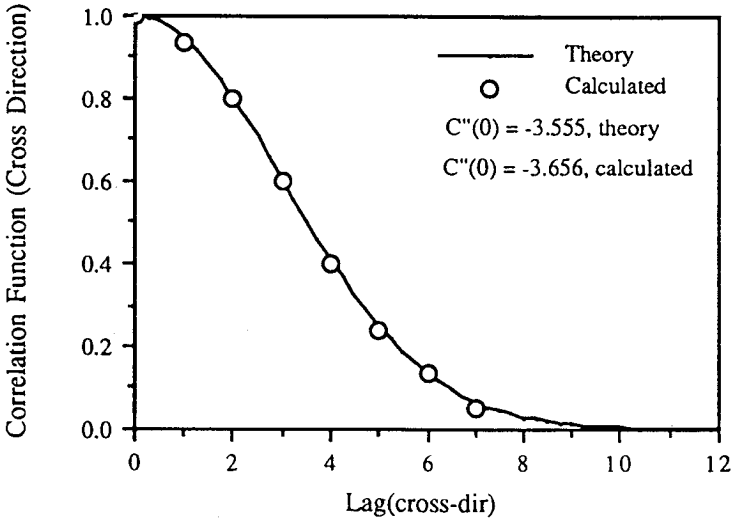

Figure 3.5.4(c) Comparison between theory and the numerically calculated correlation function (xy-direction) of a computer generated isotropic Gaussian surface.

the integral in (5.19) as

$$\overline{J}(\overline{r}) \cong 2\hat{n} \times \overline{H}^i + \frac{1}{2\pi} \int \hat{n} \times \left\{ \nabla G \times \left[2\hat{n}' \times \overline{H}^i(\overline{r}') \right] \right\} ds' \qquad (5.20)$$

For each surface patch generated on the computer, the integration in (5.20) can be performed numerically. With the current known, the far zone scattered field can be computed from the following integral

$$\overline{E}(\overline{r}) = -\eta \frac{jke^{-jkr}}{4\pi r} \hat{r} \times \hat{r} \times \int_{\text{Area}} \overline{J}(\overline{r}') e^{jk\hat{r}\cdot\overline{r}'} ds' \qquad (5.21)$$

The polarized scattering coefficient σ^0_{pq} is obtained by averaging over many scattered field samples as

$$\sigma^0_{pq} = \frac{4\pi r^2}{N A_{\text{eff}}} \left[\sum_{i=1}^{N} \left| \overline{E}^s_{pq} \right|^2_i - \frac{1}{N} \left| \sum_{i=1}^{N} \overline{E}^s_{pq} \right|^2 \right] \qquad (5.22)$$

where N is the number of surface samples taken in the calculation of scattered fields. $\overline{E}^s_{pq}$ is the scattered field for an incident "q" polarization and a scattered(or received) "p" polarization. According to

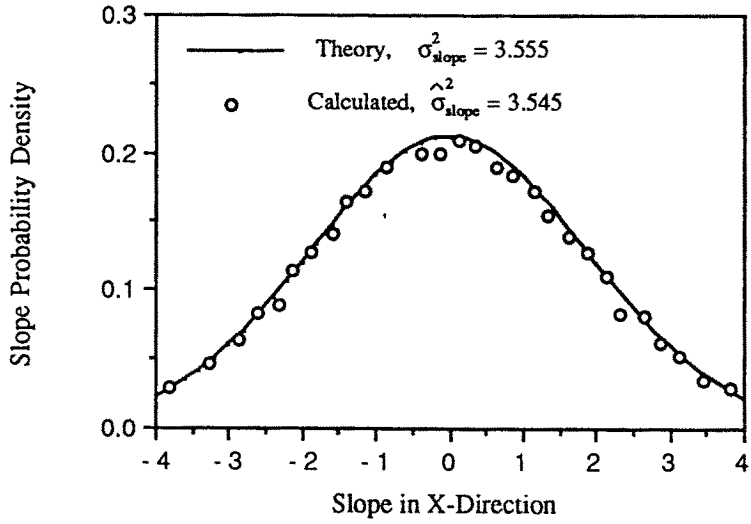

Figure 3.5.5(a) Comparison between theory and the numerically calculated slope probability density function (x-direction) of a computer generated isotropic Gaussian surface.

the standard spherical coordinates, the unit vectors representing these polarization states are

$\hat{h}_{inc} = \hat{y}$, incident horizontal polarization unit vector.

$\hat{v}_{inc} = \hat{h}_{inc} \times \hat{n}_i = -(\hat{x}\cos\theta + \hat{z}\sin\theta)$, incident vertical polarization unit vector.

$\hat{n}_i = \hat{x}\sin\theta + \hat{z}\cos\theta$, the incident direction unit vector.

Note that the angle θ is defined by $\cos\theta = -\hat{n}_i \cdot \hat{z}$ and the incident azimuth angle is assumed to be zero. The polarization unit vectors associated with the scattered field can be written as,

$\hat{h}_s = \hat{\phi} = -\hat{x}\sin\phi_s + \hat{y}\cos\phi_s$, scattered horizontal polarization unit vector.

$\hat{v}_s = \hat{\theta} = \hat{h}_s \times \hat{n}_s = \hat{x}\cos\theta_s\cos\phi_s + \hat{y}\cos\theta_s\sin\phi_s - \hat{z}\sin\theta_s$, scattered vertical polarization unit vector.

$\hat{n}_s = \hat{x}\sin\theta_s\cos\phi_s + \hat{y}\sin\theta_s\sin\phi_s + \hat{z}\cos\theta_s$, the scattered direction unit vector.

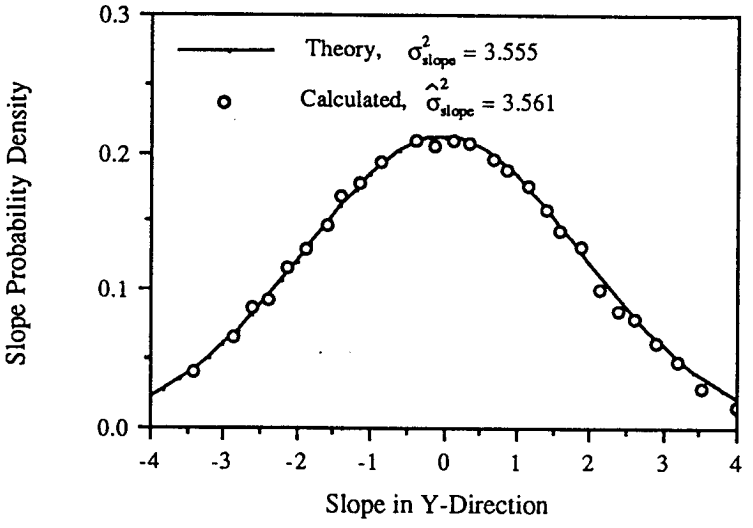

Figure 3.5.5(b) Comparison between theory and the numerically calculated slope probability density function (y-direction) of a computer generated isotropic Gaussian surface.

Note that the scattered angle θ_s is defined by $\cos\theta_s = \hat{n}_s \cdot \hat{z}$.

To insure the continuity of the field quantities at the edge of the illuminated area, the incident field is multiplied by a tapering function taken to be a Gaussian function, i.e.,

$$G(x - x_{cen}, y - y_{cen}) = \exp\left[-(x - x_{cen})^2 \cos^2\theta / g_x^2 - (y - y_{cen})^2 / g_y^2\right] \tag{5.23}$$

The constants g_x and g_y are there to control the rate of decrease of the tapering function. The effective illuminated area A_{eff} for this tapering function is defined to be

$$A_{\text{eff}} = \int_{-\infty}^{\infty}\int_{-\infty}^{\infty} G^2\, dx\, dy = \frac{\pi g_x g_y}{2\cos\theta} \tag{5.24}$$

c.2 Simulation results and discussion

Following the above simulation procedure and using the current from (2.1), the scattering behavior as a function of frequency for an

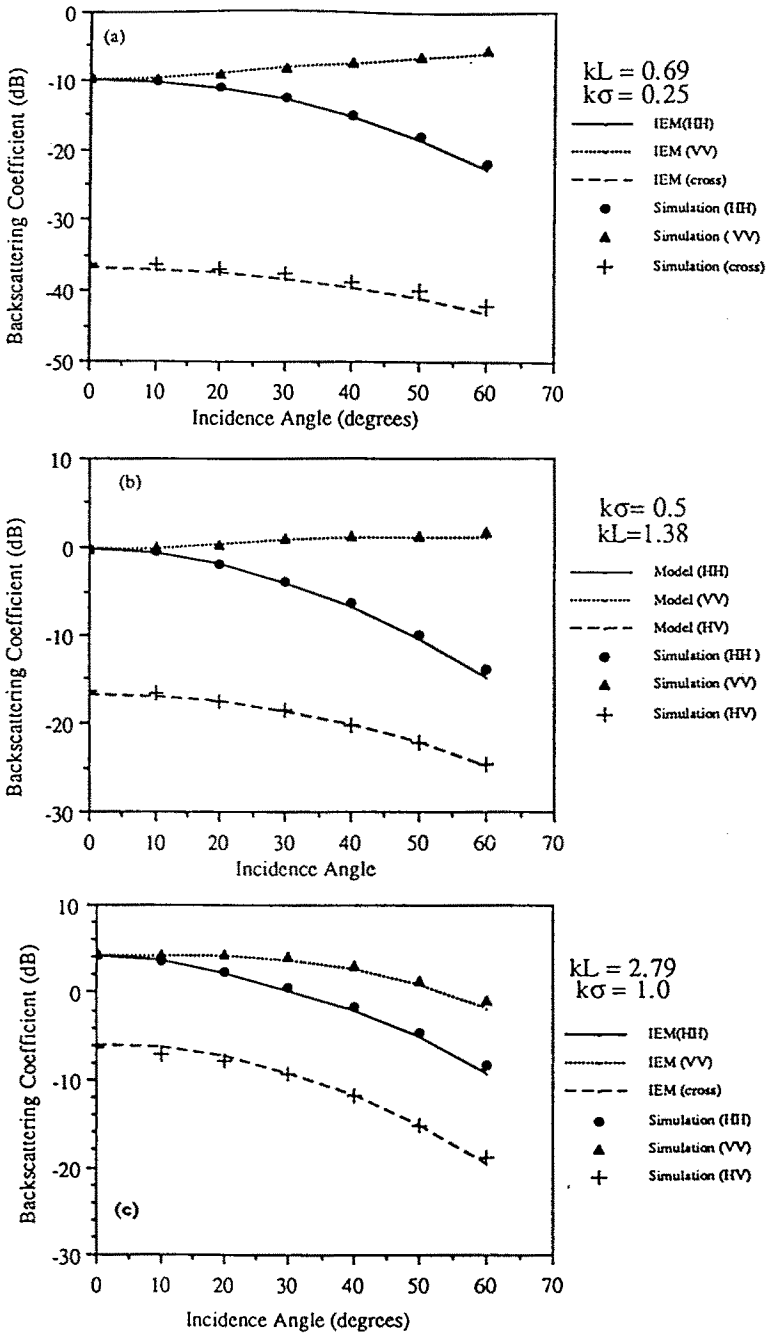

Figure 3.5.6 The simulated backscattering coefficient of an isotropic Gaussian correlated random surface with correlation length $L = 2$ units, surface height $\sigma = 0.716$ units. (a) $\lambda = 18$ units, (b)$\lambda = 9$ units, (c) $\lambda = 4.5$ units.

isotropic Gaussian surface is plotted in Figs. 3.5.6(a) through 3.5.6(c) for $\lambda = 18.0$, 9.0 and 4.5 units respectively. Note roughness parameters of the surface are $\sigma = 0.716$ unit and $L = 2.0$ units. In Fig. 3.5.6(a), it is seen that the returns between VV and HH polarizations have very pronounced level and angular trend difference that resemble the behavior of the first-order small perturbation model. This observation is not surprising since the normalized surface parameters are $k\sigma = 0.25$ and $k_L = 0.698$ unit which satisfy the validity conditions of the first-order small perturbation. Since three dimensional scattering simulation is performed, cross polarization return can also be obtained. It should be pointed out that the property of reciprocity, i.e. $\sigma^0_{vh} = \sigma^0_{hv}$, which is also shown in Fig. 3.5.6(a), is satisfied in the simulation procedure. Notice also the agreement between the simulation and the IEM model predictions which confirms the validity of the additional assumptions made in the simplification of the power calculation of the IEM model [Fung and Pan, 1987]. In Fig. 3.5.6(b), the incident wavelength is reduced to 9 units, the normalized roughness parameters are $k\sigma = 0.5$, k_L=1.38. These conditions do not satisfy the validity of the first order small perturbation model but they are not too far off either. The scattering behavior of the like polarized backscattering coefficient should not differ too much from that of Fig. 3.5.6(a), except for the higher level of return for both the like and the cross polarization returns. Note that good agreement between the IEM and the simulation is again observed in Fig. 3.5.6(b). In Fig. 3.5.6(c), the incident wavelength is further reduced to 4.5 units, the normalized roughness parameters are $k\sigma = 1.0$, $kL = 2.79$. At these values, the validity conditions of the first-order small perturbation is obviously violated, however, the condition of Kirchhoff approximation has not been reached yet. For this intermediate frequency, it is expected and clearly demonstrated in Fig. 3.5.6(c) that the difference between σ^0_{vv} and σ^0_{hh} diminishes and the level of scattering increasees relative to the two previous cases. Good agreement between the IEM and the simulation is again observed in Fig. 3.5.6(c). From the observations made in Figs. 3.5.6(a) through 5.6(c), it can be concluded that the effect of increasing frequency is to increase the level of scattering and to decrease the polarization difference between σ^0_{vv} and σ^0_{hh}. The effect of increasing frequency on the cross polarized return can also be concluded as (1) the angular trend of the cross polarization return becomes steeper as frequency increases, and (2) the level difference between the like and cross polarization

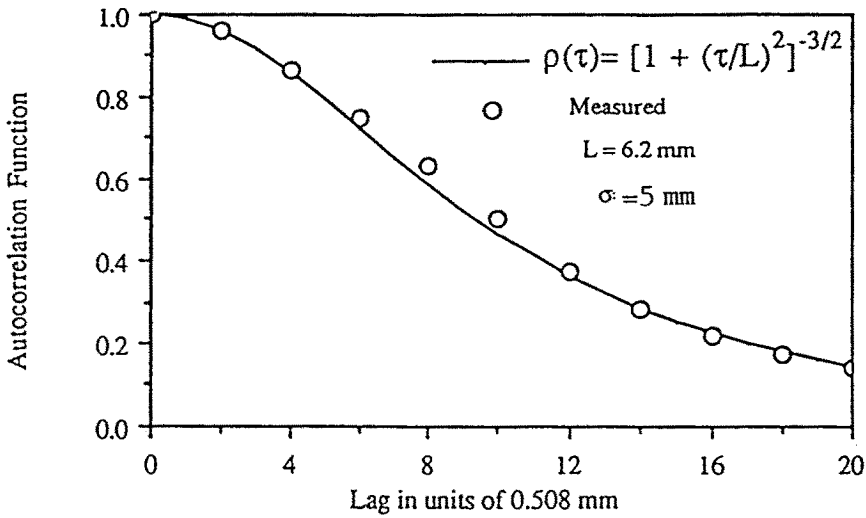

Figure 3.5.7 The autocorrelation function of the man-made slightly rough surface.

returns diminishes as frequency increases.

The autocorrelation function of a random surface is shown in Fig. 3.5.7. This surface has a kL of 3.25 and a $k\sigma$ of 0.44. Thus, the surface almost satisfies the first-order perturbation assumptions except that its $k\sigma$ and kL are a bit too large. The backscatter measurements taken at 25 GHz from this surface (Ulaby *et al* 1982) is shown in Fig. 3.5.8. It is seen that the first-order perturbation theory shows fairly good agreement with the vertically polarized measurements but progressively worse agreement with the horizontally polarized measurements as the incidence angle increases. On the other hand IEM shows good agreement with both polarizations.

3.6 Polarization Properties in Surface Imaging

a. Holographic Imaging Techniques

The conventional SAR creates an image of a target by processing time delay to, and relative doppler shift of, the scatterers comprising the target. Inverse synthetic aperture radar (ISAR) uses the SAR

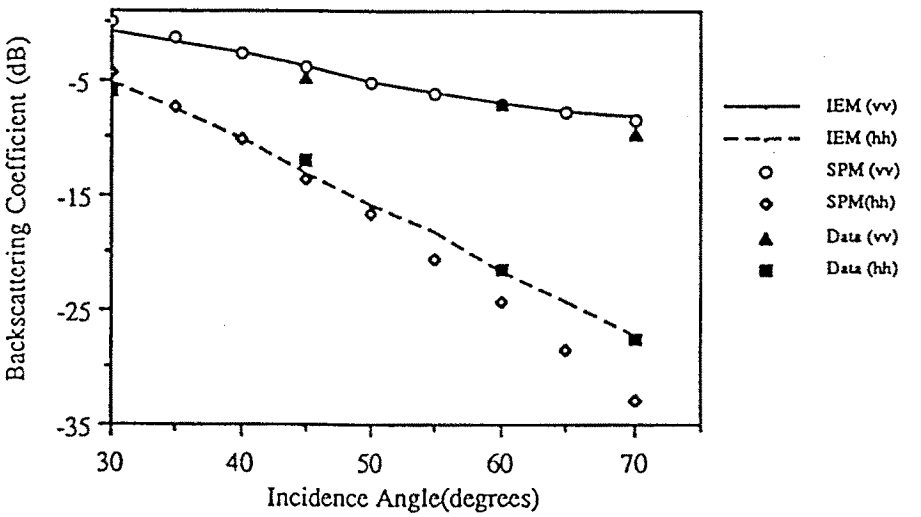

Figure 3.5.8 Comparison of measured data with the integral equation model (IEM) and the small perturbation model (SPM).

concept described above to synthesize a large aperture antenna. Conceptually we can think of the problem as one where we recover the locations of a number of scattering centers. We can develop the relation between the scattered field and the location of the scattering centers in the following fashion. The geometry for a three-dimensional measurement system is shown in Fig. 3.6.1. Assume a continuous-wave source of illumination. If the reflectivity at a particular object point, $p(r,\psi,\gamma)$, is denoted by $g'(r,\psi,\gamma)$, then the voltage recovered by the receiver, $V(t)$, is given by

$$V(t) = \mathrm{Re}\left\{\exp(j\omega t)g'(x,y,x)\exp(2jk|\overline{R}_0 - \overline{r}|)\right\} \qquad (6.1)$$

where $\exp(j\omega t)$ is the sinusoidal time dependence, $\exp(2jk|\overline{R}_o - \overline{r}|)$ is the phase delay due to propagation to and from the target and k is the wavenumber given by

$$k = \frac{2\pi}{\lambda} \qquad (6.2)$$

For the far field approximation, the difference between the two vectors $\overline{R}_0$ and $\overline{r}$ can be written as

$$|\overline{R}_0 - \overline{r}| = R_0 - \frac{\overline{R}_0 \cdot \overline{r}}{R_0} \qquad (6.3)$$

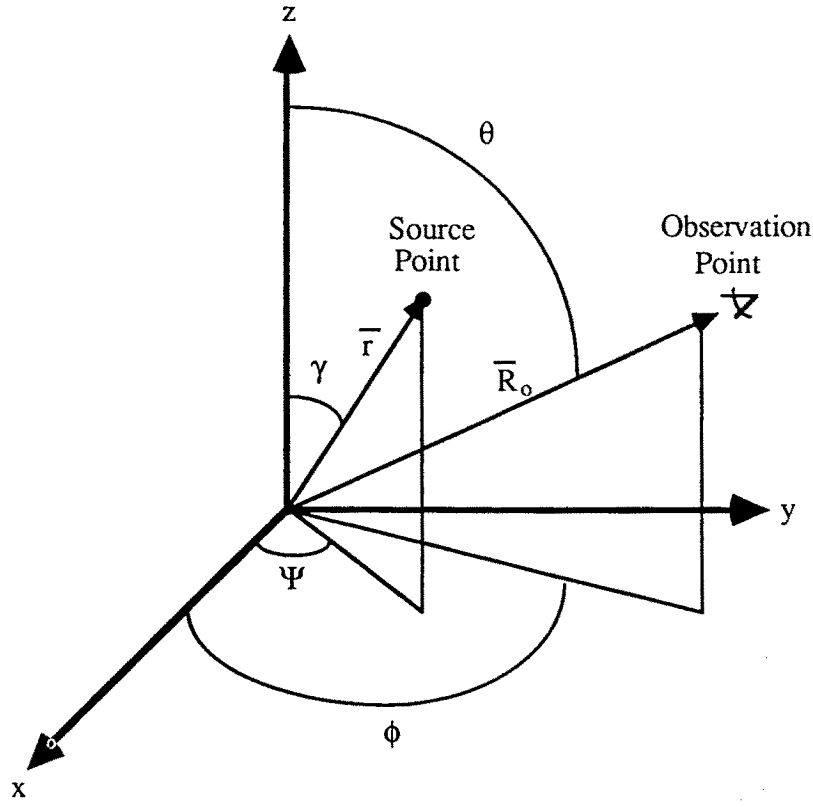

Figure 3.6.1 ISAR Measurement Geometry.

where

$$R_0 = |\overline{R}_0| \tag{6.4}$$

Also the dot product between $\overline{R}_0$ and $\overline{r}$ can be evaluated as

$$\frac{\overline{R}_0 \cdot \overline{r}}{R_0} = r\left[\sin\theta \sin\gamma(\cos\phi\cos\psi + \sin\phi\sin\psi) + \cos\theta\cos\gamma\right] \tag{6.5a}$$

$$= r[\sin\theta\sin\gamma\cos(\phi - \psi) + \cos\theta\cos\gamma] \tag{6.5b}$$

The received voltage can now be rewritten as

$$V(t) = \mathrm{Re}\{g'(x,y,z)\exp[j\omega t + 2jkR_0 - 2jkr(\sin\theta\sin\gamma\cos(\phi - \psi) + \cos\theta\cos\gamma)]\} \tag{6.6}$$

The first term in the exponential represents the sinusoidal time dependence of the received voltage and the last terms are a combination

of the phase delay due to propagation of the incident and reflected waves. Assuming that the receiver and the transmitter do not change range, the expression can be phase normalized to the $\exp(j\omega t)$ and $\exp(2jkR_o)$, so the received voltage can be reduced to

$$G(k,\phi,\theta) = g'(x,y,z)\exp[-2jkr(\sin\theta\sin\gamma\cos(\phi-\psi)+\cos\theta\cos\gamma)] \tag{6.7}$$

where $G(k,f,\theta)$ is the portion of the received signal to be processed. This reduction in the received signal can be accomplished with a calibration measurement from a known reference target such as a sphere. The variable k in equation (6.6) can be replaced by the spatial frequency f, where f is defined as

$$f = 2/\lambda \tag{6.8}$$

Then, the reduced received signal can be rewritten as

$$G(f,\phi,\theta) = g'(x,y,z)\exp[-2j\pi fr(\sin\theta\sin\gamma\cos(\phi-\psi)+\cos\theta\cos\gamma)] \tag{6.9}$$

To show the Fourier relation between the reduced received voltage $G(f,\phi,\theta)$ and the reflectivity function $g'(x,y,z)$, equation (6.9) should be transformed from spherical coordinates to cartesian coordinates. This transformation requires the following variable transformations

$$f_x = f\sin\theta\cos\phi \tag{6.10a}$$

$$f_y = f\sin\theta\sin\phi \tag{6.10b}$$

$$f_z = f\cos\theta \tag{6.10c}$$

and

$$x = r\sin\gamma\cos\psi \tag{6.11a}$$

$$y = r\sin\gamma\sin\psi \tag{6.11b}$$

$$z = r\cos\gamma \tag{6.11c}$$

Thus, for a single target point, the received signal has the form

$$G(f_x,f_y,f_z) = g'(x,y,z)\exp[-2\pi j(f_xx+f_yy+f_zz)] \tag{6.12}$$

Now if it is assumed that the target is made up of a three-dimensional distribution of discrete scatterers, and by use of the principle of superposition, the received signal can be written as

$$G(f_x,f_y,f_z) = \sum_{i=1}^{H}\sum_{j=1}^{M}\sum_{l=1}^{N} g(x_i,y_j,z_l) \cdot \exp[-2\pi j(f_xx_i+f_yy_j+f_zz_l)]\Delta x_i\Delta y_j\Delta z_l \tag{6.13}$$

where $g(x,y,z)$ is the object reflectivity density function, where g' is related to g by the following

$$g'(x,y,z) = g(x,y,z)\Delta x\Delta y\Delta z \tag{6.14}$$

H, M, and N are the total number of object points at respectively x, y and z directions. As $\Delta x_i, \Delta y_j$ and Δz_l approach zero, or in physical sense, as the distance between object points becomes infinitesimal, the reflectivity density function $g(x,y,z)$, becomes continuous. As a result, summations in equation (6.13) can be changed to an integration over the object volume

$$G(f_x,f_y,f_z) = \iiint_V g(x,y,x)\exp[-2\pi j(f_x x + f_y y + f_z z)]\,dx\,dy\,dz \tag{6.15}$$

$g(x,y,z)$ has a value in the object volume, and it is zero everywhere else, so the limits of integration can be extended to infinity

$$G(f_x,f_y,f_z) = \iiint_{-\infty}^{\infty} g(x,y,z)\exp[-2\pi j(f_x x + f_y y + f_z z)]dx\,dy\,dz \tag{6.16}$$

Equation (6.16) has the form of a Fourier transform. Since $G(f_x,f_y,f_z)$ is recovered directly from the measurement, the object reflectivity function can be determined from the inverse Fourier transform as

$$g(x,y,z) = \iiint_{-\infty}^{\infty} H(\bar{f})G(\bar{f})\exp[2\pi j(f_x x + f_y y + f_z z)]\,df_x\,df_y\,df_z \tag{6.17}$$

where $H(f_x,f_y,f_z)$ is the window function which identifies the amount of Fourier space recovered in the measured data. $H(f_x,f_y,f_z)$ has a value of unity if the point in question is within the aperture of spectrum and zero otherwise. The multiplication of $G(f_x,f_y,f_z)$ by $H(f_x,f_y,f_z)$ allows the preservation of the infinite limits on the integral for a bandlimited object. A plot of $g(x,y,z)$, gives the reflectivity of the object.

b. Resolution in ISAR Images

The resolution of the final image depends on the sampled extent of the Fourier space data. Ideally the spatial frequency vector, F, should be varied over all possible values of the Fourier space. This is obviously an impossible task, so the image is inherently a low pass filtered version

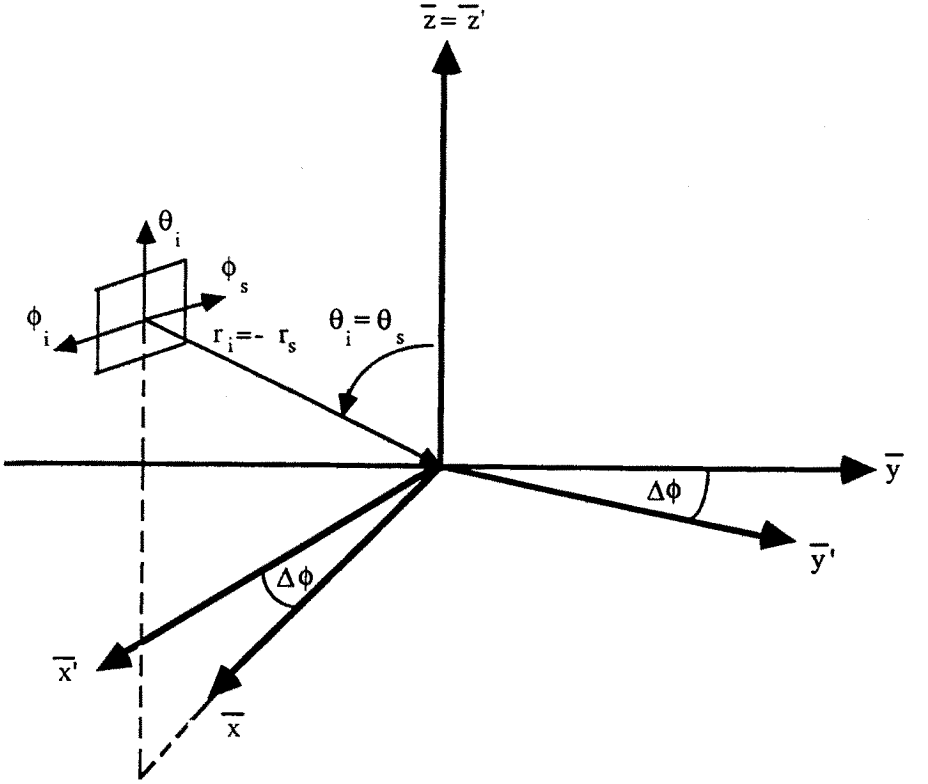

Figure 3.6.2 Monostatic Measurement Geometry.

of the object reflectivity. The relation between the size of the resolution cell and F is shown in equation (6.18).

$$\Delta x = \frac{2\pi}{F_{x\max} - F_{x\min}} \tag{6.18a}$$

$$\Delta y = \frac{2\pi}{F_{y\max} - F_{y\min}} \tag{6.18b}$$

$$\Delta z = \frac{2\pi}{F_{z\max} - F_{z\min}} \tag{6.18c}$$

where F_x, F_y, and F_z can be calculated from the geometry of Fig. 3.6.1.

$$\overline{F} = k(\hat{r}_t + \hat{r}_r) = \frac{2\pi}{\lambda}(\hat{r}_t + \hat{r}_r) \tag{6.19a}$$

$$F_x = \frac{2\pi}{\lambda}(\sin\theta\cos\phi + \sin\gamma\cos\psi) \tag{6.19b}$$

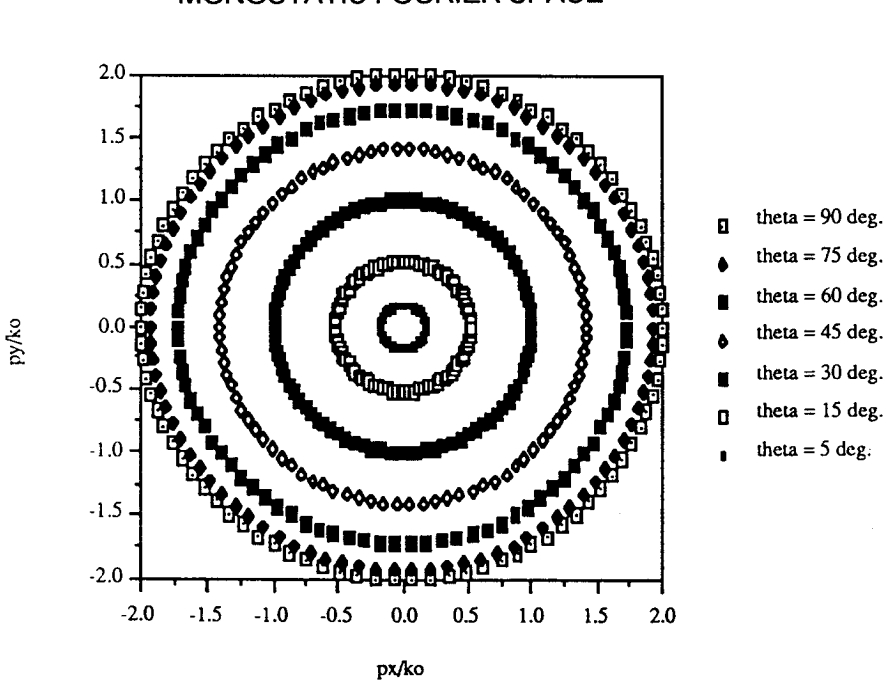

Figure 3.6.3(a) Monostatic Fourier space with object rotation.

$$F_y = \frac{2\pi}{\lambda}(\sin\theta\sin\phi + \sin\gamma\sin\psi) \tag{6.19c}$$

$$F_z = \frac{2\pi}{\lambda}(\cos\theta + \cos\gamma) \tag{6.19d}$$

Variation in value of F can be achieved by varying the position of the receiver, transmitter or the object; or by varying the illumination frequency. From a measurement perspective, variation of the illumination frequency is a more practical way to sample a large area of the spectral domain. For conducting objects, frequency diversity has been shown experimentally to improve the final image of the target over the single frequency image (Langenburg, *et al.*, 1983). The Fourier variable given in equation (6.8) is an equation for a sphere of radius $2k$, known as the Ewald sphere (Devaney, 1983). Because the information is band limited by this sphere, the resultant image corresponds to a low pass version of the actual image data. Four possible measurement schemes can be used to measure the scattered field at wavenumbers

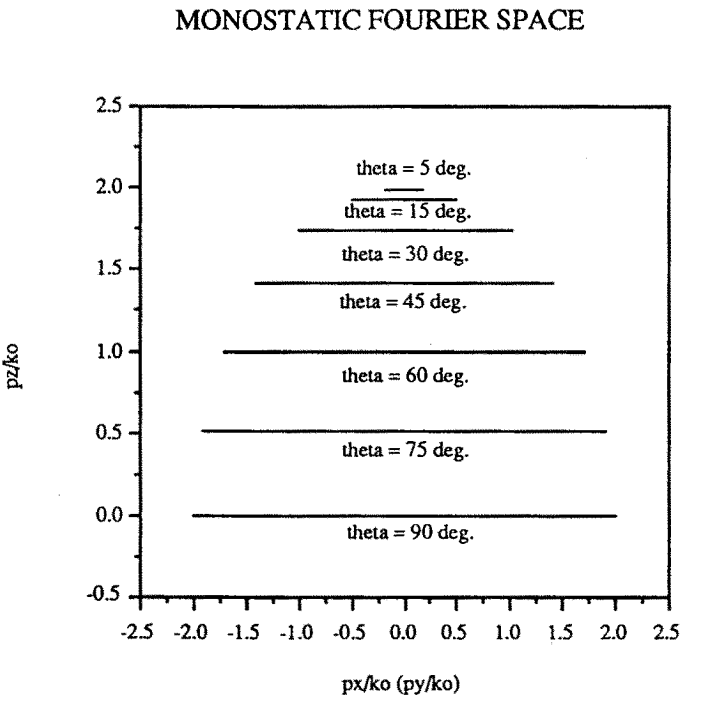

Figure 3.6.3(b) Location of the f_x and f_y planes.

residing within this sphere. These include monostatic with object rotation, bistatic with object rotation, bistatic with receiver rotation, and bistatic multiple experiments where the illumination direction is changed. Each of these measurement schemes fills the requisite Fourier space in a different fashion. Referring to the measurement geometry of Fig. 3.6.2, monostatic measurements fill the Ewald sphere as shown in Figs. 3.6.3(a) and 6.3(b). The $k_x - k_y$ planes in Fig. 3.6.3a are parallel to the plane of rotation of the object. Varying the incident angle, θ, varies the value of k_z at which the $k_x - k_y$ plane cuts the Ewald sphere. A similar situation occurs for measurements taken in the bistatic configuration with object rotation. The portion of the Ewald sphere filled using this measurement scheme is shown in Figs. 3.6.4(a) and 3.6.4(b). The specific case depicted in Fig. 3.6.4 has the transmitter and receiver placed forty-five degrees apart in azimuth and at equal elevation angles. In both of these cases the quantity of the Fourier space selected is the surface of a cone, in effect a two dimensional surface. This re-

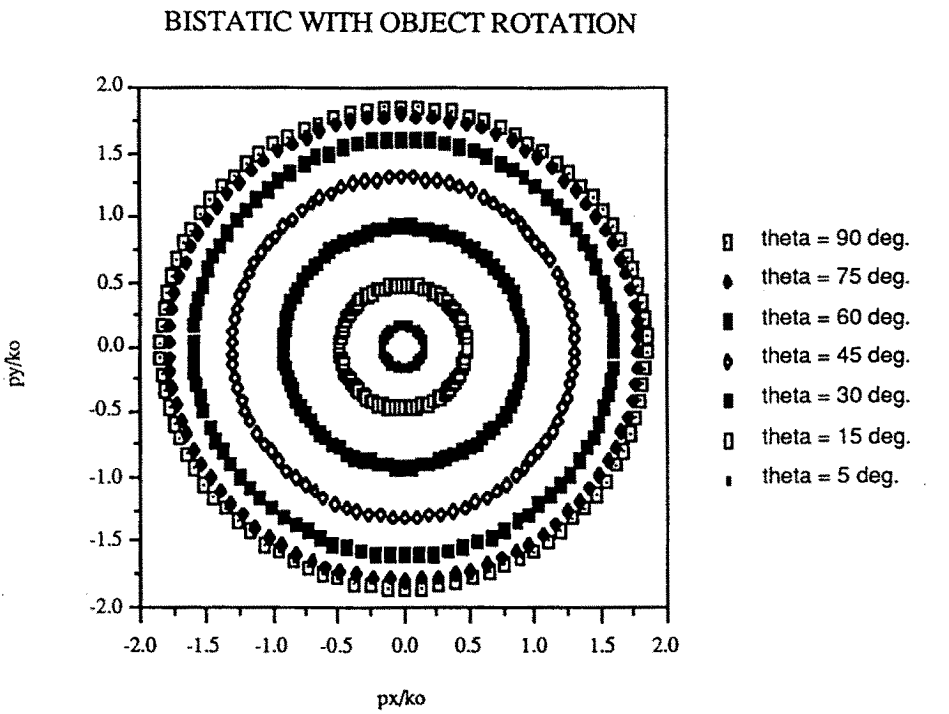

Figure 3.6.4(a) Bistatic Fourier space ($\alpha = 45°$) with object rotation.

stricts the image to a projection of a three dimensional object to a two dimensional plane.

If the receiver is rotated instead of the object, the Fourier-space plot depicted in Fig. 3.6.5 is obtained. For the case shown, the transmitter is fixed at ($\theta = 45°, \phi = 0°$) and the receiver is fixed in elevation at forty five degrees and rotated in azimuth from zero to three hundred and sixty degrees. The case is significant. In the previous two examples, to access the two dimensional Fourier space requires the use of frequency diversity and object rotation. In this case, the same two dimensional Fourier space can be recovered at a single frequency and no object rotation. The difference in the images recreated by the information recovered from these two scans is significant. We can interpret them in the following manner.

Given the measurement geometry shown in Fig. 3.6.6, the receiver samples the scattered field from all aspect angles (azimuth angle information). With this information and the Fourier relation between the

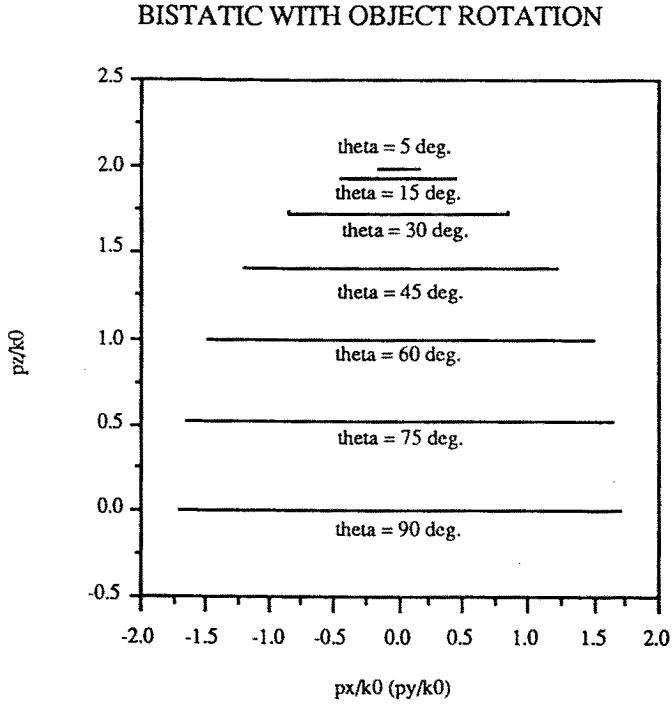

Figure 3.6.4(b) Location of the f_x and f_y planes.

far field recovered data and equivalent sources in the aperture of illumination, the equivalent scattered field sources at the target surface can be recovered. The location of the scattering intensities is derived from one illumination geometry. Consequently, these can be interpreted as equivalent field sources and used to predict what the measured field quantities will be in the far field (since they are derived from original far field measured data and assuming that sufficient sampling was employed to prevent aliasing in the image plane). This is in sharp contrast to the manner in which convention SAR and ISAR systems collect data. Recall that in the previous example the transmitter and the target remain stationary and the receiver scans in azimuth (potentially the receiver could scan in both azimuth and elevation to create complete three dimensional holographic data). In a conventional SAR or ISAR system (see Fig. 3.6.7), the transmitter and receiver remain fixed relative to each other, and move with respect to the target (In ISAR this is usually a circular scan and in SAR a linear scan, although

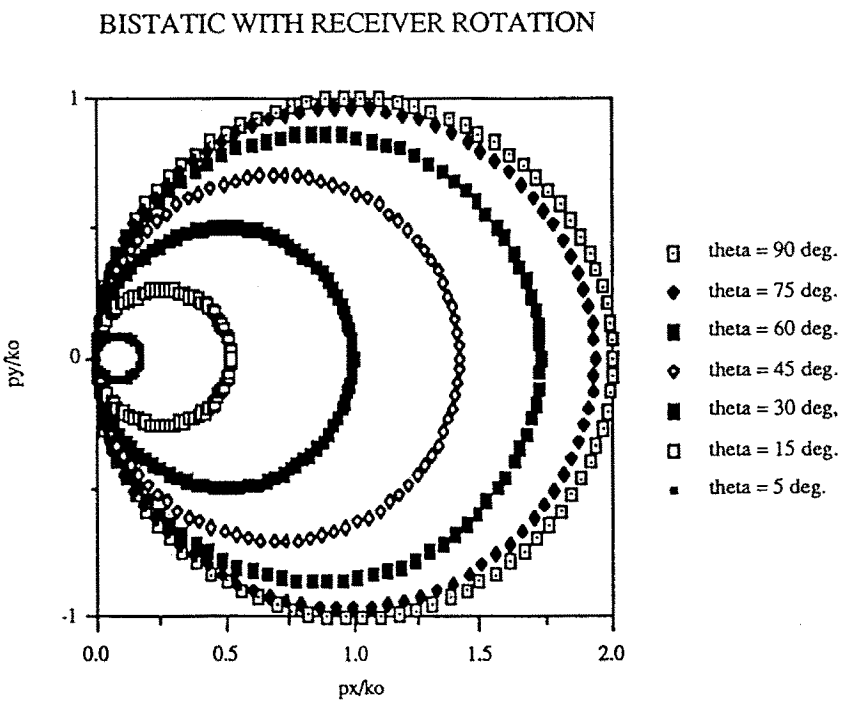

Figure 3.6.5(a) Bistatic Fourier space with receiver rotation.

other scan configurations can exist). We cannot interpret the resultant image as a display of equivalent sources because the illumination direction changes with respect to the target orientation. This image must be interpreted as a display of the radar cross section of an equivalent omni-directional scatterer in each resolution cell. This is the reflectivity map of the target. One may interpret these techniques (SAR and ISAR) as a synthesization of a large aperture antenna with very fine beamwidth.

There are two significant differences between conventional SAR and ISAR implementations. Generally, the SAR implementation uses relatively small focused angular (synthesized) apertures and a small transmitter bandwidth (usually less than 20 MHz). The ISAR configuration is capable of employing large focused apertures (360 degrees if desired) and extremely wide bandwidth (in some cases greater than 20 GHz). The reproduced image from the SAR can be considered a co-

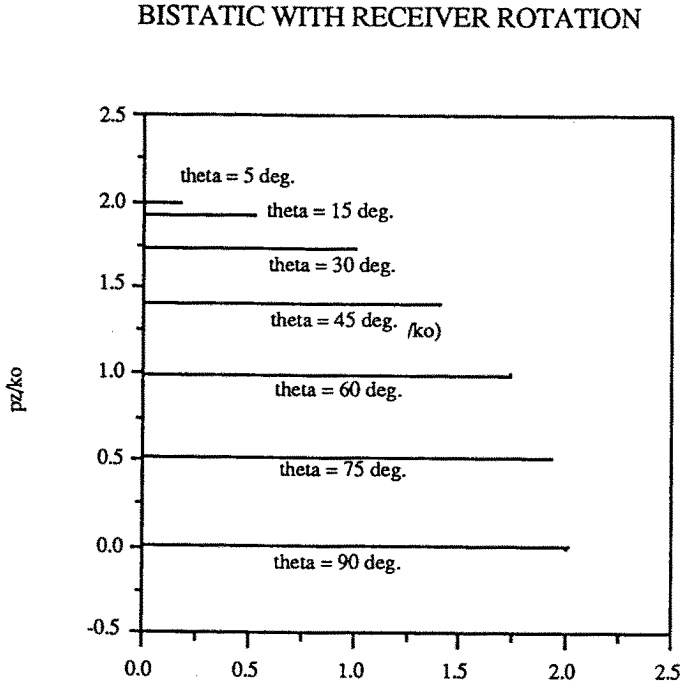

Figure 3.6.5(b) Location of the f_x and f_y planes.

herent average of narrow aspect angle and frequency information. The ISAR however, can produce an image that is a coherent average of wide aspect angle and wide bandwidth target scattering characteristics.

From a measurement perspective, variation of the illumination wavelength is an inexpensive way to obtain measurements for a larger amount of wavenumbers by varying the radius of the Ewald sphere. However, for dielectric scatterers, the parameter used for imaging can vary with frequency. Single frequency images have been formed for dielectric materials (Langenburg, *et al.*, 1983), but the use of frequency diversity for imaging dielectric scatterers has not been investigated experimentally. The use of small bandwidths may still improve images of dielectric scatterers. For targets which can be considered perfectly conducting, frequency diversity has been shown experimentally to improve images of conducting targets over single frequency images (Farhat, *et al.*, 1984; Blanchard and Dolaty, 1988). Frequency diversity has similar

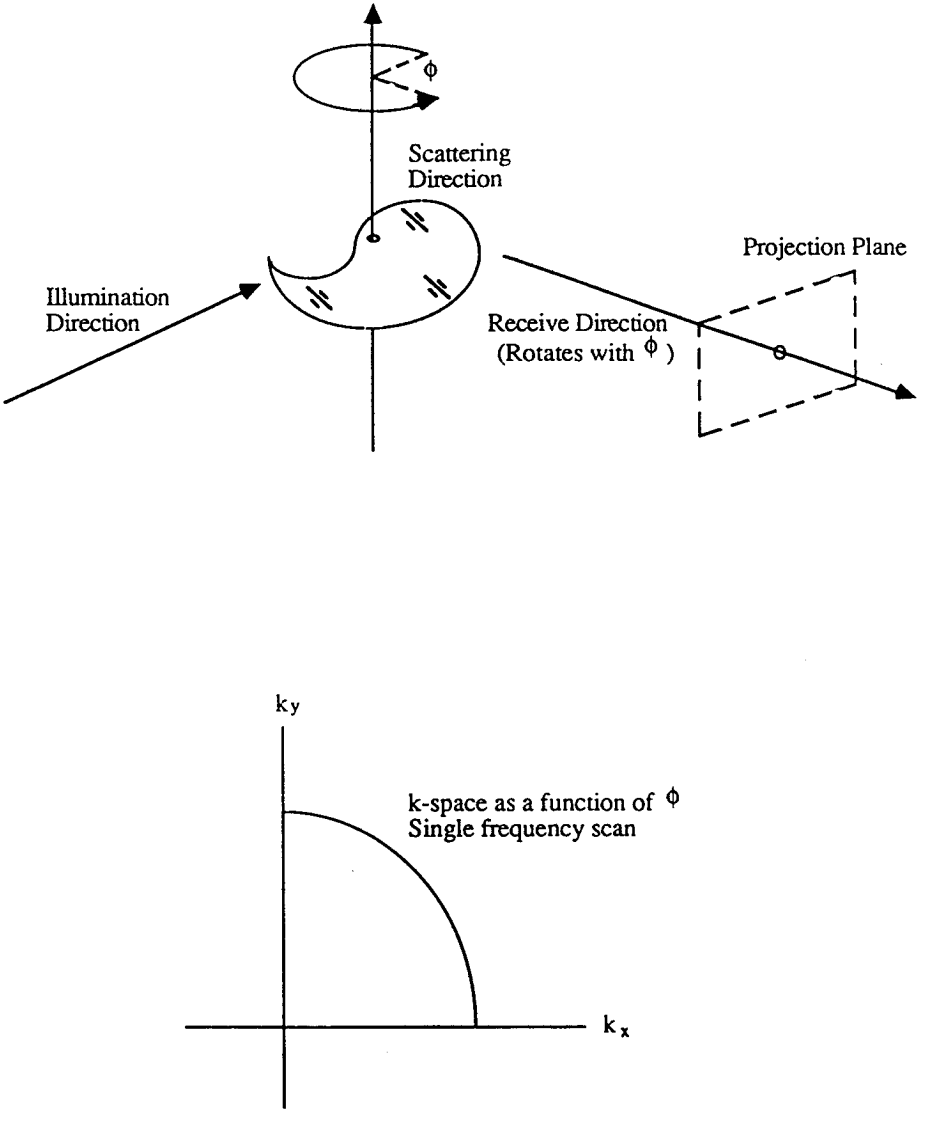

Figure 3.6.6 Scan configuration where the receiver moves relative to the target and transmitter location.

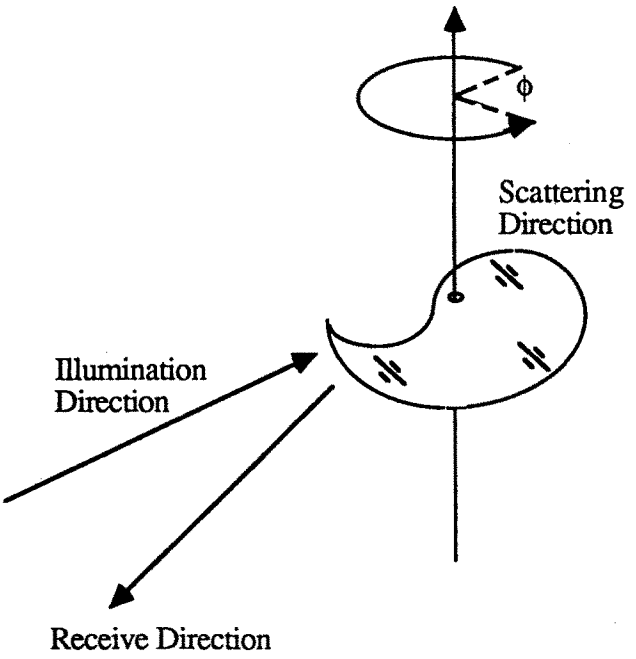

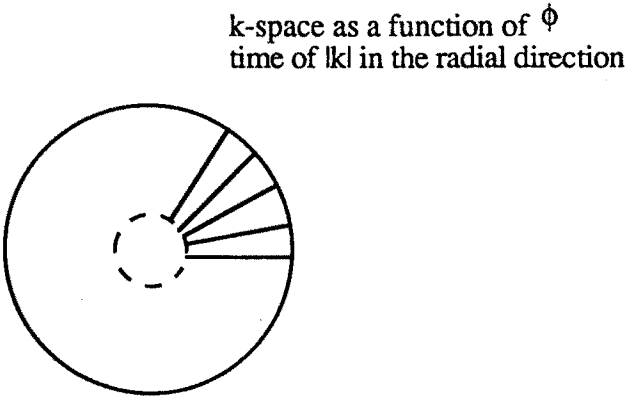

Figure 3.6.7 Scan configuration for the conventional SAR and ISAR (transmitter and receiver remain fixed relative to each other).

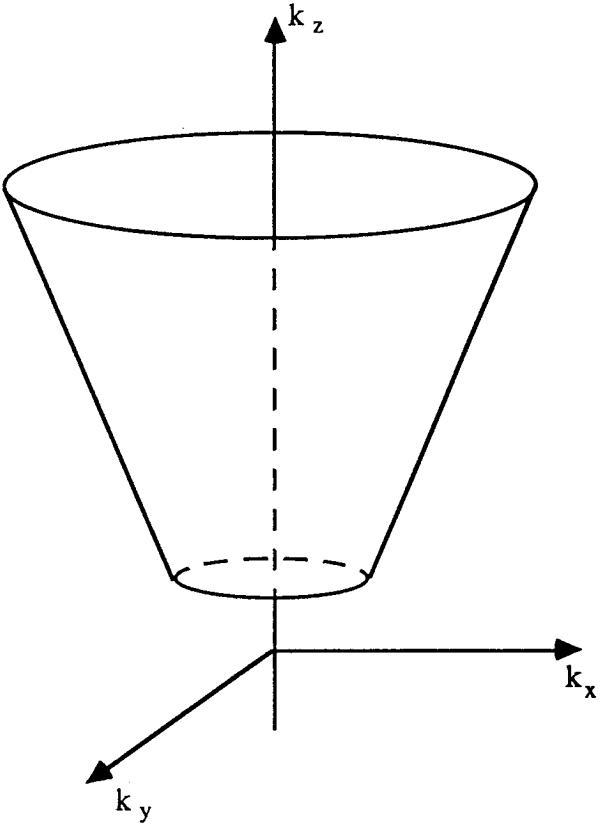

Figure 3.6.8 Manifold created in "k" space when object rotation at a single incident angle is incorporated.

effects on both monostatic and bistatic experiments.

c. Projection Images

After obtaining the object function from a three dimensional inverse Fourier transform, it is necessary to have a four dimensional space to display the image: three dimensions for the position and one dimension for the magnitude of the object function. Since this is not generally possible, usually a projection of the reflectivity $g(x, y, z)$ is plotted. In this case, only a three dimensional space is required to plot an image with two dimensions for position and one dimension for the magnitude. The following section will discuss the mathematics involved

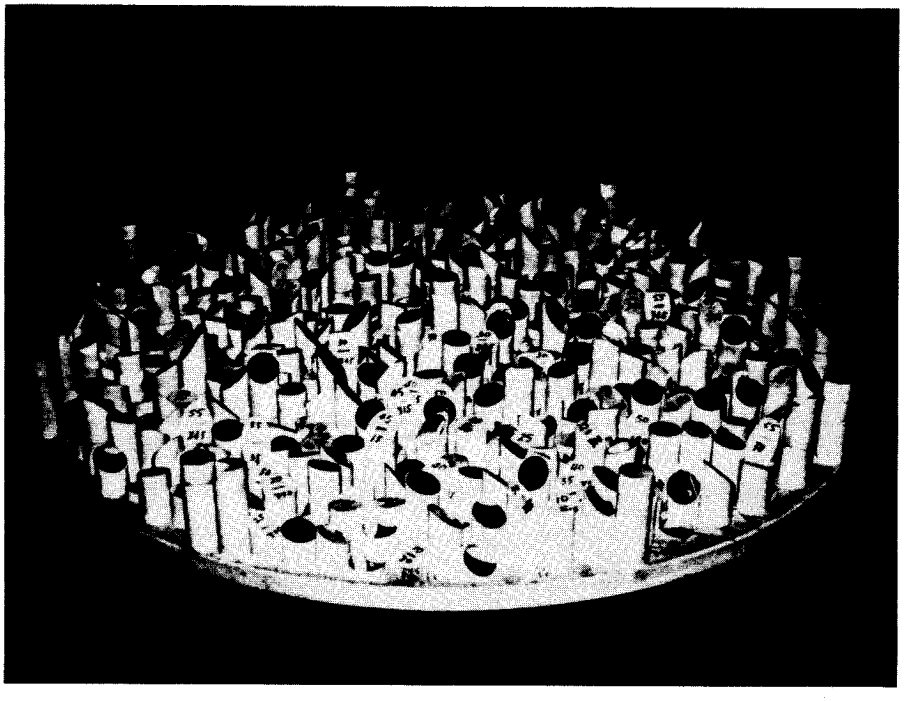

Figure 3.6.9 Photograph of the faceted surface.

in calculating $g_{proj}(x, y)$ from the scattered far field.

For convenience, the plane of projection is chosen to be the xy plane. The projection of $g(x, y, z)$ to xy plane is defined to be

$$g_{proj}(x, y) = \int_{-\infty}^{\infty} g(x, y, x) dz \tag{6.20}$$

Replacing the value of $g(x, y, z)$ by its Fourier transform pair gives

$$g_{proj}(x, y) = \iiint_{-\infty}^{\infty} H(\overline{f}) G(\overline{f}) \cdot \exp[2\pi j(f_x x + f_y y + f_z z)] \, df_x \, df_y \, df_z \, dz \tag{6.21}$$

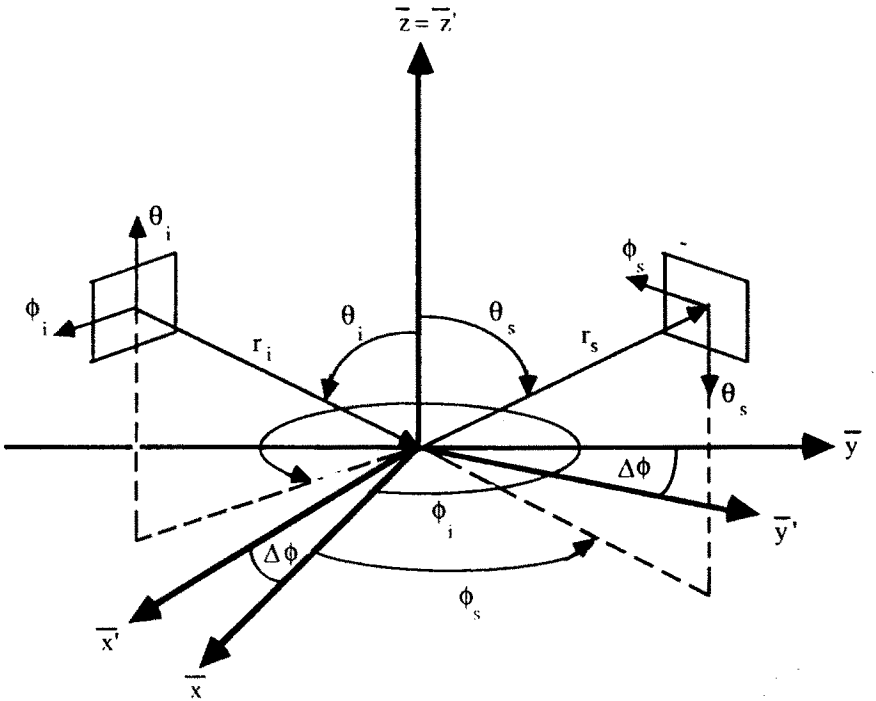

Figure 3.6.10 Measurement configuration for the imaging measurements.

The order of integration can be changed to give

$$g_{proj}(x,y) = \iiint_{-\infty}^{\infty} H(\bar{f})\, G(\bar{f}) \exp[2\pi j(f_x x + f_y y)] \cdot \left(\int_{-\infty}^{\infty} \exp[2\pi j f_z z] dz \right) df_x\, df_y\, df_z \tag{6.22}$$

The integration inside the parenthesis can be identified as a delta function

$$\int_{-\infty}^{\infty} \exp(2\pi j f_z z) dz = \delta(f_z) \tag{6.23}$$

By using the sifting property of the delta function, the integration over

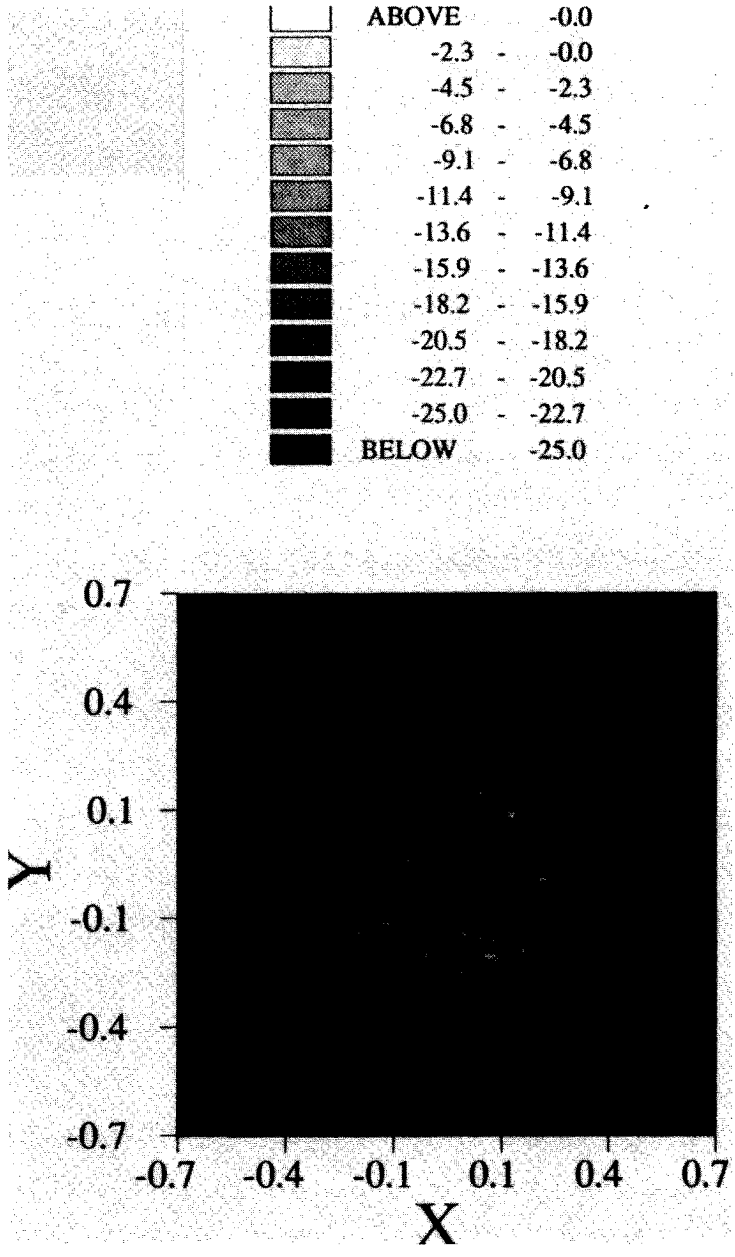

Figure 3.6.11 Scattering cross section for VV polarization–Faceted surface.

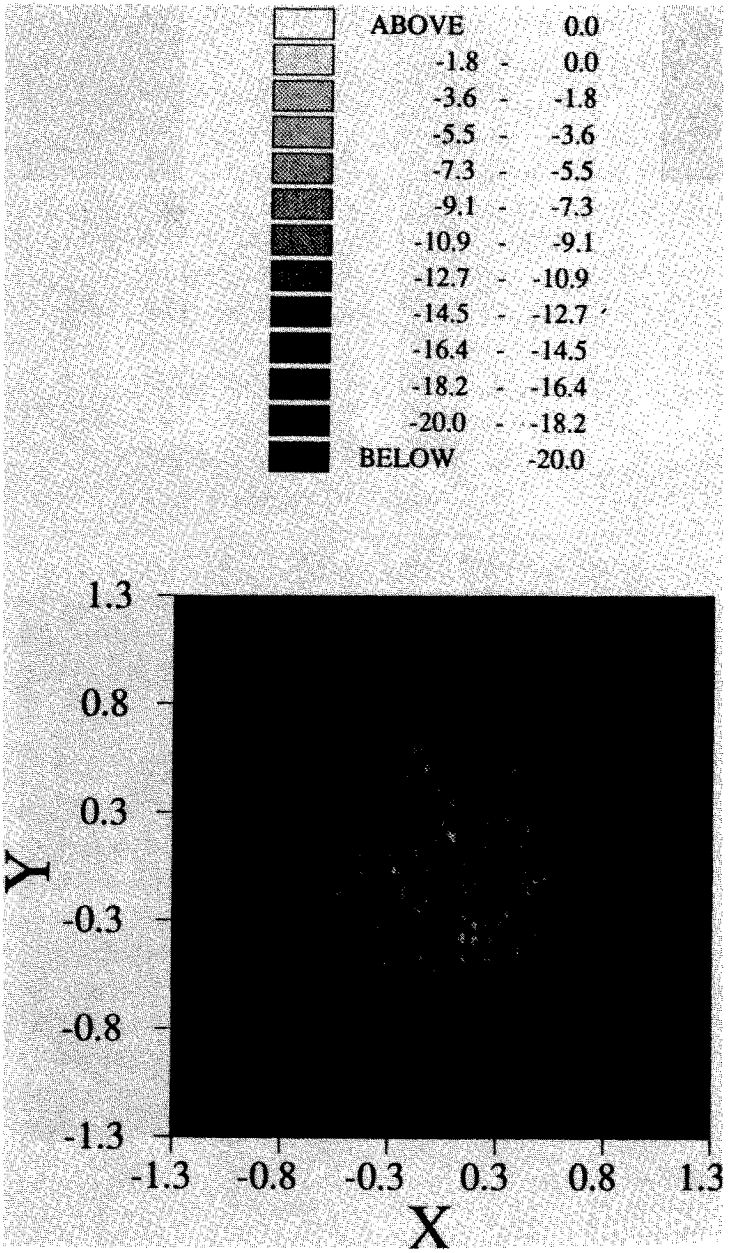

Figure 3.6.12 Scattering cross section for HH polarization–Faceted surface.

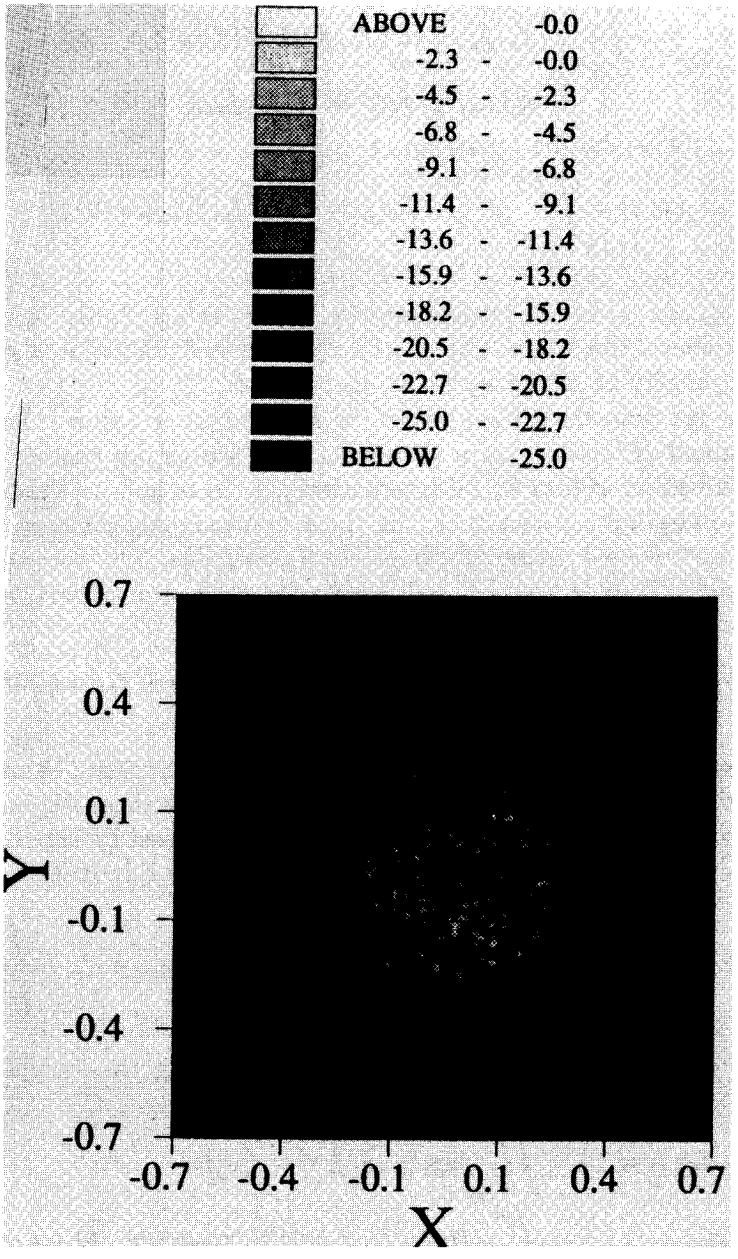

Figure 3.6.13 Scattering cross section for VH polarization–Faceted surface.

df_z can be evaluated as

$$\int_{-\infty}^{\infty} H(f_x, f_y, f_z)\, G(f_x, f_y, f_z)\delta(f_z) df_z = H(f_x, f_y, f_z = 0)\, G(f_x, f_y, f_z = 0) \tag{6.24}$$

Now $g_{proj}(x, y)$ can be rewritten as

$$g_{proj}(x, y) = \iint_{-\infty}^{\infty} H(f_x, f_y, f_z = 0)\, G(f_x, f_y, f_z = 0) \exp[2\pi j(f_x x + f_y y)]\, df_x\, df_y \tag{6.25}$$

where $g_{proj}(x, y)$ is the projection of $g(x, y, z)$ to xy plane. The information about the entire object is projected, but only the scatterers that physically lie in the xy plane are focused.

The previous theory has presented a technique to recover the three dimensional reflectivity of a distribution of scattering centers under the assumption of no mutual interaction processes and no shadowing. Using tomographic techniques, the three-dimensional scatterer can be reconstructed as a series of two-dimensional slices. The tomographic technique can be derived beginning with the three dimensional Fourier transform

$$g(x, y, z) = \iiint_{-\infty}^{\infty} H(\bar{f})\, G(\bar{f}) \exp[2\pi j(f_x x + f_y y + f_z z)]\, df_x df_y df_z \tag{6.26}$$

where again H is a window function representing the finite bandwidth in Fourier space of the measurements. A slice of the three-dimensional reflectivity function at a desired value of z is obtained by substituting that value of z into equation (6.26). For z equal to β, equation (6.26) becomes

$$g(x, y, z = \beta) = \iiint_{-\infty}^{\infty} H(\bar{f})\, G(\bar{f}) \cdot \exp[2\pi j(f_x x + f_y y + f_z \beta)]\, df_x\, df_y\, df_z \tag{6.27}$$

Changing the order of integration and separating the z-dependent terms in equation (6.27) yields

$$g(x, y, z = \beta) = \iint_{-\infty}^{\infty} \exp[j2\pi(f_x x + f_y y)] \cdot \int_{-\infty}^{\infty} H(f_z, f_y, f_z)\, G(f_x, f_y, f_z) \cdot \exp\left[j2\pi\sqrt{f^2 - f_x^2 - f_y^2}\,\beta\right] df_x\, df_y\, df_z \tag{6.28}$$

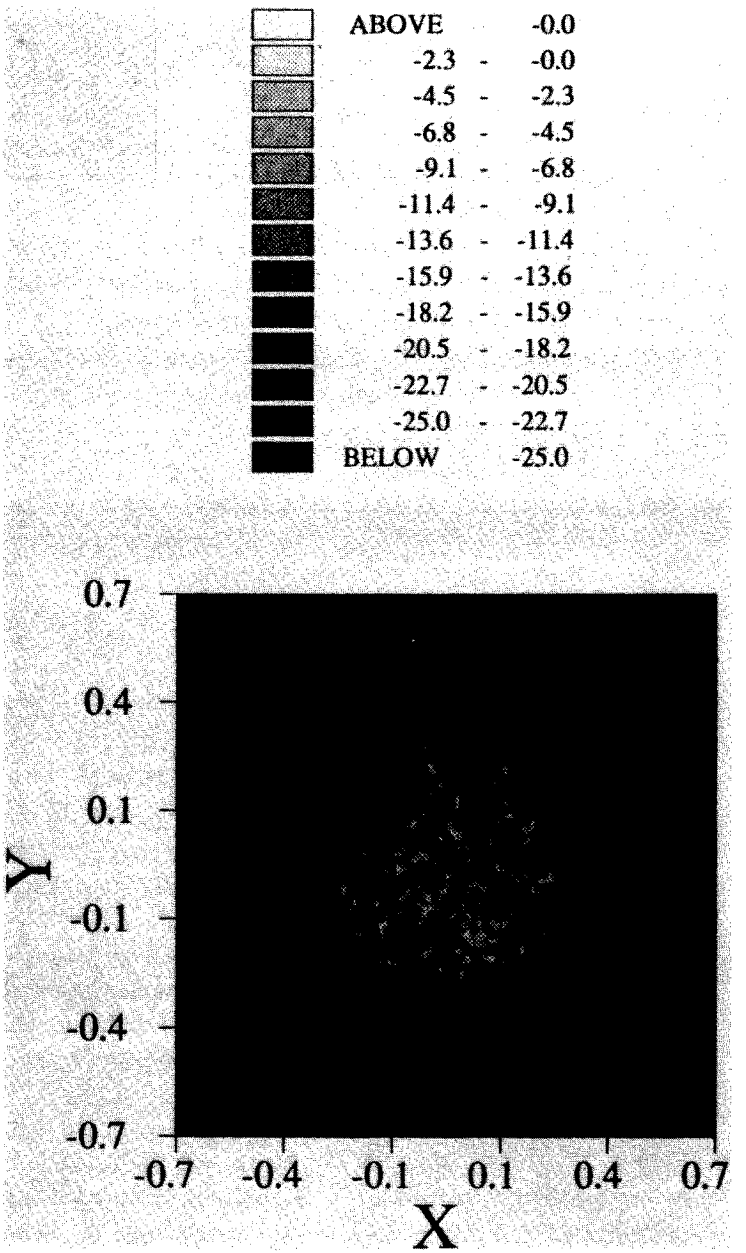

Figure 3.6.14 Shaded Contour map of Cross polarized scattered field reflectivity for the faceted surface (polarization reference for the transmitter and receiver antennas are defined by an ellipticity of -10° and tilt angle of 60°).

The inner integration is seen to be the projection of the measured data filtered by the exponential phase term dependent on b onto the f_x f_y-plane. Mathematically, this is

$$[H(f_x, f_y)\, G(f_x, f_y)]_{\beta,proj} = \int_{-\infty}^{\infty} H(f_x, f_y, f_z) \cdot G(f_x, f_y, f_z)\, \exp[j2\pi f_z \beta]\, df_z \tag{6.29}$$

For a three dimensional target, data acquisition over a finite bandwidth and finite object rotation angle results in a three dimensional contour in frequency space as shown in Fig. 3.6.8. As shown in the figure, for a given f_x and f_y, there is only a single value of f_z. The projection-slice theorem of equation (6.17) for this case is given by

$$[H(f_x, f_y)G(f_x, f_y)]_{\beta,proj} = \int_{-\infty}^{\infty} H(f_x, f_y, f_z)\delta(f_z - \sqrt{f^2 - f_x^2 - f_y^2}) \cdot G(f_x, f_y, f_z) \exp\{j2\pi f_z \beta\} df_z \tag{6.30}$$

which reduces to the form

$$[H(f_x, f_y)G(f_x, f_y)]_{\beta,proj} = H(f_x, f_y, f_z)G(f_x, f_y, f_z) \exp(j2\pi f_z \beta) \tag{6.31}$$

where $f_z = \sqrt{f^2 - f_x^2 - f_y^2}$. Projection of the measured data using equation (6.31) results in a focusing of the entire three dimensional image at the $z = \beta$ plane. In other words, the entire object is projected onto the plane but only the scatterers that physically lie in that plane are focused. Slices of the three-dimensional object are not possible in this case. The results of this processing are identical to processing the three-dimensional contour in frequency space as if it were the two dimensional annulus. To produce a three dimensional image using the projection slice theorem, data must be available over a finite bandwidth in the f_z coordinate.

The previous analysis indicates why a conventional SAR can not produce three dimensional images. The data acquired must be projected to a two dimensional plane. That can be accomplished by a projection image or by a filtered slice backprojection. In either case the three dimensional information is collapsed (coherently in the tomographic case and incoherently in the projection image) onto a two dimensional plane which causes confusion when the scattering information from two scattering points are placed on top of each other.

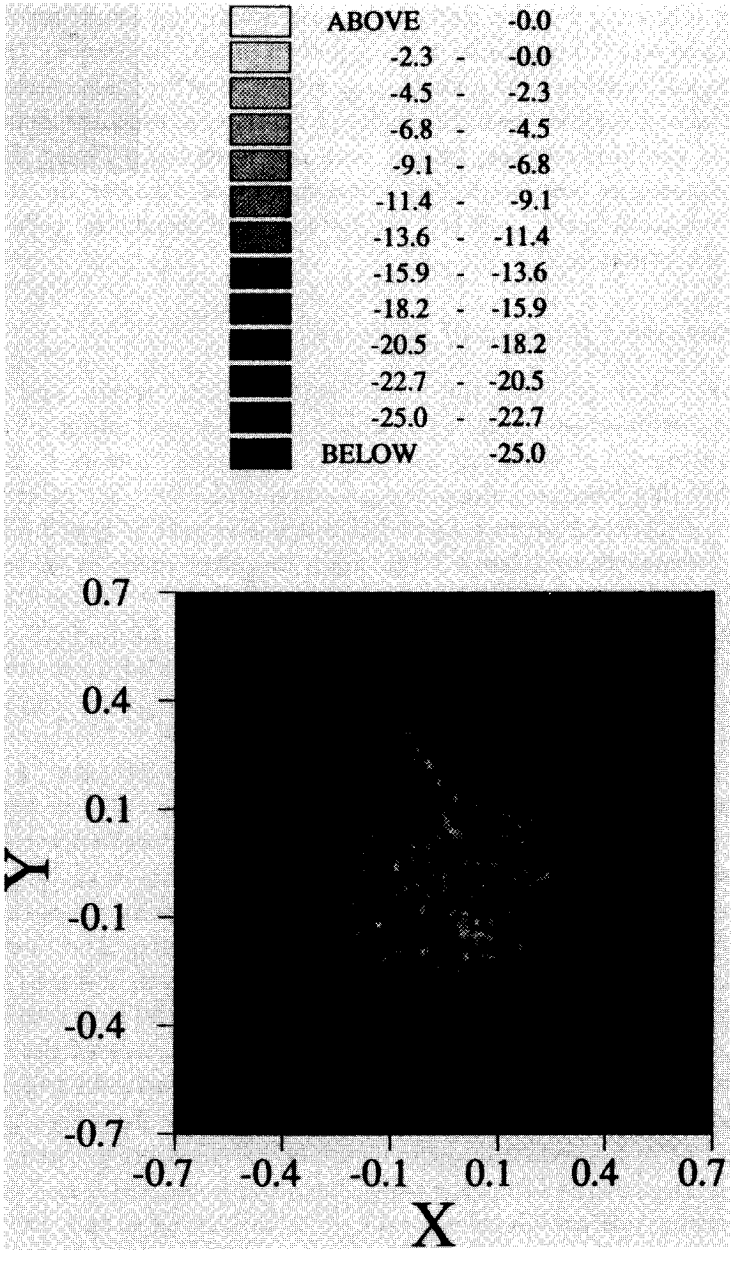

Figure 3.6.15 Shaded Contour map of Cross polarized scattered field reflectivity for the faceted surface (polarization reference for the transmitter and receiver antennas are defined by an ellipticity of $-20°$ and tilt angle of $95°$).

The following section describes some scattering experiments employing bistatic orientations and object rotation to recover the two dimensional location of the scattering reflectivity function. These targets include a faceted two dimensional surface, a machine generated Kirchhoff random surface, and a man-made surface. These surfaces were measured at various bistatic and monostatic angles for HH and VV polarization states and the projected two dimensional reflectivity images are presented.

d. Polarimetric Imaging of Surfaces

This section presents the measurements from bistatic and monostatic transmitter/receiver configurations for several different target configurations. The data are all fully polarimetric, however, in some cases only like polarized data are presented. The first set of measurements presented are from a facet-like surface shown in Fig. 3.6.9. The surface is constructed from 1200, 5cm diameter metallic disks. The scattering cells are randomly oriented in azimuth angle (uniform, 0–360°), elevation angle (uniform, 0–75°) and height (uniform, 0–15cm). The target diameter is 1.22 meters. Bistatic scattering measurements were acquired with the transmitter/receiver orientation shown in Fig. 3.6.10. The measurements were made in the 8-12GHz frequency range. The four linear phase coherent scattering elements ([s]) were recovered for a target azimuthal rotation of 0–90° in .75° increments. The recovered Fourier space data were then used to create the coherent polarization scattering cross sections shown in Figs. 3.6.11 to 3.6.13.

Because of the bistatic angle used, the data show an approximately equal response in both like and cross polarized return. The like polarized return has areas where the return is either much lower or higher than the cross polarized response. The cross polarized measurements seem to be more uniformly distributed over the surface of the target, with smaller scattering centers than in the like polarized image.

Since these returns are fully polarimetric, the data was used to synthesize the polarization response at other transmit/receiver polarization states. In the following cases, both the transmitter and receiver polarization state are identical and defined according to the convention described in section 3.3. Figs. 3.6.14 to 3.6.16 (Blanchard, *et al.*, 1988) are cross polarized images with varying ellipticity and polarization tilt. Ellipticity varies from $-10°$ to $-35°$ and orientation angle from 45° to 95°. The cross polarized response does show some tendency to shift

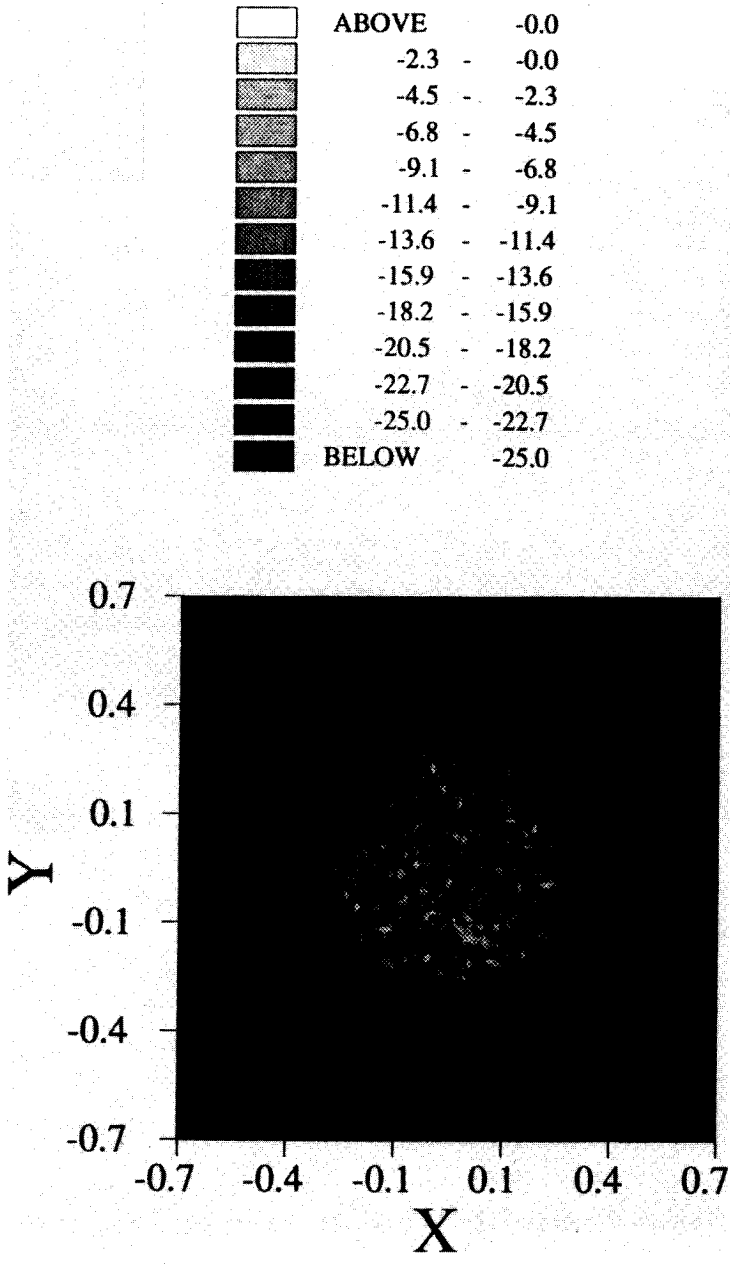

Figure 3.6.16 Shaded Contour map of Cross polarized scattered field reflectivity for the faceted surface (polarization reference for the transmitter and receiver antennas are defined by an ellipticity of $-35°$ and tilt angle of 45°).

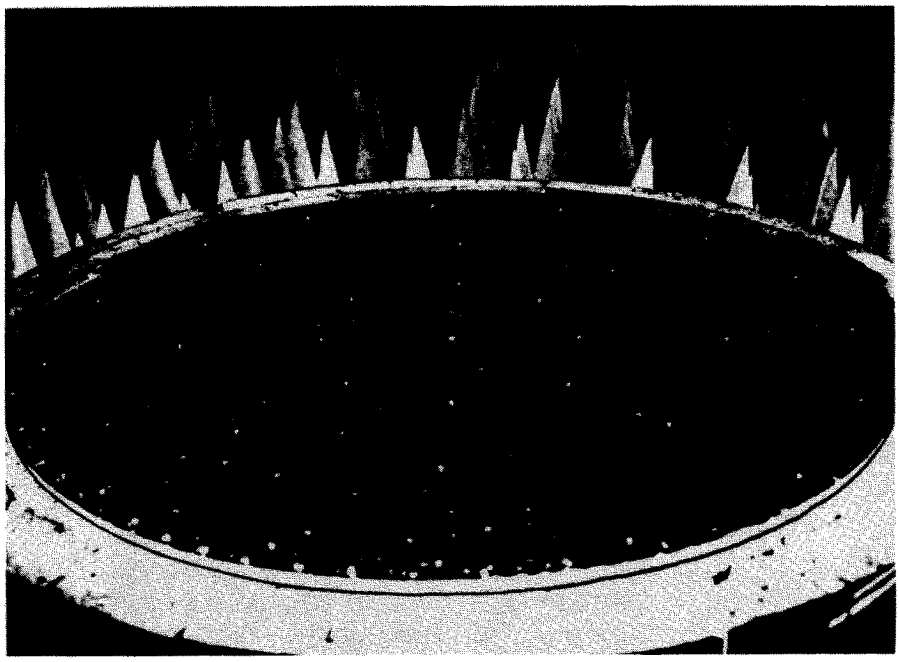

Figure 3.6.17 Photograph of the Small Perturbation surface.

the location where the centers of high cross polarized scattering occur.

The faceted surface represented a quasi-real surface, from the view point that the target parameters were easily and accurately described. A more continuous surface can represent the quality of the surface structure that is characteristic of a natural environment. The surface shown in Fig. 3.6.17 was constructed from a 1.22 meter diameter aluminum sheet. The surface roughness structure was created by striking the surface in a random fashion with ball peen hammers of three different sizes (head diameter of 2.5, 1.7, and 1.0 cm). The nature of the surface is one with small or moderate roughness at the frequencies of measurement (8-12 GHz).

The fully polarized measurements are shown in Figs. 3.6.18 to 3.6.21. The measurements configuration is identical to that used in

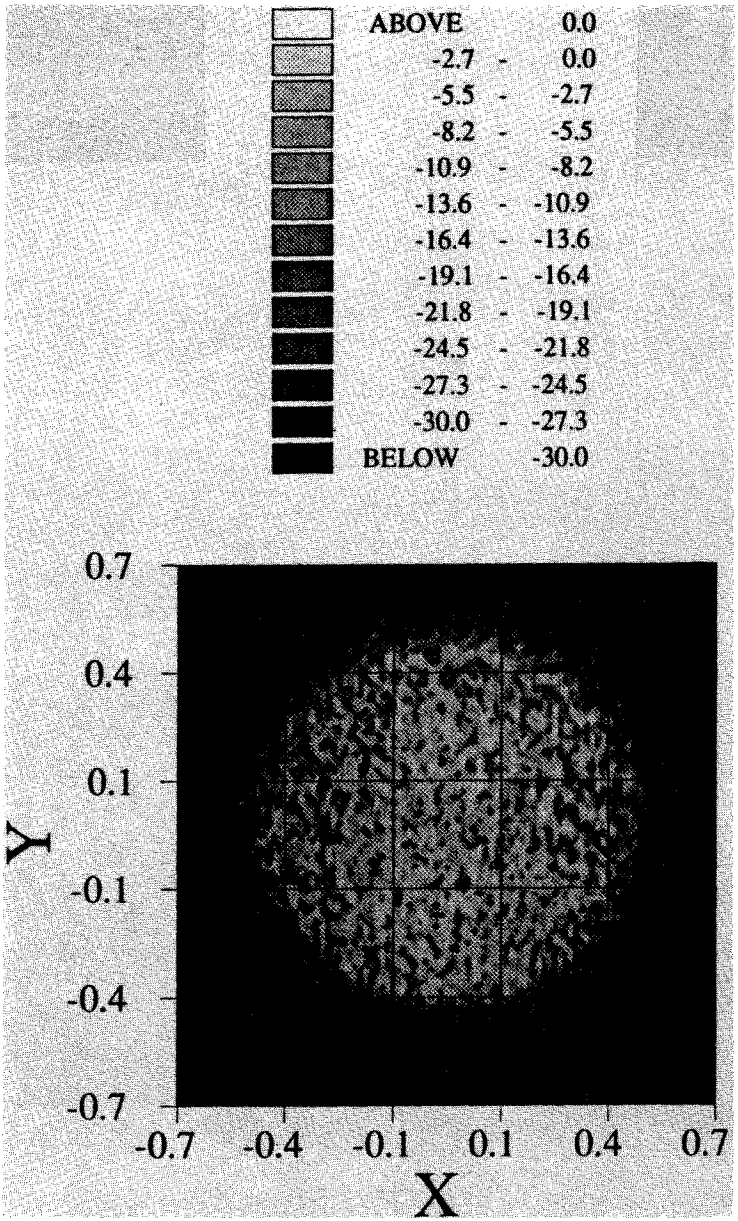

Figure 3.6.18 Shaded Contour map of VV polarized scattered field reflectivity for the Small Perturbation surface.

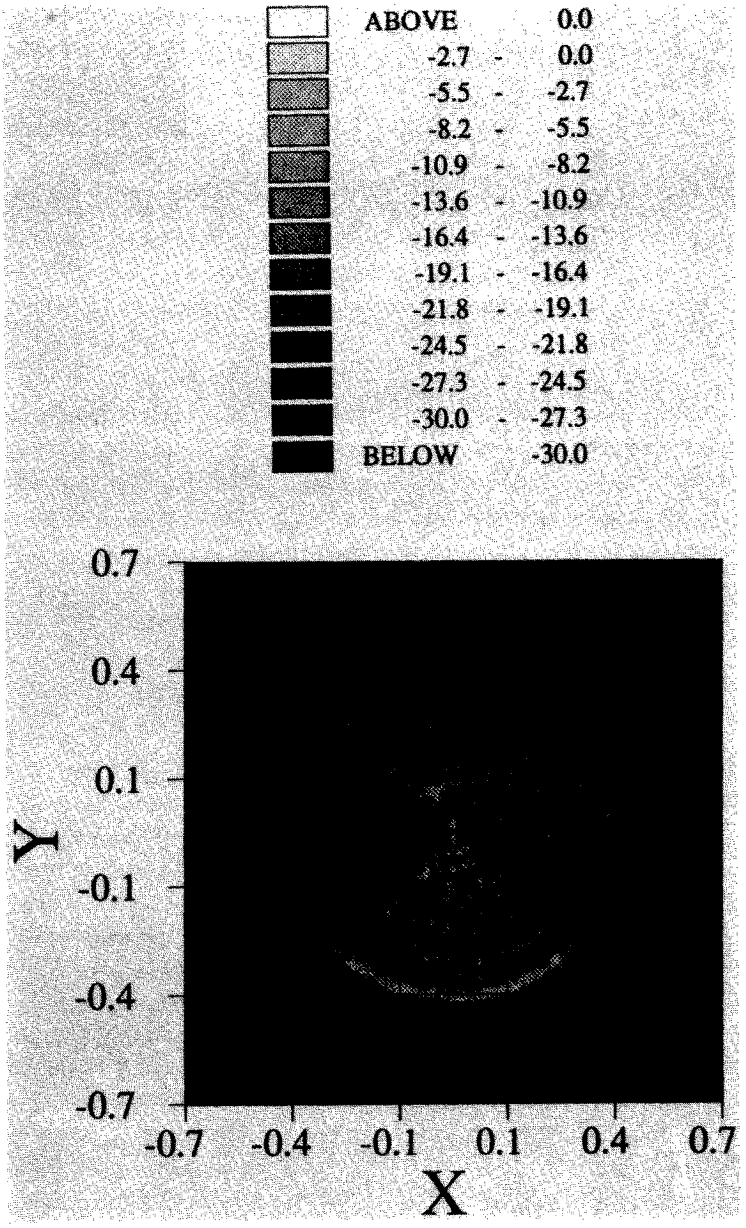

Figure 3.6.19 Shaded Contour map of HH polarized scattered field reflectivity for the Small Perturbation surface.

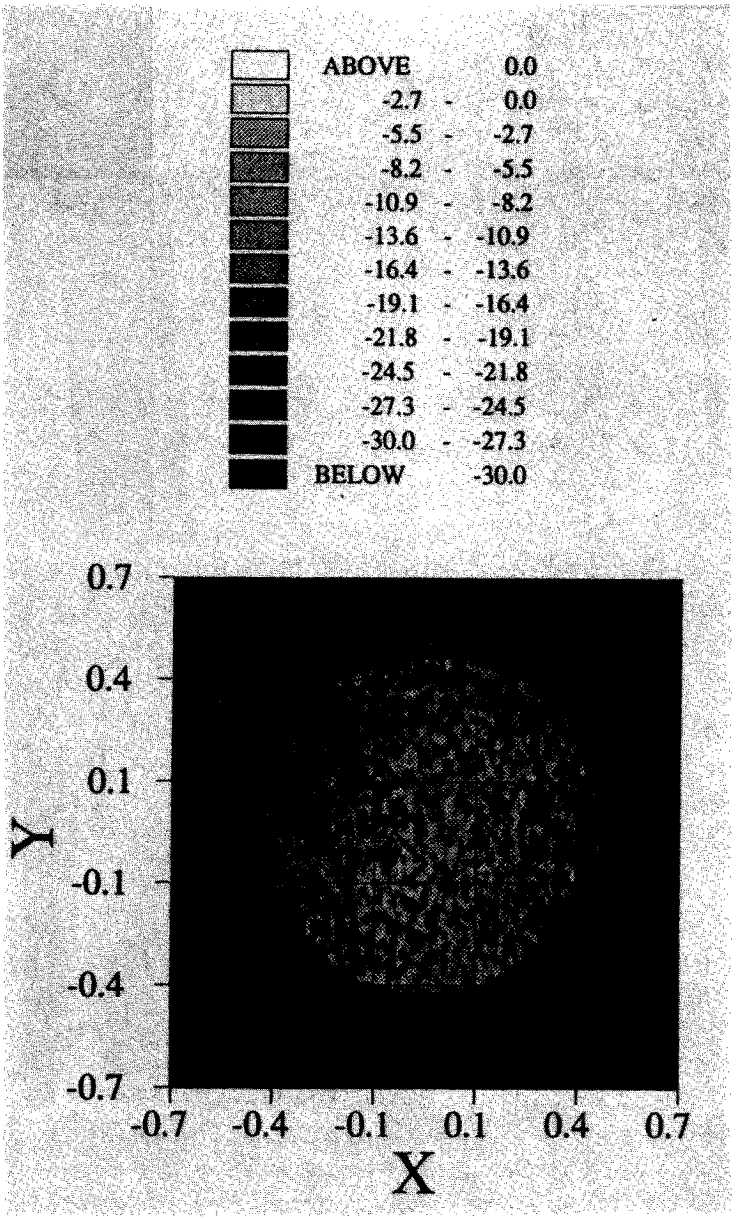

Figure 3.6.20 Shaded Contour map of HV polarized scattered field reflectivity for the Small Perturbation surface.

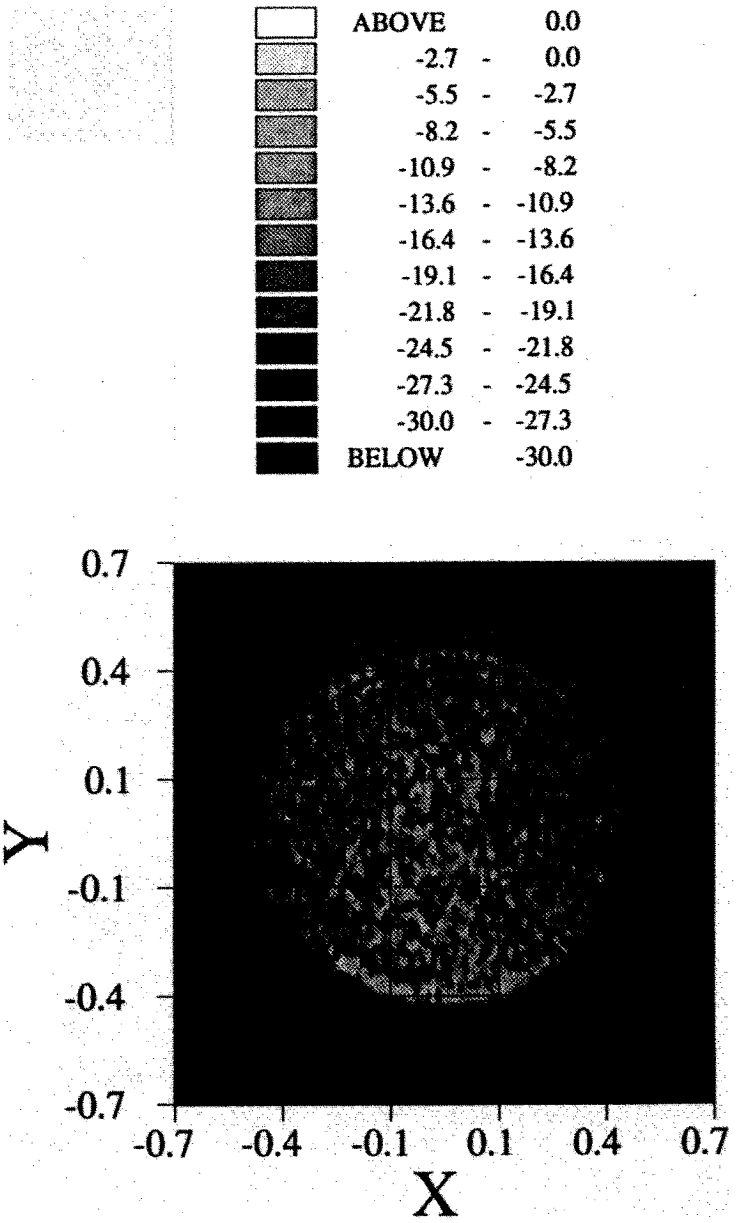

Figure 3.6.21 Shaded Contour map of VH polarized scattered field reflectivity for the Small Perturbation surface.

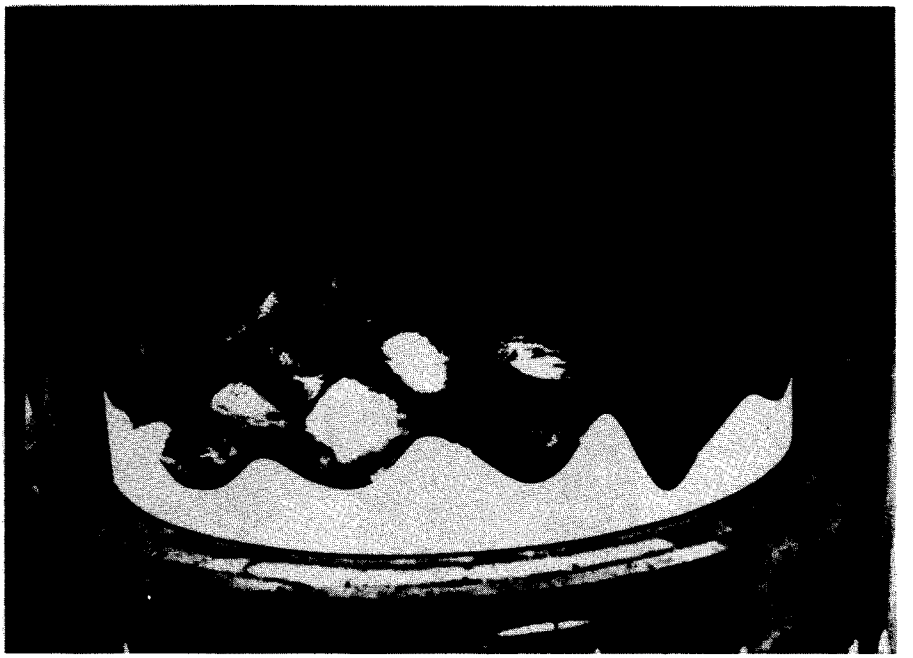

Figure 3.6.22 Photograph of the Machine generated Kirchhoff Surface.

the previously described measurement sequence. It is interesting to note that there are significant differences between the like polarized images. Although there are only slight differences in magnitude, the scattering phenomena driving the recovered images are different. For example, the HH image has a significant diffraction edge current when the transceiver looks at the edge of the finite sized target, whereas the VV image does not. Evidence of that diffraction component also appears in the VH cross polarized image, although not in the HV cross polarized return. The images also show a much finer scattering structure than the image from the previously described target (faceted target had much larger surface structure). The scattering magnitudes are larger in the cross polarized return than in the like polarized return, attributed to the bistatic transceiver configuration.

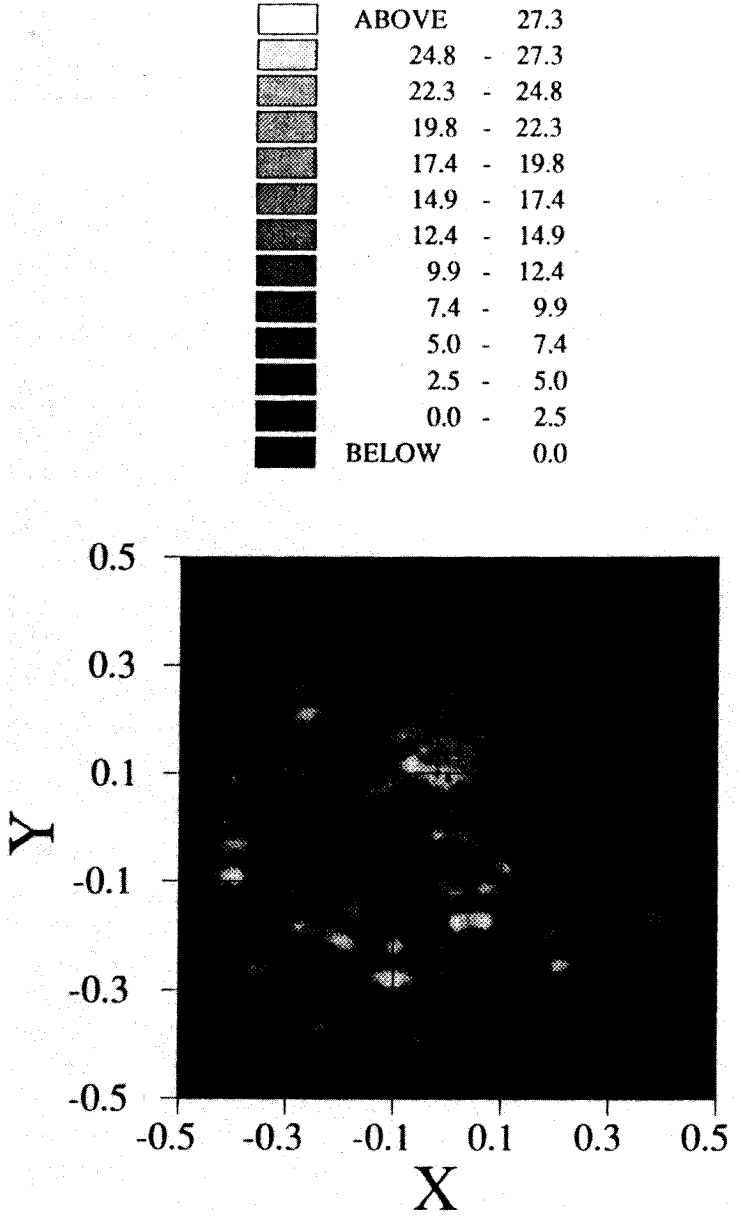

Figure 3.6.23 Shaded Contour map of VV polarized scattered field reflectivity for the Kirchhoff surface (Monostatic $\theta = 45°$).

The final surface to be discussed is a machine generated Kirchhoff surface. This surface was prepared using the technique developed by Rochier, Blanchard and Chen (1989). The surface parameters were well defined before the target was constructed (Standard deviation of surface heights 3.0 cm, and correlation length 6.8cm). The surface was measured in a monostatic configuration at $\theta = 45°$. The azimuth scan incorporated 90° of rotation. Fig. 3.6.22 presents a photograph of the Kirchhoff surface that was measured. The measured data for VV polarization is shown in Fig. 3.6.23. Because this is basically a geometric optics surface the scattering takes place from specular points that happen to face the surface at the time of the measurement. The locations of only a very few strong scattering centers appear in the image. The nature of the location and statistical distribution is also strikingly different than the images of the other targets.

Acknowledgement

This study is supported in part by the National Aeronautics and Space Administration under grant NAG 5-486.

References

[1] Bahar, E., "Scattering by anisotropic models of composit rough surface–full wave solution," *IEEE Trans. Antennas Propagat.*, **AP–33**, 106–112, 1985.

[2] Barrick, D. E., "Rough surface scattering based on the specular point theory," *IEEE Trans. Antennas Propagat.*, **AP–16**, 449–454, 1968.

[3] Bass, F. G., and I. M. Fuks, *Wave Scattering from Statistically Rough Surfaces*, New York, 1979.

[4] Blanchard, A. J., and C. E. Nance, "High Resolution Imaging Measurements of Computer Generated Surfaces", *Proceedings of Progress In Electromagnetics Research Symposium*, Boston, 1989.

[5] Blanchard, A. J., A. K. Fung, R. Schindel, and Z. Ni, "Target Detection Studies Using a Polarimetric ISAR," Invited Paper *Polari-*

metric Technology Workshop, Redstone Arsenal, Alabama, 1988.

[6] Blanchard, A. J., and M. Dolaty, "Bistatic Frequency Diverse Imaging of Complex Scattering Targets," *Proceedings of IGARSS '88 Symposium*, Edinburgh, Scotland, 1988.

[7] Beckmann, P., and A. Spizzichino, *The Scattering of Electromagnetic Waves from Rough Surfaces*, New York, 1963.

[8] Brown, G. S., "Backscattering from a Gaussian distributed perfectly conducting rough surface," *IEEE Trans. Antennas Propagat.*, **AP-26**, 472–482, 1978.

[9] Brown, G. R., "Simplification in the stochastic Fourier transform approach to random surface scattering," *IEEE Trans. Antennas Propagat.*, **AP-33**, 1985.

[10] Chen, M. F., and A. K. Fung, "A numerical study of the regions of validity of the Kirchhoff and small perturbation rough surface scattering models," *Radio Science*, **23**, 163–170, 1988.

[11] Davenport, W. B., and W. L. Root, *Random Signals and Noise*, Chapter 8, McGraw-Hill, New York, 1958.

[12] DeSanto, J. A., "Scattering from a random rough surface diagram method for elastic media," *J. Math. Phys.*, **15**, no. 3, 283–288, 1974.

[13] Devaney, M., "A filtered back propagation algorithm for diffraction tomography," *IEEE Trans. on Biomed. Engineering*, **BME-30**, No. 7, 1983.

[14] Dolaty, M., "Inverse Synthetic Aperture Imaging Techniques", *Master's Thesis*, University of Texas at Arlington, P.O. Box 19016, Arlington, TX, 1989.

[15] Farhat, N. H., C. L. Werner, T. H. Chu, "Prospects for three dimensional projective and tomography imaging networks", *Radio Science*, **9**, 1347–1355, 1984.

[16] Fuks, I. M., "Theory of Radiowave scattering at a rough sea surface," *Soviet Radiophysics*, **9**, 513–519, 1966.

[17] Fung, A. K., "Theory of cross-polarized power returned from a random surface," *Appl. Sci. Res.*, **18**, 50–60, 1967a.

[18] Fung, A. K., "Character of wave depolarization by a perfectly conducting rough surface and its application to earth and moon

experiments," *Plant. Space Sci.*, **15**, 1337–1347, 1967b.

[19] Fung, A. K., "Mechanism of polarized and depolarized scattering from rough dielectric surface," *J. Franklin Institute*, **285**, 125–133, 1968.

[20] Fung, A. K., and M. F. Chen, "Numerical simulation of scattering from simple and composite random surfaces," *J. of Optical Society of America*, **2**, 2274–2284, 1985.

[21] Fung, A. K., and G. W. Pan, "The integral equation method for rough surface scattering", *Proceeding of Multiple Scattering from Random Media and Randomly Rough Surfaces*, Pennsylvania State University, 1985.

[22] Fung, A. K., and H. L. Chan, "On backscattering from two-scale rough surface," *AGARD Conference Proc.: Propagation Limitation in Remote Sensing*, **GP-90**, 1–13, 1971.

[23] Fung, A.K., and G. W. Pan, "A scattering model for perfectly conducting random surfaces; part 1. Model development" *International J. of Remote Sensing*, **8**, 11, 1579–1593, 1987.

[24] Garcia, N., V. Celli, and M. Nieto-Vesperinas, "Exact multiple scattering of waves from random rough surfaces," *Optics Communications*, **30**, 279–281, 1979.

[25] Gray, E. P., R. W. Hart, and R. A. Farrall, "An application of a variational principle for scattering by random rough surfaces," *Radio Sci.*, **13**, 333–343, 1978.

[26] Hagfors, T., "Relationship of geometric optics and autocorrelation approaches to the analysis of lunar and planetary radar," *J. Geophys. Res.*, **71**, 379–383, 1966.

[27] Kodis, R. O., "A note on the theory of scattering from an irregular surface," *IEEE Trans. Antennas Propagat.*, **AP-14**, 1, 77–82, 1966.

[28] Kovalev, A. A. and S. I. Pozknyak, "Electromagnetic wave scattering from a statistically rough surface with finite conductivity," *Radiotekhnika*, **16**, 31–36, 1961.

[29] Langenberg, K. J., G. Bollig, M. Fischer, and D. Bruk, "Transient Methods in Electromagnetic Imaging", *Inverse Methods in Electromagnetic Imaging*, NATO ASI Series, Series C: Mathematical

and Physical Sciences, Vol. 143-Part I, D. Reidel Publishing Co., 87–110, 1983.

[30] Leader, J. C., "Incoherent backscatter from rough surfaces; the two-scale model re-examined," *Radio Science*, **13**, 441–457, 1978.

[31] Pan, G. W., and A. K. Fung, "A scattering model for perfectly conducting random surfaces: part 2. Range of validity" *International J. of Remote Sensing*, **8**, 11, 1595–1605, 1987.

[32] Poggio, A. J., and E. K. Miller, "Integral equation solution of three-dimensional scattering problms", Chapter 4 of *Computer Techniques for Electromagnetics*, Pergamon, New York, 1973.

[33] Press, W. H., B. P. Flannery, S. A. Teukolsky, and W. H. Vetterling, *Numerical Recipes The Art of Scientic Computing*, Chapter 7, Cambridge University Press, 1987.

[34] Rice, S. O., "Reflection of electromagnetic waves from slightly rough surfaces," *Comm. Pure Appl. Math.*, **4**, 213, 361–378, 1951.

[35] Rochier, J. D., A. J. Blanchard, and M. F. Chen, "The generation of surface targets with specified surface statistics," Accepted for publication on the *Int. J. of Remote Sensing*, 1989.

[36] Sancer, M. I., "Shadow-corrected electromagnetic scattering from a randomly rough surface," *IEEE Trans. Antennas Propagat.*, **AP-17**, 5, 577–589, 1969.

[37] Semyonov, G., "Approximate computation of scattering of electromagnetic waves by rough surface contours," *Radio Eng. an Elect. Phys.*, **11**, 1179–1187, 1966.

[38] Thorsos, E. I., "The validity of the Kirchhoff approximation for rough surface scattering using a Gaussian roughness spectrum," *J. of Acoustic Society of America*, **83**, 1, 78–92, 1988a.

[39] Thorsos, E. I., "An examination of the full wave method for rough surface scattering", presented at the National Radio Science Meeting, University of Colorado, Boulder, Colorado, Janurary 1988b.

[40] Ulaby, F. T., R. K. Moore, and A. K. Fung, *Microwave Remote Sensing: Active and Passive*, **2**, Chapter 12, Artech House, 1982.

[41] Valenzuela, G. R., "Depolarization of EM waves by slightly rough surfaces," *IEEE Trans. Antenna Propagat.*, **AP-15**, 4, 552–557, 1967.

[42] Valenzuela, G. R., "Scattering of electromagnetic waves from a tilted slightly rough surface", *Radio Science*, **3**, 1057–1066, 1968.

[43] Wright, J. W., "A new model for sea clutter", *IEEE Trans. Antennas Propagat.*, **AP-16**, 2, 217–223, 1968.

[44] Winebrenner, D. P., and A. Ishimaru, "Application ot the phase perturbation technique to randomly rough surfaces", *J. Opt. Soc. Am.*, **2**, 12, 2285–2294, 1985.

[45] Wu, S. T., and A. K. Fung, "A noncoherent model for microwave emission and backscattering from the sea surface," *J. Geophys. Res.*, **77**, 30, 5917–5929, 1972.

[46] Wu, S. C., M. F. Chen, and A. K. Fung, "Non-Gaussian surface generation," *IEEE Trans. on Geos. and Remote Sensing*, **26**, 6, 885–888, 1988a.

[47] Wu, S. C., M. F. Chen, and A. K. Fung, "Scattering from non-Gaussian randomly rough surfaces-cylindrical case" *IEEE Trans. on Geos. and Remote Sensing*, **26**, 7, 790–798, 1988b.